

3D Crystal Structures and Solid-State Properties of  
Polyhedral  $\pi$ -Conjugated Organic Radicals

(立体  $\pi$  共役有機ラジカルの三次元結晶構造と固体物性)

ASATO MIZUNO

水野 麻人

Department of Chemistry, Graduate School of Science

Nagoya University

2018

## Table of Contents

<b>Acknowledgements.....</b>	<b>5</b>
------------------------------	----------

<b>Nomenclature.....</b>	<b>7</b>
--------------------------	----------

### Chapter 1

<b>General Introduction .....</b>	<b>10</b>
-----------------------------------	-----------

1.1 Molecular Conductors and Magnets.....	10
---	----

1.2 Crystal Engineering in Molecular Conductors and Magnets.....	13
--	----

1.3 $K_4$ Crystal: Isotropic 3D Structures .....	19
--	----

1.4 Geometrical Spin Frustration and Quantum Spin Liquid States .....	24
---	----

1.5 Polyhedral $\pi$ Acceptors of Naphthalene-Diimide-Based Rigid Cyclophanes .....	27
---	----

1.6 Motivation and Scope of This Thesis .....	33
---	----

### Chapter 2

#### Preparation, Electronic and Magnetic Properties of Radical Anion

<b>Salts of (-)-NDI-<math>\Delta</math>: Construction of Molecular 3D <math>K_4</math> Crystals.....</b>	<b>36</b>
--	-----------

2.1 Introduction .....	36
------------------------	----

2.2 Preparation of Radical Anion Salts of (-)-NDI- $\Delta$ .....	37
---	----

2.3 X-ray Crystal Structures of Radical Anion Salts .....	39
---	----

2.4 Characterization of Rb Salt .....	45
---------------------------------------	----

2.5 Band Structure of Rb Salt.....	47
------------------------------------	----

2.6 Electronic and Magnetic Properties of Rb Salt .....	50
2.7 Conclusion .....	53
2.8 Experimental Section.....	54
2.8.1 Synthesis of (-)-NDI- $\Delta$ and Its Radical Anion Salts.....	55
2.8.2 X-ray Structural Analysis .....	57
2.8.3 Magnetic and Electronic Measurements.....	59
2.8.4 DFT and Band-Structure Calculations .....	59

## Chapter 3

### Spin-Frustrations in the Hyperkagome Lattices in the $K_4$ Crystals of

<b>(-)-NDI-<math>\Delta</math>.....</b>	<b>60</b>
3.1 Introduction .....	60
3.2 X-ray Analysis and Characterization of TBA Salt.....	61
3.2.1 X-ray Analysis of TBA Salt.....	61
3.2.2 Comparison between Rb and TBA Salts .....	63
3.2.3 Characterization of TBA Salt .....	64
3.3 Band Structure and Electronic Properties of TBA Salt .....	66
3.4 Spin Lattice of TBA Salt: $K_4$ Crystal to Hyperkagome Lattice .....	68
3.5 Magnetic Properties of TBA Salt.....	72
3.6 Thermal Properties of TBA Salt .....	77
3.7 Comparison with Organic Gapless Quantum Spin Liquids.....	81
3.8 Conclusion.....	83
3.9 Experimental Section.....	84

3.9.1 Preparation of (-)-NDI- $\Delta$ Radical Anion Salts .....	84
3.9.2 X-ray Structural Analysis .....	85
3.9.3 Magnetic and Electronic Measurements.....	86
3.9.4 Heat-Capacity Measurements.....	87
3.9.5 DFT and Band-Structure Calculations .....	87

## Chapter 4

### Preparation of 3D Chiral Crystals of Radical Anions of (-)-NDI- $\Delta$ :

#### Formation of (*M*)- and (*P*)-Helices from a Chiral Molecule ..... 88

4.1 Introduction .....	88
4.2 Preparation and X-ray Analysis of Radical Anion Salts of (-)-NDI- $\Delta$ .....	89
4.3 Characterization of Rb@18-crown-6 Salt .....	97
4.4 Magnetic, Electronic, and Thermal Properties of Rb@18-crown-6 Salt.....	100
4.5 Conclusion.....	102
4.6 Experimental Section.....	104
4.6.1 Preparation of (-)-NDI- $\Delta$ Radical Anion Salts .....	104
4.6.2 X-ray Structural Analysis .....	105
4.6.3 Magnetic, Electronic, and Heat-capacity Measurements .....	106

## **Chapter 5**

### **Supramolecular Crystal Structures of Charge-Transfer Complexes of**

<b>(-)-NDI-<math>\Delta</math>.....</b>	<b>107</b>
5.1 Introduction .....	107
5.2 Preparation and X-ray Analysis of CT Complexes of (-)-NDI- $\Delta$ .....	108
5.2.1 TTF Complexes .....	109
5.2.2 Pyrene and Perylene Complexes .....	112
5.3 Diffuse Reflectance Spectra of CT Complexes .....	116
5.4 Conclusion .....	118
5.5 Experimental Section.....	119

## **Chapter 6**

<b>Conclusions .....</b>	<b>121</b>
<b>Bibliography .....</b>	<b>124</b>
<b>List of Publications.....</b>	<b>134</b>

## Acknowledgements

This work was carried out under the supervision of Professor Kunio Awaga at the laboratory of advanced materials, Department of Chemistry, Graduate School of Science, Nagoya University. I would like to gratefully thank Professor Kunio Awaga for his valuable discussion, kind guidance, and continuous encouragement throughout this work. He also gave me a lot of opportunities of international and domestic research collaborations, and supported me to study abroad.

I would like to thank Associate Professor Michio M. Matsushita for his kind help and fruitful discussion in conductivity and transistor measurements, and theoretical calculations. I would like to thank Dr. Zhongyue Zhang for his kind support. I especially would like to thank Dr. Yoshiaki Shuku for instructing me a lot of things including experimental techniques, data analyses, preparation of beautiful figures, etc. Without his selfless help, this thesis would never completed. I also would like to thank Dr. Seiya Yokokura and Dr. Keitaro Eguchi for their fruitful comments and discussion. I also like to thank Ms. Amy Qu and Mr. Joseph Hardie for their kind advices on my thesis. I am grateful to Dr. Matvey Gruzdev for his kind instruction of useful synthetic techniques.

I am extremely grateful to Associate Professor Masahisa Tsuchiizu (Nara Women's University) for his band calculation, kind suggestion and fruitful discussion on my entire research. I am extremely grateful to Professor Nobuo Wada for his magnetic and heat-capacity measurements using a dilution refrigerator, and kind and fruitful discussion. I grateful to Mr. Yuki Hara for his kind support during the measurements. I would like to thank all the members in Wada Group for giving a warm welcome to me. I would like to thank Dr. Yasuhiro Shimizu for his solid-state NMR measurements and

fruitful discussion. I would like to thank Associate Professor Hirofumi Yoshikawa Hirofumi (currently at Kwansai Gakuin University) for instructing me SEM-EDX measurements. I would like to thank Mr. Kinichi Oyama for his help in a lot of analyses including elemental analysis, mass spectroscopy, and ICP and NMR measurements. I would like to thank Professor Vincent Robert (Université de Strasbourg), Professor Francesc Illas (Universitat de Barcelona), and Dr. Daniel Reta Mañeru (Universitat de Barcelona) for their theoretical calculation. I would like to thank Dr. Rie Suizu (Chiba University) for her help in the X-ray analysis. I am grateful to Professor Jeremy Rawson, Dr. Muhammad Usman Anwar, and Dr. Yassine Beldjoudi (University of Windsor) for their kind support and instruction of various techniques for synthesis of thiazyl radicals during my stay in Windsor. I am also grateful to Professor Neil Robertson, and Dr. Helen Benjamin for their kind discussion and instruction during my stay in the University of Edinburgh. I also grateful to Dr. Stephene Moggach and Mr. Jonathane Richardson (the University of Edinburgh) for their kind support on high-pressure X-ray analysis.

I would like to thank all the members in Awaga group for their kind supports and discussion. I would especially thank to Ms. Sayuri Handa, Ms. Motoko Tsuchibe, and Ms. Hideko Watanabe, the secretaries in Awaga group for supporting my research lives.

I would like to thank Integrative Graduate Education and Research Program in Green Natural Scientists (IGER) for the financial support. This work was also supported by a Grant-in-Aid for the Japan Society for the Promotion of Science (JSPS) for the research fellowship for young scientists.

Finally, I sincerely thank to my parents for their continuous supports and understanding.

Asato Mizuno

## Nomenclature

ATR	Attenuated total reflection
BBDTA	Benzo[1,2-d:4,5-d']bis[1,3,2]dithiazole
BCS	Bardeen Cooper Schrieffer
BEDT-TTF (ET)	Bis(ethylenedithio)tetrathiafulvalene
Bu	Butyl
Cat-EDT-TTF	Catechol-fused ethylenedithiotetrathiafulvalene
COF	Covalent organic framework
15-crown-5	1,4,7,10,13-pentaoxacyclopentadecane
18-crown-6	1,4,7,10,13,16-hexaoxacyclooctadecane
2,2,2-cryptand	4,7,13,16,21,24-hexaoxa-1,10-diazabicyclo[8.8.8]hexacosane
CT	Charge-transfer
CV	Cyclic voltammetry
DBE	1,2-dibromoethane
DCE	1,2-dichloroethane
DDDT	5,6-dihydro-1,4-dithiin-2,3-dithiolate
DFT	Density functional theory
Diglyme	1-methoxy-2-(2-methoxyethoxy)ethane
DIPSe	Diiodo(pyrazino)tetraselenafulvalene
DMF	<i>N,N</i> -dimethylformamide
DMIT	1,3-dithio-2-thione-4,5-dithiolate
DNA	Deoxyribonucleic acid
DOS	Density of states
EC	Ethylene carbonate (1,3-dioxolan-2-one)
EDX	Energy dispersive X-ray spectrometry
EDT-TTF	Ethylenedithiotetrathiafulvalene
ESR	Electron spin resonance
Et	Ethyl
EPR	Electron paramagnetic resonance
FAB	Fast atom bombardment
Fc	Ferrocene
FET	Field effect transistor
FT	Fourier transform

HOMO	Highest occupied molecular orbital
ICP	Inductively coupled plasma
IR	Infrared
LUMO	Lowest occupied molecular orbital
NDA	1,4,5,8-naphthalenetetracarboxylic dianhydride
NDI	Naphthalene diimide
NIR	Near-infrared
NMP	<i>N</i> -methyl-2-pyrrolidone
NMR	Nuclear magnetic resonance
<i>p</i> -NPNN	2-(4-nitrophenyl)-4,4,5,5-tetramethylimidazoline-3-oxide-1-oxyl
Me	Methyl
MOF	Metal organic framework
MPMS	Magnetic property measurement system
MS	Mass spectrometry
OES	Optical emission spectroscopy
PC	Propylene carbonate (4-methyl-1,3-dioxolan-2-one)
PDI	Perylene diimide
Ph	Phenyl
PPMS	Physical property measurement system
Pr	Propyl
Py	Pyridinium
PMA (PyDI)	Pyromellitic diimide
PXRD	Powder X-ray diffraction
RVB	Resonating valence bond
SCE	Saturated calomel electrode
SEM	Scanning electron microscope
SOMO	Singly occupied molecular orbital
STM	Scanning tunneling microscope
SQUID	Superconducting quantum interference device
$\mu$ SR	Muon spin rotation
TBA	Tetrabutylammonium
TCNQ	7,7,8,8-tetracyanoquinodimethane
TDAE	Tetrakis(dimethylamino)ethylene
TMDT	Trimethylenetetraathiafulvalenedithiolate
TMTSF	Tetramethyltetraselenafulvalence
TOA	Tetraoctylammonium

TTF	Tetrathiafulvalene
UHV	Ultra high vacuum
UV	Ultraviolet
VIS	Visible

# Chapter 1 General Introduction

## 1.1 Molecular Conductors and Magnets

The first major event in the history of molecular conductors was the (photo)conductivity measurements of phthalocyanines and polycyclic aromatic hydrocarbons.<sup>1-4</sup> The first molecular semiconductors, which exhibited a high conductivity of  $1-10^{-3}$  S cm<sup>-1</sup>, were the perylene-bromine complexes discovered by Akamatsu, Inokuchi, and Matsunaga in 1954.<sup>5</sup> This discovery showed the good potential of organic conductors and demonstrated for the first time that carrier doping is useful to enhance conductivity. In the case of the study by Akamatsu and colleagues, carrier doping was achieved by means of a charge-transfer interaction. Charge-transfer complexes, which are prepared by mixing electron donors and electron acceptors, show various oxidized (reduced) states depending on their combinations.

In 1972, Epstein et al. discovered the first organic metal, NMP-TCNQ, which exhibited a metallic conductivity down to 200 K.<sup>6</sup> In 1973, a more promising complex, TTF-TCNQ, was reported,<sup>7,8</sup> which showed a high conductivity of 1837 S cm<sup>-1</sup> at room temperature.<sup>7</sup> TTF-TCNQ retained a metallic conductivity down to 60 K and underwent a metal-insulator transition at 53 K due to the Peierls instability, which is typical for 1D conductors. In order to suppress this instability, the dimensionality of the organic conductors was increased by introducing sulfur, selenium, and tellurium into the molecular skeletons. Various organic superconductors have been explored along this molecular design.<sup>9-11</sup>

In 1980, Jérôme et al. discovered the first organic superconductor, a quasi-one-dimensional conductor  $(\text{TMTSF})_2\text{PF}_6$ , which exhibited a superconducting phase transition at 0.9 K under 12 kbar.<sup>12</sup> A superconducting transition temperature exceeding 10 K was observed for a two-dimensional BEDT-TTF salt in 1988.<sup>13</sup> A decade later, Tanaka et al. reported the first single component conductor,  $\text{Ni}(\text{tmdt})_2$ , which retained a metallic conductivity down to 0.6 K,<sup>14</sup> and the three-dimensional Fermi surface of this material was experimentally demonstrated.<sup>15</sup> Recent research into molecular conductors has expanded to include studies on massless Dirac fermions, which are well-known in graphene physics.<sup>16</sup> Dirac cones have been investigated in the bulk crystals of  $\alpha$ -(BEDT-TTF) $_2\text{I}_3$ <sup>17</sup> and  $\text{Pd}(\text{dddt})_2$ <sup>18</sup> under high pressure.

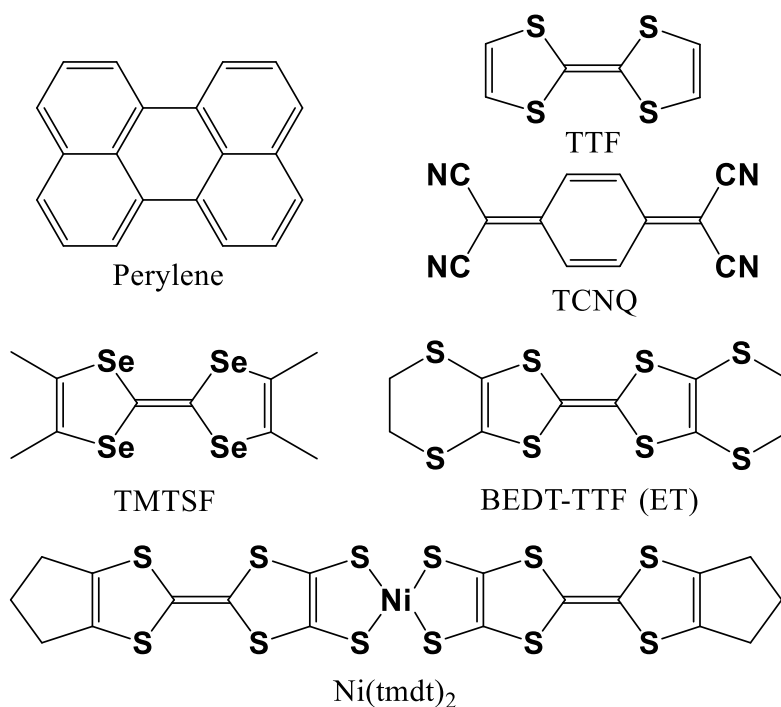


**Figure 1.1.** Molecular structures of the representative molecular conductors and magnets.

Ferromagnetic interactions in organic radicals were not observed until the 1960s due to the strong tendency of organic radicals to dimerize in the solid state. The first theoretical principles in the effort to realize molecular ferromagnets were proposed by McConnell in 1963.<sup>19</sup> Several years later, a high-spin molecule, *m*-phenylenebis(phenylmethylene), was reported.<sup>20,21</sup> This and other high-spin polycarbenes<sup>22,23</sup> have been developed as model compounds to investigate the intramolecular ferromagnetic interactions. A neutral radical, galvinoxyl, is one of the well-known organic magnets exhibiting intermolecular ferromagnetic interactions (Figure 1.2).<sup>24,25</sup> It was first reported by Mukai in 1969<sup>24</sup> and its ferromagnetic interactions were rationalized by McConnell's principles. In 1989, Awaga and Maruyama reported a ferromagnetic intermolecular interaction of 0.9 K in an organic nitroxide radical, *p*-NPNN( $\beta$  phase),<sup>26</sup> and in 1991 Tamura et al. discovered the first example of organic ferromagnets with a transition temperature of 0.6 K.<sup>27</sup> Today, the transition temperatures for a molecular magnet without C<sub>60</sub> and transition metals as spin centers reach 17 K for a ferromagnet based on selenazyl radicals developed by Robertson et al.,<sup>28</sup> and 36 K for a weak ferromagnet,  $\beta$ -[*p*-NCC<sub>6</sub>F<sub>4</sub>CN<sub>2</sub>SSN] (a thiazyl radical), reported by Banister et al.<sup>29</sup> Experimental work on molecular magnets has also focused on low-dimensional magnetism,<sup>30,31</sup> spin frustration,<sup>32</sup> spintronics,<sup>33,34</sup> etc.

Among the molecules used in molecular conductors and magnets, C<sub>60</sub><sup>35,36</sup> is one of the most promising candidates. Numerous 3D isotropic structures have been constructed based on the ideal spherical shape of C<sub>60</sub>, and high-*T<sub>c</sub>*-ferromagnets<sup>37,38</sup> and superconductors<sup>39,40</sup> of the C<sub>60</sub> complexes have been reported. The highest superconducting temperature at ambient pressure is observed for an anion radical complex, RbCs<sub>2</sub>C<sub>60</sub>, which shows a superconductivity at 33 K.<sup>40</sup> The trend of

superconducting transition temperatures of fullerene complexes is rationalized by the BCS theory; the densities of states based on the highly degenerated LUMOs of  $C_{60}$  are related to the transition temperatures.<sup>41–43</sup> The charge-transfer complex of TDAE- $C_{60}$  also shows the highest ferromagnetic transition temperature of 16 K among molecular ferromagnets.<sup>37</sup> These studies on the  $C_{60}$  complexes indicate the importance of the 3D intermolecular interactions resulting from the high symmetry of the spherical molecule.

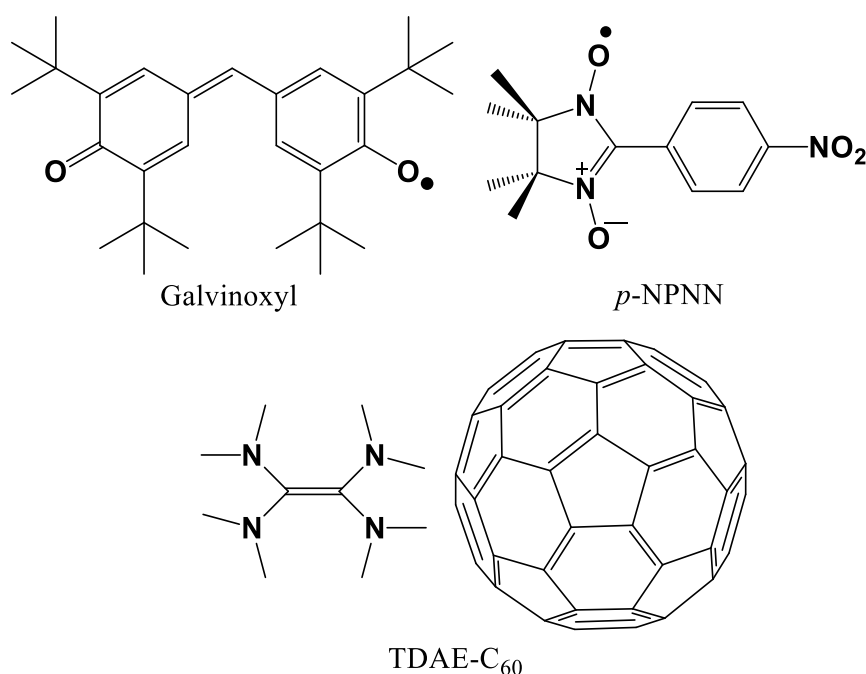


**Figure 1.2.** Molecular structures of the representative molecular magnets, galvinoxyl, *p*-NPNN, and TDAE- $C_{60}$ .

## 1.2 Crystal Engineering in Molecular Conductors and Magnets

As described in Section 1.1, the dimensionality of molecular crystals is a key factor which dominates their solid-state properties. Careful tuning of the molecular skeletons affects the packing motifs, and is crucial to obtain exotic physical properties

such as superconductivity, Dirac cones, and quantum spin liquid states. In this section, various approaches and development of the crystal engineering are described.

Crystal structures of molecular magnets and conductors are determined from various types of intermolecular interactions such as van der Waals forces, hydrogen bonds, and CT interactions. The first series of organic metals, including NMP-TCNQ<sup>6</sup> and TTF-TCNQ,<sup>7,8</sup> were prepared based on the CT interactions. Figure 1.3 shows two typical crystal packings of CT complexes. They usually form segregated stacks and alternate stacks in their solid states. For example, the crystal of TTF-TCNQ shows segregated stacks with eclipsed  $\pi$ - $\pi$  overlaps, which are accompanied by a partial charge transfer of  $0.59 e^-$  from TTF to TCNQ.<sup>44,45</sup> This type of eclipsed overlap is stabilized by the exchange interactions between the radical species, although the slipped overlaps are usually preferable due to the electron repulsive force between aromatic rings. Exchange interactions are characteristic of radical species and have played an important role in their crystal packing. Two types of exchange interactions, namely potential exchange and kinetic exchange, are depicted in Figure 1.4. The potential exchange stabilizes parallel spin alignment (or ferromagnetic interaction), and is well-known as the basis for Hund's rule in the ground states of a multi-electron atom. The other type of exchange interaction, the kinetic exchange, stabilizes antiparallel spin alignment (or antiferromagnetic interaction). The potential exchange is dominant only when the net intermolecular overlaps are almost zero, a limitation known as the Goodenough-Kanamori rule.<sup>46-48</sup> Thus, the crystals of molecular radicals often show antiferromagnetic interactions and the molecules simultaneously tend to dimerize as shown in Figure 1.4(c). Eclipsed overlaps are preferable in order to maximize the overlap between the SOMOs and the radical-radical interactions. These interactions lead to significantly shorter contact distances

(strong dimerization) and are known as “pancake bonds,”<sup>49,50</sup> which are recognized in various kinds of molecular radicals in their solid states (Figure 1.5).<sup>49</sup>

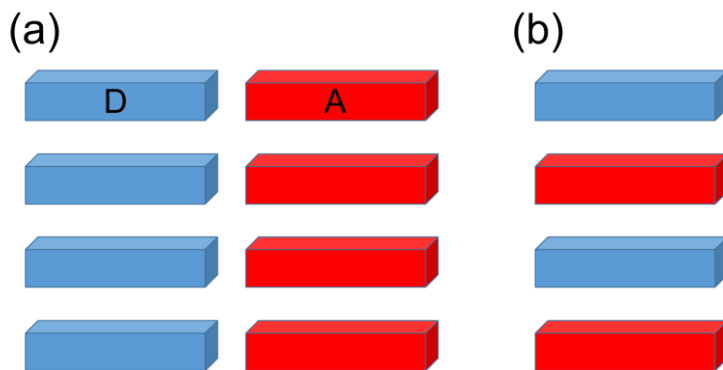


**Figure 1.3.** A segregated stack (a) and an alternate stack (b) that are typical for CT complexes. Blue and red squares indicate donor and acceptor molecules.

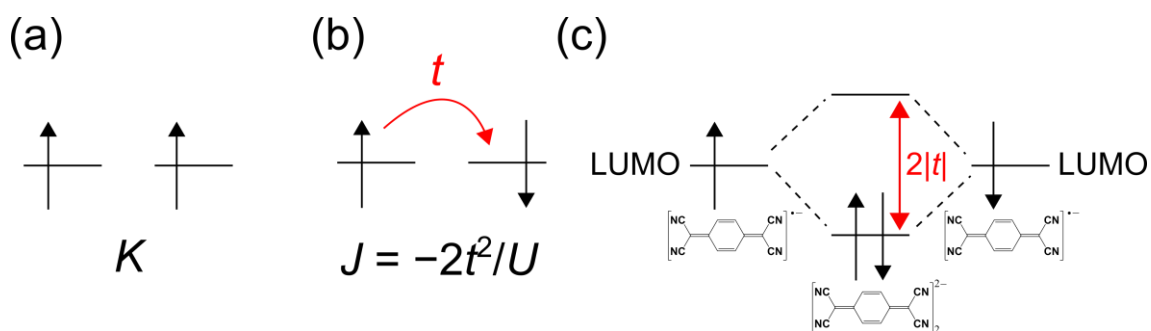


**Figure 1.4.** (a) Potential exchange  $K$ . (b) Kinetic exchange  $J$ . (c) Radical-radical interactions and the resulting dimerization in TCNQ radical anions.

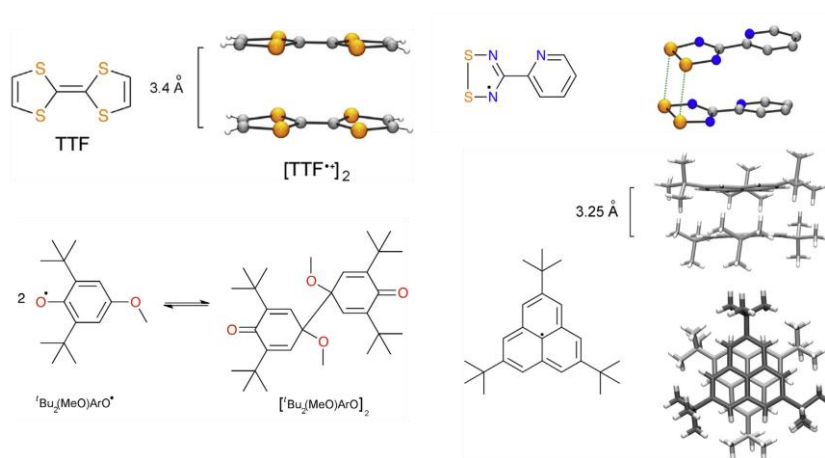


**Figure 1.5.** Strong dimerization in various organic radicals. (Adapted from Preuss.<sup>49</sup>)

One way to modulate the crystal packing from the usual 1D stacking (with dimerization) is to use steric hindrance. Inabe et al. designed axially ligated phthalocyanines<sup>51,52</sup> in which two  $\text{CN}^-$  ions are coordinated to their metals from above and below the  $\pi$ -planes. Due to the steric hindrance caused by the coordinated  $\text{CN}^-$  ions, the oxidized axially ligated phthalocyanines form 1D and 2D  $\pi$ - $\pi$  stacking networks in a manner dependent on the counter cations (Figure 1.6). In the 2D  $\pi$ - $\pi$  stacking network, the charge localization is suppressed and metallic conductivity is observed.<sup>52</sup>

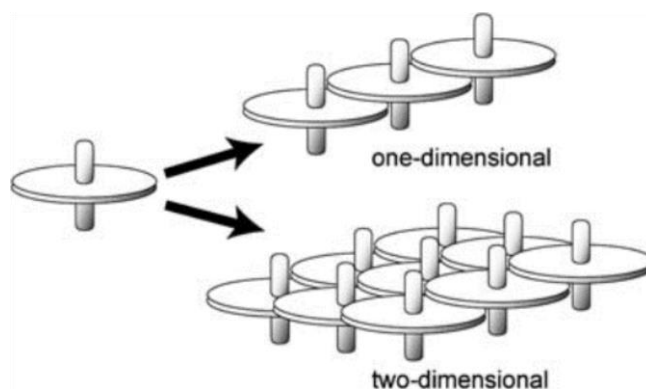


**Figure 1.6.** Schematic image of the crystal packing motifs of axially ligated phthalocyanines. They can form 1D and 2D  $\pi$ - $\pi$  stacking networks. (Reproduced from Inabe et al.<sup>51</sup>)

Halogen bonding is also useful to control the structures. This interaction is a highly directional one between halogen atoms and Lewis bases (halogen atoms, N, O, S, Se, etc.). Yamamoto et al. reported a conducting nanowire of EDT-TTF cation radicals surrounded by an insulating network consisting of supramolecular assemblies formed by halogen bonding between the halide anions and neutral solvent molecules (Figure 1.7(a)).<sup>53,54</sup> Their work indicated that the resulting network had high potential as a sheathing material. Imakubo et al. successfully induced a hexagonal supramolecular structure with a 1D channel by halogen bonding between donor molecules (Figure

1.7(b)).<sup>55–57</sup> The channel can be used as a reaction path, and the cation radicals of DIPSe are reduced by reaction with water in organic solvents in a high yield of 90%. This means that the organic conductor is recyclable. Moderately strong, highly directional halogen bonding has the potential to form these types of unique structures.

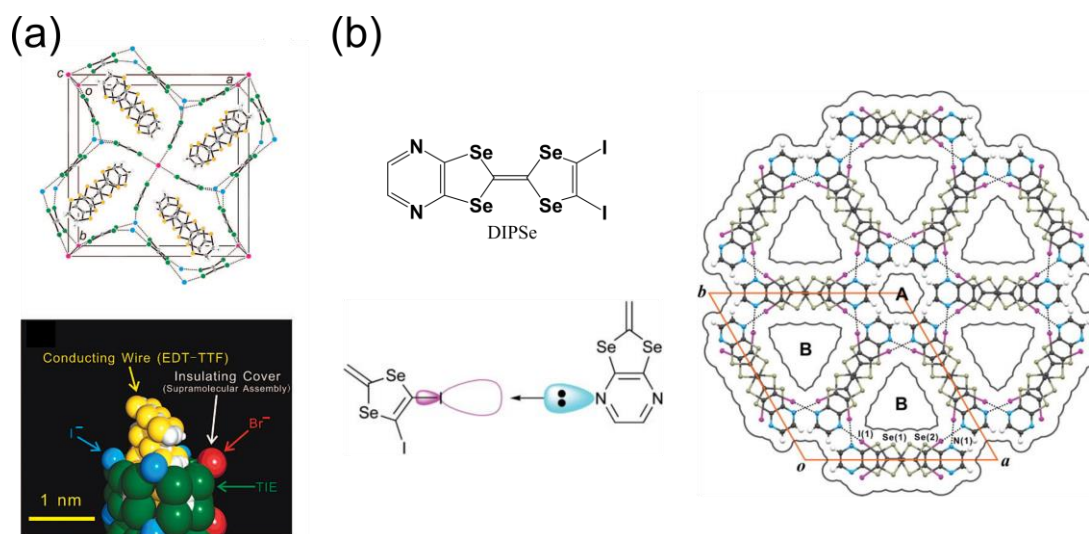


**Figure 1.7.** (a) Crystal structure and schematic image of the conducting nanowire of the radical cations of EDT-TTF surrounded by the halogen bond network. (b) Molecular structure of DIPSe, formation of the halogen bond between donor molecules, and hexagonal supramolecular structure of the radical cation salts  $(\text{DIPSe})_3(\text{PF}_6)_{1.33}(\text{CH}_2\text{Cl}_2)_{1.2}$ . ((a) Adapted from Yamamoto et al.<sup>53</sup> (b) Bottom left and right figures adapted from Imakubo et al.<sup>56</sup>)

In the past two decades, fine crystal tuning has been carried out for organic radical cation (anion) salts of BEDT-TTF<sup>10,58</sup> and  $\text{Pd}(\text{dmit})_2$ .<sup>11,59–61</sup> In their crystals, unpaired electrons existing on the intermolecular dimers form triangular lattices. Their triangle shape can be easily modified by changing the counter anions (cations) and is evaluated by the parameter  $t'/t$ , where  $t'$  and  $t$  are the transfer integrals as defined in Figure 1.8. The phase diagram for the  $\text{Pd}(\text{dmit})_2$  radical anion salts shows various phases such as

antiferromagnetic order (AFLO), quantum spin liquids (QSL), and charge order (CO). The solid-state properties can be systematically changed by tuning  $t'/t$ .

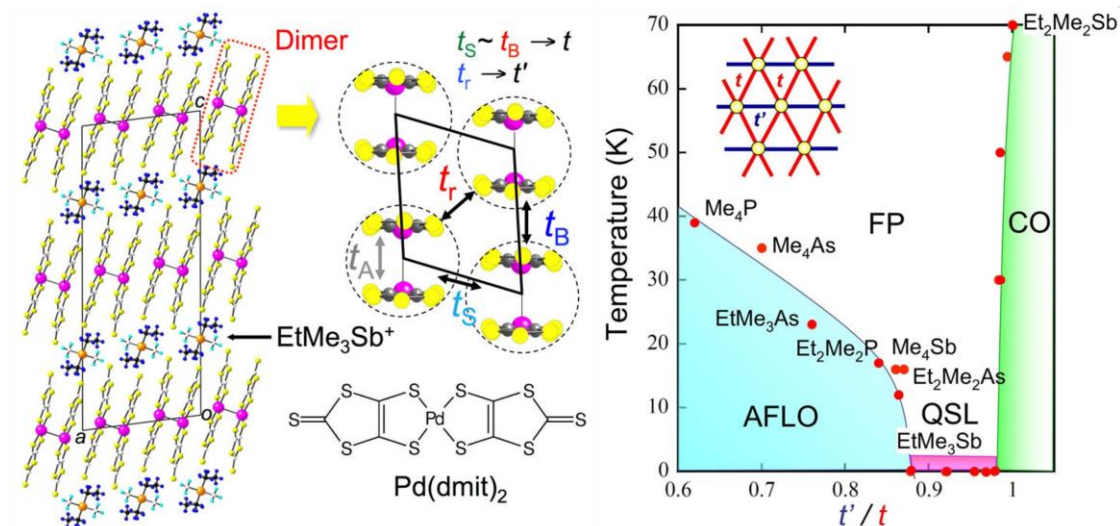


**Figure 1.8.** Crystal structure and phase diagram of the Pd(dmit)<sub>2</sub> radical anion salts. Unpaired electrons which exist on the intermolecular dimers form triangular lattices. (Reproduced from Kato.<sup>61</sup>)

Recently, hydrogen-bond conductors have been developed by Mori et al.<sup>62–64</sup> Figure 1.9 shows the molecular structure of  $\kappa$ -D<sub>3</sub>(Cat-EDT-TTF)<sub>2</sub> and the hydrogen-bond-dynamics-based switching of conductivity and magnetism. This deuterated hydrogen system shows a phase transition at 185 K with significant switching of the electronic and magnetic properties, which is accompanied by a simultaneous electron and deuterium transfer within the hydrogen-bond unit.<sup>64</sup> Since the transition does not take place in  $\kappa$ -H<sub>3</sub>(Cat-EDT-TTF)<sub>2</sub>, the H/D isotope effect on the H-bond geometry and potential energy curve is considered.

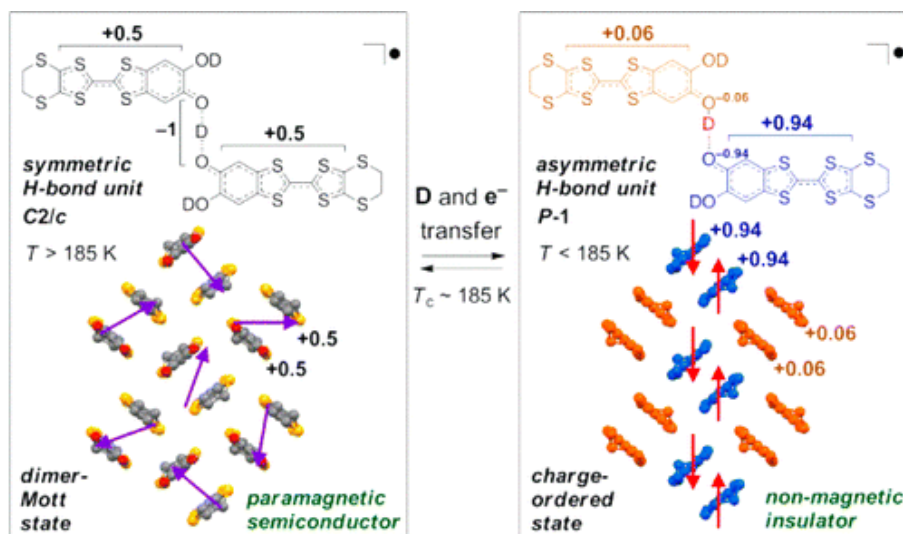


**Figure 1.9.** Hydrogen-bonded molecular unit of  $\kappa\text{-D}_3(\text{Cat-EDT-TTF})_2$  and the hydrogen-bond-dynamics-based switching of conductivity and magnetism. (Reproduced from Ueda et al.<sup>64</sup>)

### 1.3 $K_4$ Crystal: Isotropic 3D Structures

Highly symmetrical structures, such as those of diamonds, seem to hold an inherent attraction for humans. In addition to their aesthetic appeal, however, such structures can confer properties such as hardness and thermal conductivity to bulk materials. Among 3D lattices, the  $K_4$  crystal<sup>65</sup> is a special 3D lattice that is mathematically related to the diamond crystal. This structure appears in various fields, and its structural beauty and special properties have been attracting researchers for over eighty years. This chapter focuses on the  $K_4$  crystal, beginning with a description of its mathematical aspect. Then, the structure and the diversity in real systems are described.

Graph theory indicates a special high symmetry of the  $K_4$  crystal from the view point of mathematics.<sup>65,66</sup> Two properties, “maximal symmetry” and “strong isotropic property”, characterize the  $K_4$  crystal. The name,  $K_4$ , comes from the complete graph  $K_4$ ,

which consists of four vertices, each pair of which is connected by a unique edge. A mathematical operation, “periodic realization”, transforms this type of absolute graph to a crystal lattice, and “standard realization”, which is one of the periodic realizations, realizes the  $K_4$  crystal. It is proven that the most symmetrical structure is obtained by standard realization and the realized crystal has maximal symmetry among all the periodic realizations; any structural deformation of the arrangement in the crystal reduces the symmetry. In addition to maximal symmetry, the  $K_4$  crystal is characterized by a strong isotropic property. In Figure 1.10, honeycomb and square lattices are compared to describe this strong isotropic property. If there are congruent transformations preserving the crystal net after swapping any two edges with the same origin while fixing the other edges, the lattice will exhibit the strong isotropic property. Thus the honeycomb lattice has this property, but the square lattice does not. Indeed, Sunada showed that only four kinds of structures have maximal symmetry and a strong isotropic property in 2D and 3D crystal nets: honeycomb lattice,  $K_4$  crystal, mirror image of the  $K_4$  crystal, and diamond crystal. The  $K_4$  crystal has a special high symmetry crystal net among 3D lattices and is called a diamond twin.

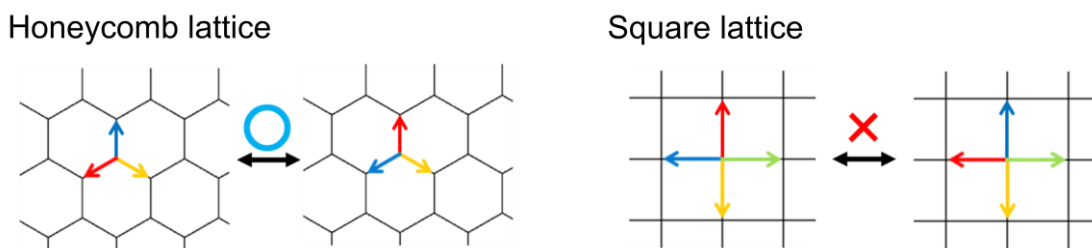


**Figure 1.10.** Description of the strong isotropic property.

Sunada proposed a new carbon allotrope,  $K_4$  carbon, as a possible realization of the  $K_4$  crystal in nature.<sup>65,67</sup> Figure 1.11 shows the crystal structure of the  $K_4$  carbon and

its local structure. The  $K_4$  carbon has a chiral structure of the cubic space group of  $I4_132$ , consisting of trivalent  $sp^2$  carbons. Each  $sp^2$  plane consisting of four carbon atoms has a twisting connection with the nearest  $sp^2$  planes with a torsion angle of  $\pm\cos^{-1}(1/3)$  ( $\sim \pm 70.5^\circ$ ). This 3D structure has interconnected decagonal rings with a huge 3D cavity, and the number of rings meeting at each vertex is fifteen. After the description of the  $K_4$  carbon by Sunada, theoretical calculations on the  $K_4$  carbon predicted its striking properties. The band calculation of the  $K_4$  carbon predicted a metallic ground state<sup>67</sup> in spite of the insulating properties of diamond. Moreover, the appearance of the Dirac cones in the band structure has also been reported.<sup>68,69</sup> However, the electronic properties of the  $K_4$  carbon have not been investigated due to the difficulty of the synthesis; the  $K_4$  carbon was first described as a metastable allotrope by Itoh et al.,<sup>67</sup> and then the structural instability was pointed out by the phonon band calculation.<sup>70</sup>

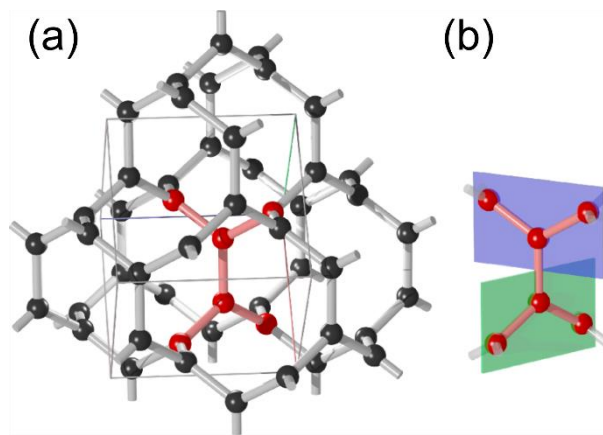


**Figure 1.11.** (a) Crystal structure of the  $K_4$  carbon. (b) Local structure in the  $K_4$  carbon.

Beyond the  $K_4$  carbon, the  $K_4$  crystal itself was first discovered by crystallographers and then rediscovered many times in various fields.<sup>71,72</sup> The structure of the crystal was first described by Laves in 1932<sup>73,74</sup> and later named the Laves graph

by Coxeter.<sup>75</sup> It was rediscovered by Wells and called Net 1((10,3)-a).<sup>76,77</sup> The srs net is also used to describe the structure, which is named after the  $K_4$  structure of the Si networks in  $\text{SrSi}_2$ .<sup>78,79</sup> The srs net is strongly related to the gyroid, or G surface, which is a triply periodic minimal surface discovered by Shoen.<sup>80</sup> Figure 1.12(a) shows the relationship between the gyroid and the channel structure. The gyroid separates the space into a pair of enantiomorphic channels, and the chiral channel corresponds to the srs net with different chirality. The gyroid itself belongs to the cubic space group of  $Ia\bar{3}d$  if there is no distinction between the front and back side of the surface. The srs net is ubiquitous<sup>71</sup> in nature and appears in such fields as mathematics, biology, and materials chemistry. This structure has been reported in naturally occurring and synthetic architectures of various sizes, such as mesoporous silicate (MCM-48),<sup>81-83</sup> lipid-water systems,<sup>84</sup> block copolymers,<sup>85-87</sup> photonic crystals,<sup>88</sup> and butterfly wings.<sup>89</sup> Recently, tensile and compressive tests were also carried out for 3D-printed gyroid<sup>90</sup> toward a possible application of the gyroid as a lightweight material with high strength.

In the field of chemistry, Si networks of  $\text{SrSi}_2$ ,<sup>78,79</sup> cg-N,<sup>91</sup> and metal organic frameworks such as metal-oxalate complexes,<sup>92</sup> are known to form the srs net, but the theoretical predictions for the  $K_4$  carbon have not been experimentally confirmed for these materials. The band structure of  $\text{SrSi}_2$  is affected by Sr, and it is regarded as a narrow gap semiconductor.<sup>93</sup> cg-N is synthesized from elemental nitrogen under high pressures and high temperatures, and is metastable at ambient conditions. Metal-oxalate complexes have been investigated as molecular magnets<sup>94</sup> and considered as localized-electron systems since the metal centers are separated by oxalate ligands. Though the srs net is ubiquitous in various fields, it is still challenging to form this structure on a molecular scale and to examine the theoretical predictions on the  $K_4$  carbon.

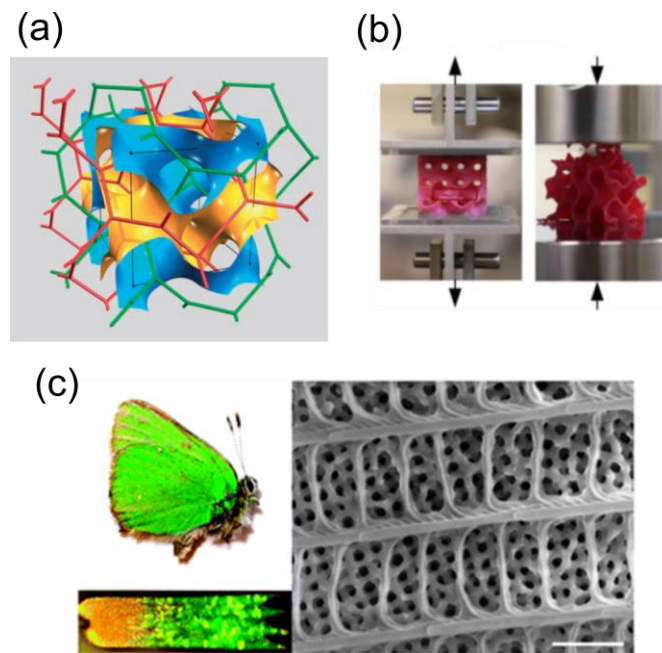


**Figure 1.12.** (a) Relationship between the gyroid and the channel structure (green and red). (b) 3D-printed gyroid sample under the tensile and compressive tests. (c) *C. rubi* with its green wings and the SEM micrograph of the top of the wing scale. The 3D gyroid structures are found below the longitudinal ridges. The scale bar is 1  $\mu\text{m}$ . (Reproduced from (a) Hyde et al.,<sup>71</sup> (b) Qin et al.,<sup>90</sup> and (c) Mille et al.<sup>89</sup>)

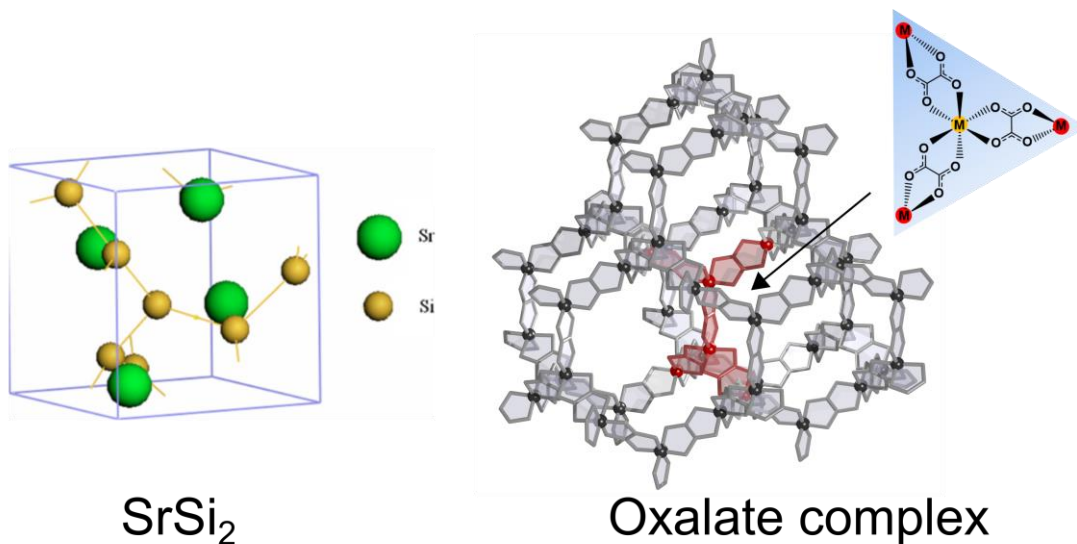


**Figure 1.13.** Crystal structures of  $\text{SrSi}_2$  (left) and oxalate complexes (right). (Left figure reproduced from Chen et al.<sup>93</sup>)

## 1.4 Geometrical Spin Frustration and Quantum Spin Liquid States

Research on magnetic materials has been extensively devoted to the development of materials with magnetic ordering. Recently, however, physicists and chemists have also researched spin frustration that could realize quantum fluctuated non-ordered states from the viewpoint of fundamental solid-state physics.<sup>95</sup> Figure 1.14(a) shows a simple description of geometrical spin frustration in the Ising model. Nearest-neighbor spin pairs with antiferromagnetic interactions on a triangle cannot take an energetically favorable, ordered spin alignment due to the geometrical limitation caused by the triangle shape; the pairs have six possible spin alignments on it. This type of magnetic frustration is called geometrical spin frustration. In the case of the Heisenberg model, spins on a triangle can yield 120-degree structures and show two types of spin alignment, which are characterized by (+) and (-) chirality as shown in Figure 1.14(b). In any case, the magnetic ground states are degenerated.

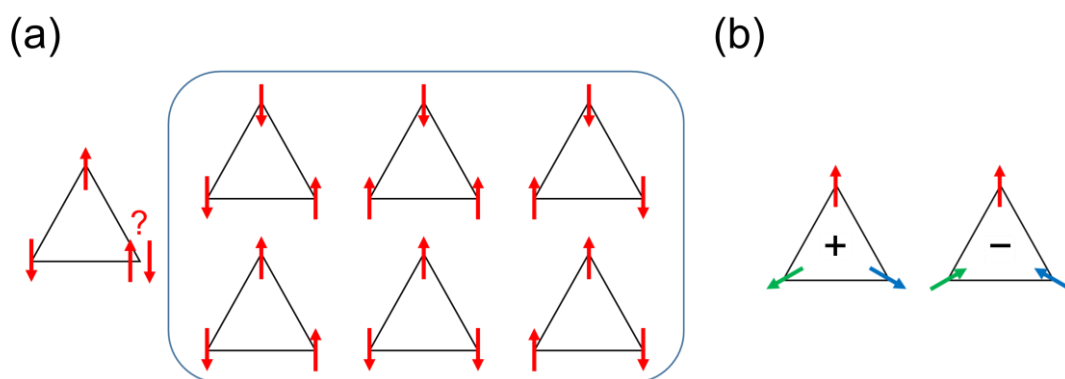


**Figure 1.14.** Spins with nearest-neighbor antiferromagnetic interactions on a triangle in the Ising model (a) and in the Heisenberg model (b).

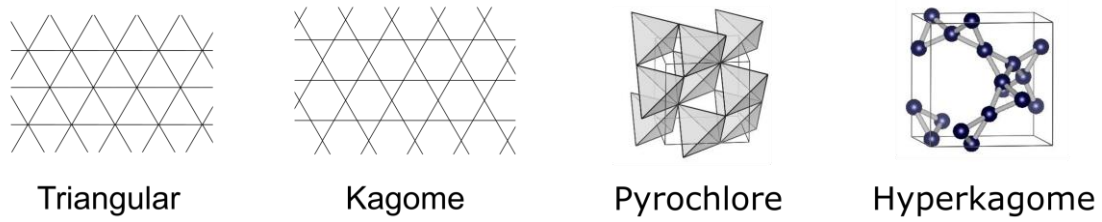


**Figure 1.15.** Magnetic lattices with spin frustration caused by spins with nearest-neighbor antiferromagnetic interactions. A part of this figure is made by VESTA.<sup>96</sup>

Figure 1.15 shows magnetic lattices with spin frustration caused by spins with nearest-neighbor antiferromagnetic interactions. Edge-sharing triangles or corner-sharing triangles are included in these lattices. The lattices with corner-sharing triangles are considered to be more frustrated due to the small number of neighboring spins. Figure 1.16 shows two of the possible spin alignments in a kagome lattice with antiferromagnetic coupled Heisenberg spins. Due to the spin chirality, the spin alignment in a kagome lattice is infinite. This corresponds to highly degenerated ground states, which are no longer magnetically ordered even at the absolute zero temperature. This kind of the fluctuated magnetic states is called spin liquid state. More specifically, spin liquid state characterized by quantum fluctuation of spins with small spin quantum number, is called quantum spin liquid state.

One of the quantum spin liquid states, the resonating valence bond (RVB) state, was described as an alternative state to the Neel antiferromagnetic state for triangle lattices by Anderson in 1972.<sup>97</sup> The RVB state is a non-magnetic degenerated state, which is described as a superposition of spin-singlet pairs. Many experimental and theoretical studies have been devoted to frustrated magnets,<sup>31,32,63,98–124</sup> but the direct observation of quantum spin liquid states was not achieved until 2003, when Shimizu et al. performed <sup>1</sup>H NMR measurement of a spin liquid state in an organic Mott insulator  $\kappa$ -(BEDT-

$\text{TTF})_2\text{Cu}_2(\text{CN})_3$  with a triangle lattice.<sup>99</sup> This NMR measurement indicated that there was no long-range magnetic ordering even at 32 mK, which is four orders of magnitude lower than the energy scale of the magnetic interactions. In the last two decades, candidates for quantum spin liquids have been investigated from various points of view, such as neutron diffraction,  $\mu\text{SR}$ , and heat-capacity measurements. However, the nature of quantum spin liquid states is still a matter of debate.<sup>125</sup> In particular, the gapped and/or gapless nature of quantum spin liquid states has been widely discussed. For example, heat-capacity measurements for many of the candidates have revealed degenerated ground states characterized by the finite linear heat-capacity coefficient  $\gamma$ , indicating the gapless nature of spin liquids.<sup>32,95,125</sup> On the other hand, a gapped nature was observed for an organic candidate,  $\kappa\text{-(BEDT-TTF)}_2\text{Cu}_2(\text{CN})_3$ , by thermal conductivity measurements.<sup>122</sup>

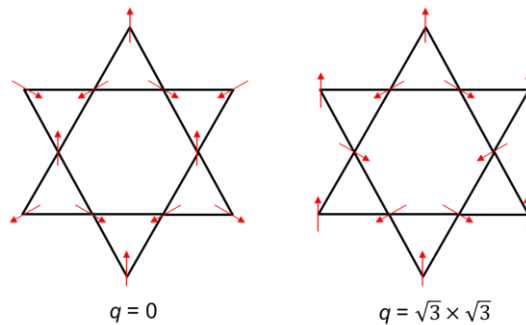


**Figure 1.16.** Two of the possible spin alignments in a kagome lattice with antiferromagnetic coupled Heisenberg spins.

Ideal experimental models are crucial for elucidating the nature of quantum spin liquids. Many of the candidates thus far are inorganic materials with 2D triangular and kagome lattices.<sup>98–100,103–115</sup> In the 2D systems, the features of quantum spin liquid states are affected by minor effects such as structural deformations from equilateral triangles,

and interlayer interactions between the 2D lattices as shown in Figure 1.17.<sup>108,119–121</sup> On the other hand, 3D frustrated systems are still very rare due to the difficulty of their preparation.  $\text{Na}_4\text{Ir}_3\text{O}_8$ <sup>101</sup> is a well-known 3D frustrated system with a hyperkagome lattice of corner-sharing  $\text{Ir}^{4+}$  ions with  $S = 1/2$  spins, while magnetic anisotropy caused by spin-orbit coupling governs the spin ground states of this material.<sup>102</sup> The effects of heavy elements such as Ni, Cu, and Ir are problematic for the search of spin liquids irrespective of the lattice dimensions.<sup>102,123,124</sup> All the effects described above sometimes induce long-range magnetic ordering and could affect the spin ground states. 3D organic frustrated magnets with isotropic Heisenberg spins, which should be an ideal experimental model without these effects, have not been reported yet.

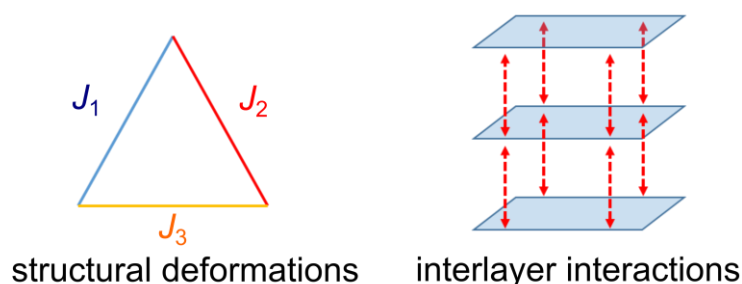


**Figure 1.17.** Structural deformations and interlayer interactions in 2D lattices.

## 1.5 Polyhedral $\pi$ Acceptors of Naphthalene-Diimide-Based Rigid Cyclophanes

Naphthalene diimide (NDI) is one of the aromatic cyclic diimides which are widely used as electron-accepting molecules.<sup>126–129</sup> NDIs can be synthesized by a simple one-step reaction as shown in the bottom of Figure 1.18. NDIs are prepared by the reaction of 1,4,5,8-naphthalenetetracarboxylic dianhydride (NDA) with appropriate



1.19(c)).<sup>135,136</sup> Complex macrocycles including trefoil knots were synthesized based on the equilibrium of reversible disulfide reactions. These studies indicate the diversity of NDI-based cyclophanes.

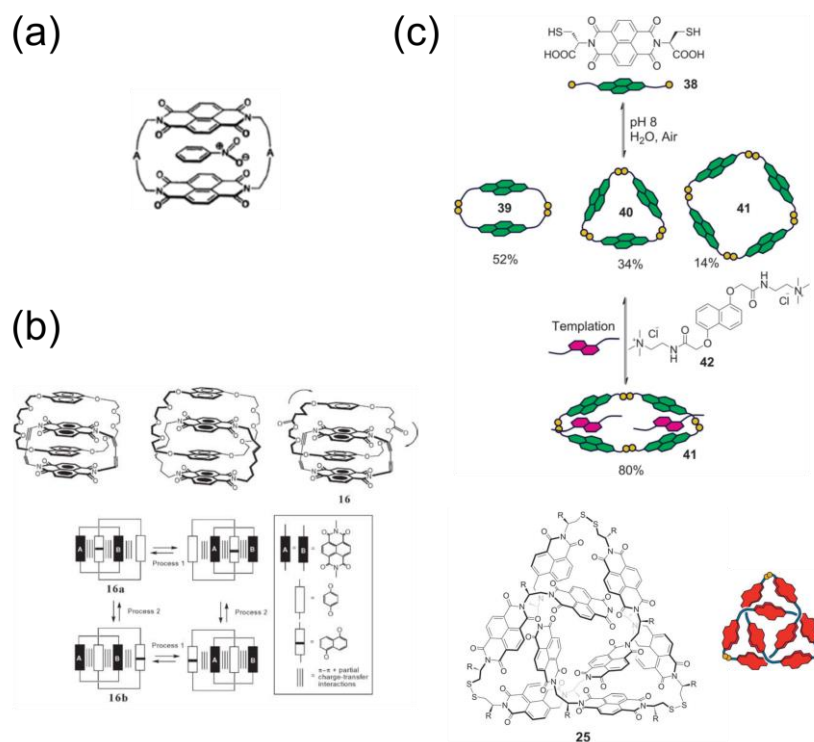


**Figure 1.19.** Molecular recognition by NDI-based cyclophanes. (Adapted from (a) Jazwinski et al.,<sup>131</sup> and (c) Black et al.<sup>135</sup> Reproduced from (b) Bhosale et al.<sup>126</sup>)

NDI-based rigid cyclophanes with a shorter linker (one or two atoms in length) are important to investigate the electronic communication within the macrocycles. In 2002, Gawroński et al. reported PyDI-based chiral rigid cyclophanes using a chiral trans-cyclohexanediamine as a linker.<sup>137</sup> The synthesized cyclic dimer and trimer have a well-defined rigid structure and indicate the potential of the diamines for cyclophane synthesis. In the past five years, Stoddart et al. have been developing aromatic cyclic diimide-based rigid cyclophanes using the same diamines in order to investigate the electronic

communication within the macrocycles.<sup>138–148</sup> Figure 1.20 shows the molecular structures of their rigid cyclophanes. These molecules have a chirality ((–) or (+)) that is dependent on the chirality of the cyclohexanediamines ((1*R*,2*R*) or (1*S*,2*S*)).

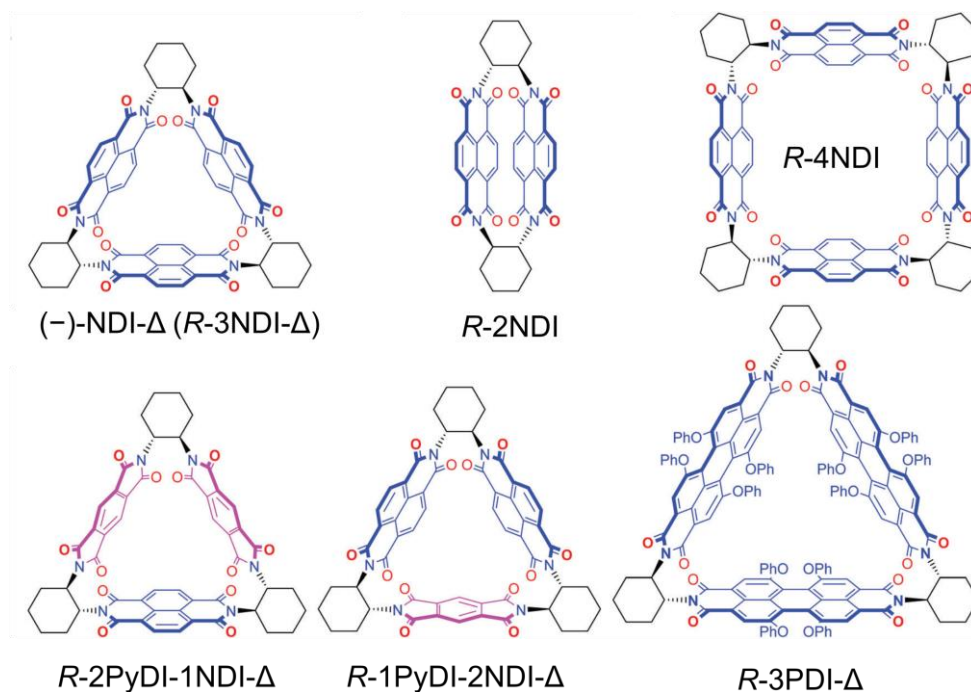


**Figure 1.20.** Molecular structures of aromatic diimide-based chiral rigid cyclophanes. (Adapted from Liu et al.<sup>148</sup> The compound names are added.)

Among the rigid cyclophanes, the NDI-based cyclophanes, (–)-NDI-Δ, 2NDI, and 4NDI, have been extensively investigated. Figure 1.21(a) shows the LUMO of (–)-NDI-Δ. This calculation predicts a through-space interaction among the three NDI units. The CV and EPR measurements provide evidence of the electron sharing for these three cyclophanes. Figure 1.21(b) shows the cyclic voltammograms of the NDI-based cyclophanes. The first redox potential for (–)-NDI-Δ is shifted to a higher potential than that for Ref-NDI, indicating the enhancement of the electron-accepting ability through the through-space interaction. In addition, six distinct redox states are observed for (–)-

NDI- $\Delta$ , as two electrons are accepted per NDI moiety. Six is an unusually large number for such a relatively small organic molecule. The degree of the potential shifts reflects the strength of the intramolecular interactions ( $2\text{NDI} > (-)\text{-NDI-}\Delta > 4\text{NDI}$ ), and is negligibly small for 4NDI. The EPR spectra in their mono-reduced states also indicate an electron delocalization within the macrocycles (Figure 1.21(c)). Multiple redox states along with the accessible intramolecular cavity of  $(-)\text{-NDI-}\Delta$  are also investigated to examine the potential of  $(-)\text{-NDI-}\Delta$  as an active material for lithium-ion batteries, and these experiments reveal that  $(-)\text{-NDI-}\Delta$  shows higher cyclic performance than Ref-NDI.<sup>144</sup>

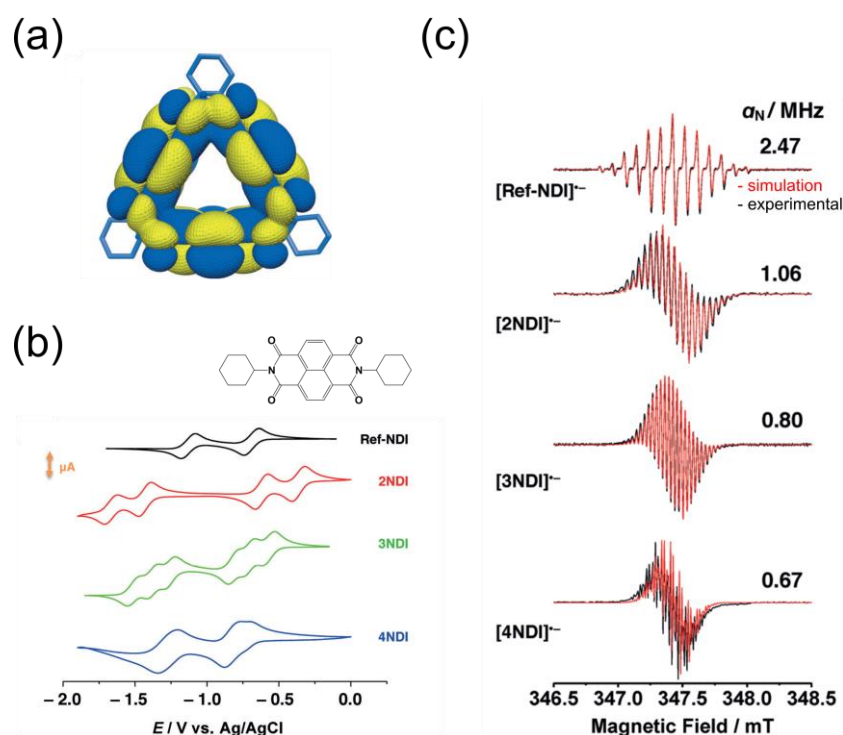


**Figure 1.21.** (a) Through-space interaction in the LUMO of  $(-)\text{-NDI-}\Delta$ . (b) Cyclic voltammograms of the NDI-based cyclophanes. (c) EPR spectra of the NDI-based rigid cyclophanes in their mono-reduced states. In (b) and (c), the spectra of the reference compound (Ref-NDI) are shown for comparison. ((a) Reproduced from Schneebeli et al.<sup>138</sup> (b) and (c) Adapted from Wu et al.<sup>140</sup> The molecular structure of Ref-NDI (b) and the explanation of the red and black traces (c) are added.)

The characteristic triangular shape of (-)-NDI- $\Delta$  with a cavity space is useful as a building block for supramolecular crystals. Figure 1.22 shows two supramolecular structures formed by (-)-NDI- $\Delta$ . In Figure 1.22(a), a 1D helical structure is induced by anion- $\pi$  interactions between  $I_3^-$  and (-)-NDI- $\Delta$ .<sup>138</sup> The chirality of the helical chains is transferred from the molecular chirality. In Figure 1.22(b), 1D supramolecular nanotubes are also formed from the columnar stacking of (-)-NDI- $\Delta$ , which is induced by halogen bonding interaction of 1,2-dihalohydrocarbons inside the nanotube, lateral [X- $\pi$ ] or [ $\pi$ - $\pi$ ], and C-H $\cdots$ O interactions between the triangles.<sup>141</sup>

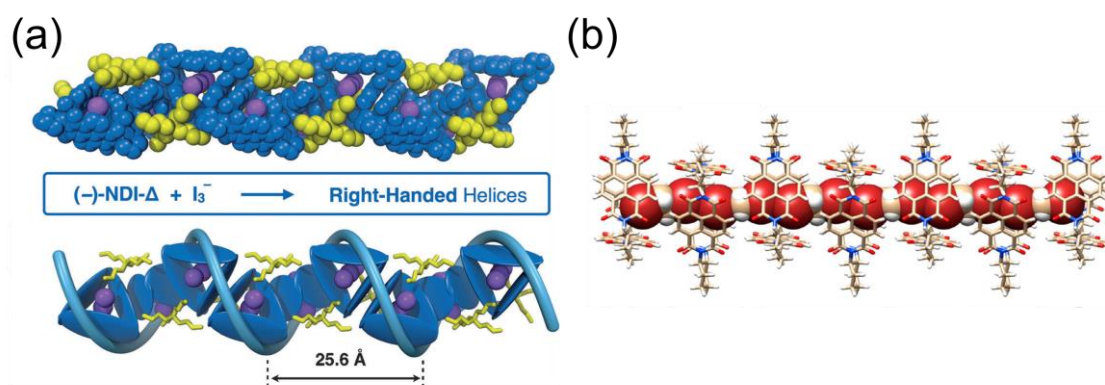


**Figure 1.22.** (a) 1D helical structure induced by anion- $\pi$  interactions. (b) 1D supramolecular nanotubes induced by halogen-bonding interactions. (Reproduced from (a) Schneebeli et al.<sup>138</sup> (b) Adapted from Liu et al.<sup>141</sup>)

The enhanced accepting ability of the NDI-based cyclophanes is suitable for the preparation of radical anion salts. So far, there are few examples of structurally characterized radical anion salts of NDIs,<sup>139,147,149–151</sup> probably due to the instability of the radical anion salts in air; the first redox potential of Ref-NDI (-1.24 vs. Fc/Fc<sup>+</sup>)<sup>138</sup> indicates the weaker accepting ability of typical NDIs compared to C<sub>60</sub> (-0.99 V)<sup>152</sup> and *p*-benzoquinone (-0.91 V,<sup>153</sup> converted from SCE to Fc/Fc<sup>+</sup> by subtracting 0.4 V<sup>154</sup>).

Kumar et al. demonstrated that the radical anion salts of NDIs can be stabilized by a zwitterionic form using phosphonium-substituted NDIs, as shown in Figure 1.23(a).<sup>149</sup> Use of the NDI-based cyclophanes is an alternative way to obtain stable radical anion salts. 2NDI and (-)-NDI- $\Delta$  were reduced by chemical reduction, and the structures of the radical anion salts were revealed in their dianion and triradical trianion states, respectively.<sup>139,147</sup> In these crystals, there is no significant  $\pi$ - $\pi$  interaction between the cyclophanes.

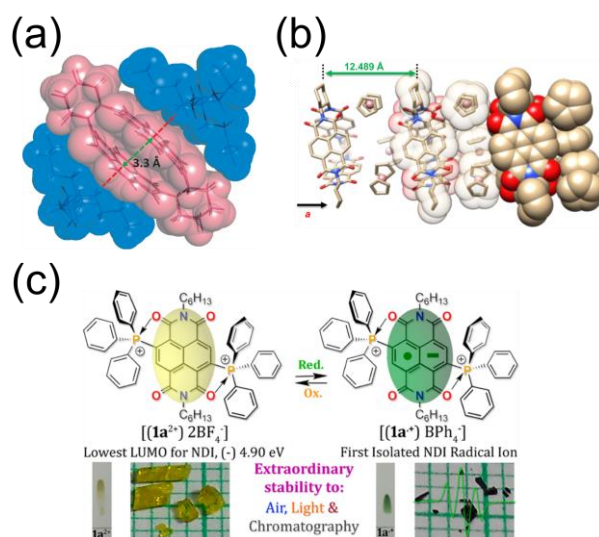


**Figure 1.23.** (a) Stable radical anion salts of NDIs stabilized by a zwitterionic form using phosphonium-substituted NDIs. Crystal structures of the radical anion salts of 2NDI (b) and (-)-NDI- $\Delta$  (c). (Reproduced from (a) Kumar et al.,<sup>149</sup> (b) Schneebeli et al.,<sup>139</sup> and (c) Liu et al.<sup>147</sup>)

## 1.6 Motivation and Scope of This Thesis

A large body of research on molecular conductors and magnets has revealed that the solid-state properties are strongly dominated by the dimensionality and packing in the

crystals. Most of the attempts to control the crystal structures, however, have been limited to the modulation of intermolecular arrangements based on the obtained crystal structures, and major structural control that includes the crystal symmetry has proven difficult. If it is possible to generate the desired crystal structures in a controlled manner, the solid-state properties can be quickly searched in a logical way. Thus, the theoretical predictions in physics can be directly connected to the syntheses in materials chemistry. Exotic physical properties such as Dirac cones and quantum spin liquid states are strongly related to highly symmetrical structures such as honeycomb and triangular lattices. 3D structures in particular have the potential to exhibit interesting properties as in  $C_{60}$ , but these structures are difficult to produce due to the strong tendency toward the 1D stacking interaction of planar aromatic molecules. Recently,  $\pi$ -extended double helicenes, which exhibit 3D lamellar stacking due to their curved structures, were reported by Fujikawa et al.<sup>155,156</sup> Their work clearly indicated the importance of non-planar aromatic molecules for the realization of 3D  $\pi$ - $\pi$  interactions.

This thesis focuses on the 3D  $K_4$  crystal which has a strong mathematical relationship (strong isotropic property) with a honeycomb lattice. The  $K_4$  crystal is expected to be an interesting and novel platform for solid-state physics due to its predicted properties, which include a metallic state and Dirac cones. The chiral (-)-NDI- $\Delta$  molecule is expected to be suitable as a building block for highly symmetrical 2D and 3D structures due to its rigid triangular shape with polyhedral aromatic rings. The strong electron-accepting ability of (-)-NDI- $\Delta$  is also important for the synthesis of radical anion salts. Moreover, the characteristic triangular shape provides an opportunity to investigate 3D organic frustrated magnets.

In Chapter 1, the general introduction of this thesis is given. The history of molecular conductors and magnets, including crystal engineering, the 3D  $K_4$  crystal, concepts of spin frustration and quantum spin liquid states, and the recent development of NDI-based rigid cyclophanes are described. In Chapter 2, the preparation and the electronic and magnetic properties of radical anion salts of (-)-NDI- $\Delta$  are described. The radical anion salts of (-)-NDI- $\Delta$  are prepared by electrochemical reduction, and the 3D  $K_4$  crystals are revealed by single-crystal X-ray analysis. The crystal components are examined in detail by IR and ICP measurements, and elemental analysis. The band structure of the obtained  $K_4$  crystal is calculated, and the electronic and magnetic properties are investigated. In Chapter 3, spin-frustrations in the hyperkagome lattices formed in the  $K_4$  crystals are discussed. The spin lattice of the  $K_4$  crystal is discussed, based on the results of the valence, the electronic properties, and the calculations. Hyperkagome lattices in the  $K_4$  crystals are revealed, and the spin frustration is investigated by magnetic susceptibility, NMR, and heat-capacity measurements. In Chapter 4, novel 3D chiral crystals of radical anions of (-)-NDI- $\Delta$  are described. Novel 3D crystals of radical anions of (-)-NDI- $\Delta$  are prepared by electrochemical reduction with cyclic multidendate ligands such as crown ethers and cryptands. These structures are solved by X-ray analysis, and the electronic and magnetic properties are examined. In Chapter 5, supramolecular crystals of CT complexes of (-)-NDI- $\Delta$  are described. CT complexes of (-)-NDI- $\Delta$  are prepared with various donor molecules, and the crystal structures with different dimensionality are solved by X-ray analysis. CT interactions between donors and (-)-NDI- $\Delta$  are also examined by UV-VIS-NIR diffuse reflectance measurements. Finally, this thesis is summarized in Chapter 6.

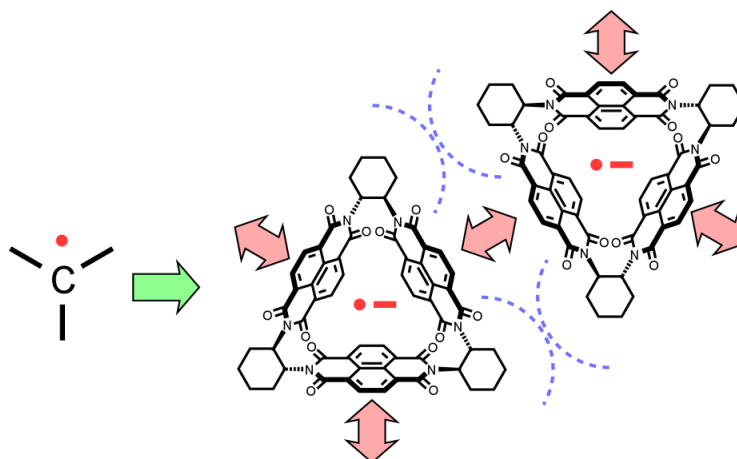
# Chapter 2 Preparation, Electronic and Magnetic Properties of Radical Anion Salts of (-)-NDI- $\Delta$ : Construction of Molecular 3D $K_4$ Crystals

## 2.1 Introduction

As described in Section 1.4, the predicted electronic properties of the  $K_4$  carbon<sup>67-</sup><sup>69</sup> are very interesting in comparison with those of diamond. Although several metal-oxalate complexes are known to form the  $K_4$  crystals,<sup>92,94</sup> their localized-electron nature is not suitable for investigating the electronic properties. Synthesis of the  $K_4$  carbon, however, has not been successful probably due to the instability, which was predicted by the imaginary modes in the phonon band structure.<sup>70</sup> In order to prepare the  $K_4$  crystals with delocalized electrons, the exchange interactions through  $\pi$  overlaps are useful. In this perspective, a triangular  $\pi$  molecule, (-)-NDI- $\Delta$ ,<sup>138</sup> has a promising molecular structure. Scheme 2.1 shows a strategy for preparation of  $K_4$  crystals. The exchange interactions between the radical anions of (-)-NDI- $\Delta$  can realize 3-way intermolecular interactions. In addition, the steric hindrance caused by the bulky cyclohexane moieties may prevent an eclipsed  $\pi$  overlap and may make a twisted  $\pi$  overlap, which is also a key factor to produce the  $K_4$  structure.

In Chapter 2, the author firstly describes the preparation of the radical anion salts of (-)-NDI- $\Delta$ . Then, the  $K_4$  structure formed by the radical anions of (-)-NDI- $\Delta$  is revealed, and the detailed analysis of the crystal components is described. The band

structure of the obtained molecular  $K_4$  crystal is also shown, and its fascinating features, which are caused by the triangular shape of  $(-)$ -NDI- $\Delta$ , are revealed. At last, the electronic and magnetic properties of the obtained crystals are described.

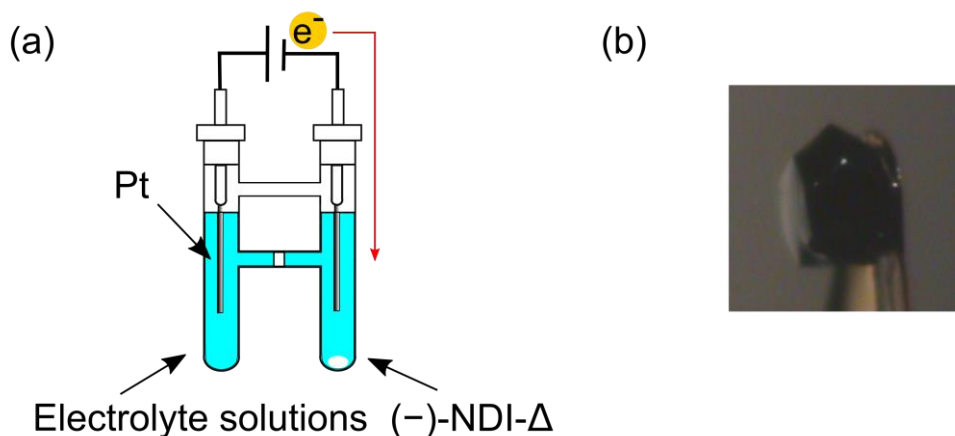


**Scheme 2.1.** Strategy for preparation of  $K_4$  crystals. Comparison between the  $sp^2$  carbon and radical anions of  $(-)$ -NDI- $\Delta$ .

## 2.2 Preparation of Radical Anion Salts of $(-)$ -NDI- $\Delta$

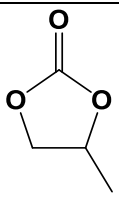
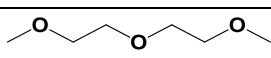
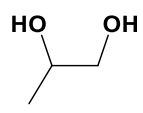
The crystallization of  $(-)$ -NDI- $\Delta$  radical anion salts were conducted by galvanostatic electrocrystallization using H-shaped glass cells equipped with a glass filter and two Pt electrodes (Figure 2.1(a)).  $(-)$ -NDI- $\Delta$  was placed in the cathode side of the glass cells and reduced under a constant current condition. Black block or black needle crystals (Figure 2.1(b)) grew on the cathode in the electrolyte solutions listed in Table 2.1. Propylene carbonate (PC) solutions afforded the most kinds of crystals, while other solvents were also adopted as solvents for the electrocrystallization. Multidentate ligands were used in addition to the alkali metal electrolytes to increase the cation size, and the results are described in Section 4.2. The size and the quality of most of the obtained

crystals were not sufficient for the X-ray structure analysis due to their weak diffraction. Especially, the X-ray analysis for the black needle crystals was always unsuccessful.



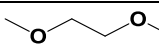
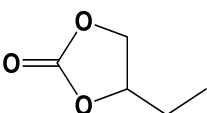
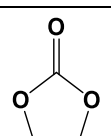
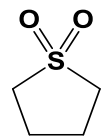
**Figure 2.1.** (a) Electrochemical cell for electrocrystallization. (b) Picture of a single crystal of the Rb salt crystallized in a solution of propylene carbonate.

**Table 2.1.** Crystallization conditions of the (-)-NDI- $\Delta$  radical anion salts.

Solvent	Electrolyte	Crystal habit
 PC	K•ClO <sub>4</sub> , Rb•ClO <sub>4</sub> , Cs•ClO <sub>4</sub> , NH <sub>4</sub> •ClO <sub>4</sub> , Me <sub>4</sub> N•ClO <sub>4</sub> , Et <sub>4</sub> N•ClO <sub>4</sub> , TBA•ClO <sub>4</sub> , TOA•Br, MePy•PF <sub>6</sub> , PPh <sub>4</sub> •I, and TBA•Br	Black block
	Na•ClO <sub>4</sub>	No crystal
 Diglyme	TBA•ClO <sub>4</sub> , Bu <sub>4</sub> P•PF <sub>6</sub> , Pr <sub>4</sub> N•I, PPh <sub>4</sub> •I, MePy•PF <sub>6</sub> , and Pr <sub>4</sub> P•Br	Black block
	NH <sub>4</sub> •ClO <sub>4</sub> , Cs•ClO <sub>4</sub> , Et <sub>4</sub> N•ClO <sub>4</sub> , and Bu <sub>4</sub> P•Br	No crystal
 Propylene glycol	K <sub>2</sub> (COO) <sub>2</sub> •H <sub>2</sub> O, K•ClO <sub>4</sub> , PPh <sub>4</sub> •I, TOA•Br, and MePy•PF <sub>6</sub>	Black block
	Rb•ClO <sub>4</sub> , and TBA•ClO <sub>4</sub>	No crystal
CH <sub>3</sub> CN	TBA•ClO <sub>4</sub> , and MePy•PF <sub>6</sub>	Black block
	Na <sub>2</sub> •(COO) <sub>2</sub>	No crystal

Continue on next page

**Table 2.1. (Continued)**

Solvent	Electrolyte	Crystal habit
 1,2-dimethoxy ethane	TBA•ClO <sub>4</sub> , and MePy•PF <sub>6</sub>	Black block
	NH <sub>4</sub> •ClO <sub>4</sub> , and Cs•ClO <sub>4</sub>	No crystal
 1,2-butylene carbonate	Rb•ClO <sub>4</sub> , and TBA•ClO <sub>4</sub>	Black block
 EC	Rb•ClO <sub>4</sub>	Black needle
 Sulfolane	Rb•ClO <sub>4</sub> , K•ClO <sub>4</sub> , and Li•ClO <sub>4</sub>	Black needle
	K <sub>2</sub> •(COO) <sub>2</sub> •H <sub>2</sub> O, Na <sub>2</sub> •(COO) <sub>2</sub> , TBA•ClO <sub>4</sub> , and PPh <sub>4</sub> •I	No crystal
$\gamma$ -butyrolactone, EtOH, nitromethane, acetone, and 1,4-dioxane		No crystal

### 2.3 X-ray Crystal Structures of Radical Anion Salts

Table 2.2 lists the lattice parameters of the (–)-NDI- $\Delta$  radical anion salts grown in the various electrolyte solutions. All of the crystals belong to the cubic system, having nearly the same lattice parameters between 29.9–30.9 Å. This result suggests that these crystals have an identical structure which is independent of the electrolytes. Especially, the extinction rules for the diffraction data in the PC electrolyte solutions indicate the structures belong to the cubic space group of  $I4_132$ , which is the same as that for the  $K_4$  carbon.<sup>65,67</sup> However, several salts are formed to exhibit the Bravais  $P$ , instead of  $I$ .

**Table 2.2.** Lattice parameters of the (–)-NDI- $\Delta$  radical anion salts grown in the various electrolyte solutions. All of the crystals belong to the cubic systems with the Bravais *P* or *I*.

PC			Diglyme		
Electrolyte	<i>a</i> / Å	Bravais	Electrolyte	<i>a</i> / Å	Bravais
Rb•ClO <sub>4</sub>	30.582(3)	<i>I</i>	TBA•ClO <sub>4</sub>	30.0813(6)	<i>P</i>
NH <sub>4</sub> •ClO <sub>4</sub>	30.914(9)	<i>I</i>	Bu <sub>4</sub> P•PF <sub>6</sub>	30.2286(6)	<i>P</i>
Me <sub>4</sub> N•ClO <sub>4</sub>	30.755(5)	<i>I</i>	Pr <sub>4</sub> N•I	30.5952(8)	<i>P</i>
TBA•ClO <sub>4</sub>	30.74(6)	<i>I</i>	Pr <sub>4</sub> P•Br	29.9474(5)	<i>P</i>
MePy•PF <sub>6</sub>	30.881(4)	<i>I</i>	Propylene glycol		
K•ClO <sub>4</sub>	30.524(4)	<i>I</i>	K <sub>2</sub> (COO) <sub>2</sub> • H <sub>2</sub> O	30.5372(10)	<i>I</i>
Cs•ClO <sub>4</sub>	30.6808(6)	<i>I</i>	K•ClO <sub>4</sub>	30.7024(9)	<i>I</i>
Et <sub>4</sub> N•ClO <sub>4</sub>	30.705(6)	<i>I</i>	PPh <sub>4</sub> •I	30.5539(6)	<i>P</i>
Bu <sub>4</sub> P•Br	30.6426(6)	<i>I</i>	TOA•Br	30.2996(6)	<i>I</i>
PPh <sub>4</sub> •I	30.7005(8)	<i>I</i>	1,2-butylene carbonate		
TOA•Br	30.2996(6)	<i>I</i>	TBA•ClO <sub>4</sub>	30.4594(6)	<i>P</i>
1,2-dimethoxyethane			Rb•ClO <sub>4</sub>	30.6888(6)	<i>I</i>
TBA•ClO <sub>4</sub>	30.1466(6)	<i>P</i>			

Though the X-ray structural analyses for these crystals were attempted, counter cations near (–)-NDI- $\Delta$  could be located only for the crystals highlighted in red and blue in Table 2.2. The structures of the TBA (Bu<sub>4</sub>N), Pr<sub>4</sub>P, and Cs salts highlighted in blue could not be refined anisotropically due to a significant disorder of the cations and the low data quality in the high-angle regions. The refinement including cations was successful only for the Rb and TBA salts, grown in the PC and diglyme solutions, respectively. These two salts are highlighted in red in Table 2.2. Since the Rb salt was firstly prepared and analyzed, this chapter focuses on the structure and properties of this salt. The results for the TBA salt are described in Chapter 3. The X-ray analysis revealed the *K*<sub>4</sub> structures of these salts. The X-ray analysis of the Rb salt revealed a 3D network

structure of the radical anions of (–)-NDI- $\Delta$  with a huge 3D cavity and the position of the Rb ions which were coordinated from the oxygen atoms in (–)-NDI- $\Delta$ . However, the refinement for the structure in the cavity was always unsuccessful, probably due to a significant structural disorder within it. Therefore, the electron densities in the cavity were flattened by using the SQUEEZE subroutine of PLATON,<sup>157</sup> and only the 3D framework of the (–)-NDI- $\Delta$  anions and the Rb ions coordinated from the oxygen atoms were refined. This treatment decreased the reliability factor for the SQUEEZED structure (Table 2.3), which confirmed that the primary uncertainties were not caused by the molecular skeleton of (–)-NDI- $\Delta$ , but by the disorder in the large void space. The present data quality and structural analysis are not sufficient for a discussion of the fine molecular structure, but are sufficient to conclude the  $K_4$  structure in the obtained crystals.

**Table 2.3.** Selected crystallographic parameters before and after the SQUEEZE procedure for the Rb salt of (–)-NDI- $\Delta$ .

	non-SQUEEZE	SQUEEZE
$R_1 [I > 2\sigma(I)]$	0.2270	0.1217
$R$ (all data)	0.2594	0.1341
$wR_2$ (all data)	0.5758	0.3552
Goodness of fit	2.083	1.220
Flack parameter	0.057(18)	0.036(14)

The crystallographic data and the asymmetric unit of the Rb salt after the SQUEEZE procedure are shown in Table 2.4 and Figure 2.2, respectively. This crystal belongs to the cubic space group of  $I4_132$ , which is the same as that for the  $K_4$  carbon.

The asymmetric unit consists of one-sixth of (-)-NDI- $\Delta$  and a Rb ion with an occupancy factor of 0.233(3), which is coordinated from the oxygen atoms of (-)-NDI- $\Delta$ . The result means that (-)-NDI- $\Delta$ :Rb = 1:1.4 in average and the composition is Rb<sub>1.4</sub>[(-)-NDI- $\Delta$ ]. Figure 2.3 shows a comparison between the projections of the  $K_4$  structures of carbon and (-)-NDI- $\Delta$  along the [111] and [010] directions, respectively. The former lies along a 3-fold rotation axis and the latter along a 4-fold screw axis. The structures of the (-)-NDI- $\Delta$  radical anions are understood by replacing every sp<sup>2</sup> carbon with a (-)-NDI- $\Delta$ .

**Table 2.4.** Crystallographic data for Rb<sub>1.4</sub>[(-)-NDI- $\Delta$ ] after the SQUEEZE procedure.

Formula	C <sub>60</sub> H <sub>42</sub> N <sub>6</sub> O <sub>12</sub> Rb <sub>1.4</sub>
Formula weight / g mol <sup>-1</sup>	1158.68
Temperature / K	123
Crystal dimensions / mm <sup>3</sup>	0.25 × 0.24 × 0.22
System	Cubic
Space group	<i>I</i> <sub>4</sub> 32 (#214)
<i>a</i> / Å	30.582(3)
<i>V</i> / Å <sup>3</sup>	28602(5)
<i>Z</i>	8
$\rho_{\text{calcd}}$ / g cm <sup>-3</sup>	0.538
$\mu$ (MoK $\alpha$ ) / cm <sup>-1</sup>	5.071
$\lambda$ / Å	0.71075
$2\theta_{\text{max}}$ / °	54.9
Reflections collected	115158
Unique reflections ( $R_{\text{int}}$ )	5478 (0.0574)
Number of parameters	128
Final $R_1$ [ $I > 2\sigma(I)$ ]	0.1217
$wR_2$ (all data)	0.3552
Goodness of fit	1.220
Flack parameter	0.036(14)
Residual electron density / Å <sup>-3</sup>	0.36 e <sup>-</sup>

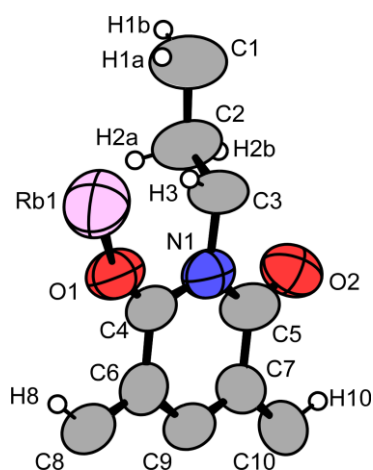


**Figure 2.2.** Asymmetric unit of  $\text{Rb}_{1.4}[(-)\text{-NDI-}\Delta]$ .

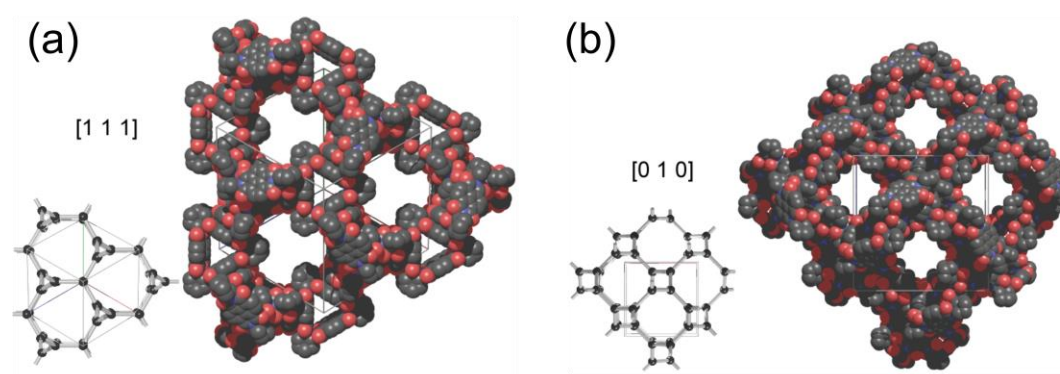


**Figure 2.3.** Comparison between the projections of the  $K_4$  structures of carbon and  $(-)\text{-NDI-}\Delta$ , along the  $[111]$  (a) and  $[010]$  (b) directions. Rb ions coordinated from the oxygen atoms in  $(-)\text{-NDI-}\Delta$  and hydrogen atoms are omitted for clarity.

The obtained  $K_4$  structure has a chirality, depending on the molecular chirality of  $\text{NDI-}\Delta$ ; the left-handed ( $M$ )-helices are stereospecifically formed by  $(-)\text{-NDI-}\Delta$  along the  $[010]$  direction. This kind of chirality transfer is well-known in the chemistry of self-assembly<sup>158</sup> and have already been reported for 1D helical structures of  $(-)$ - and  $(+)$ - $\text{NDI-}\Delta$  (see Figure 1.22).<sup>138</sup> In addition to the chirality transfer, this  $K_4$  structure has a huge 3D cavity with a void fraction of 73% (Figure 2.3), which is comparable with those of metal-organic frameworks (MOFs)<sup>159,160</sup> and covalent-organic frameworks (COFs).<sup>161,162</sup> Figure

2.4 shows the nearest-neighbor intermolecular arrangement in  $\text{Rb}_{1.4}[(-)\text{-NDI-}\Delta]$ . This indicates a twisted  $\pi$ - $\pi$  interaction with an interplanar distance of 3.4 Å and the twisted angle is 70.5°, which is identical to the  $K_4$  carbon. Since the neutral  $(-)\text{-NDI-}\Delta$  doesn't have a  $\pi$ - $\pi$  interaction,<sup>138</sup> this  $\pi$ - $\pi$  interaction is caused by the exchange interaction between the paramagnetic radical anions of  $(-)\text{-NDI-}\Delta$  as expected. This interplanar distance is not as short as those for the so-called “pancake bonds” in radical dimers.<sup>49,50</sup> This suggests a weak  $\pi$ - $\pi$  interaction between the neighboring radical anions of  $(-)\text{-NDI-}\Delta$ . Since the  $\pi$ - $\pi$  interaction exists in all the directions in the same way, this 3D structure is formed only by the unique interaction, which is in clear contrast to most of the organic crystals having various intermolecular interactions like intra- and intercolumnar interactions (Figure 2.5).

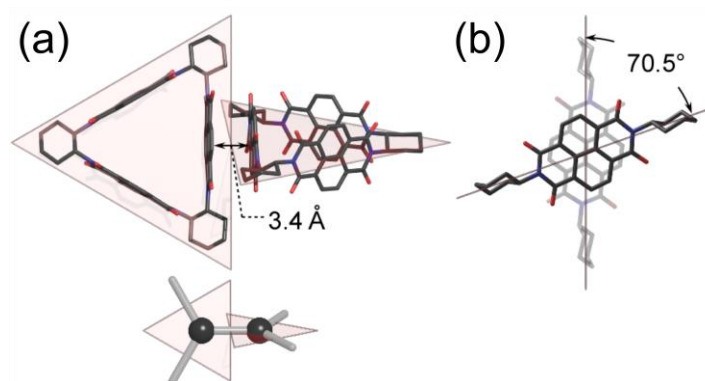


**Figure 2.4.** (a) Nearest-neighbor intermolecular arrangement in  $\text{Rb}_{1.4}[(-)\text{-NDI-}\Delta]$  and the  $K_4$  carbon. (b)  $\pi$ - $\pi$  overlap between the NDI moieties in  $\text{Rb}_{1.4}[(-)\text{-NDI-}\Delta]$ . Rb ions and hydrogen atoms are omitted for clarify.

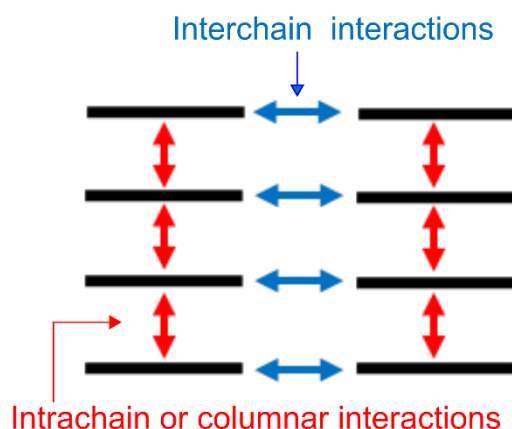


**Figure 2.5.** Intermolecular interactions in conventional organic crystals.

## 2.4 Characterization of Rb Salt

In Section 2.3, the 3D  $K_4$  structure formed by the radical anions of (–)-NDI- $\Delta$  was revealed. In this section, the chemical composition of the Rb salt is discussed, based on the results of elemental analysis and IR, EDX, and ICP measurements.

Figure 2.6 shows the IR spectra for the neutral (–)-NDI- $\Delta$  and its Rb salt. Two peaks around 1677 and 1713  $\text{cm}^{-1}$  are assignable to the C=O stretching vibrations of the cyclic imides. The frequencies of the Rb salt are lower than those of the neutral (–)-NDI- $\Delta$  by ca. 5  $\text{cm}^{-1}$ , which is consistent with the contribution of an antibonding character of the LUMO at the C=O bond of NDI- $\Delta$ . A similar low-frequency shift is observed in other radical anions of NDIs in their solid states,<sup>149,163,164</sup> but the shift of 40–70  $\text{cm}^{-1}$  is much bigger than that for the Rb salt. It could be related to an electron delocalization within the three NDI units and the presence of Rb ions near the carbonyl moieties. Figure 2.7 shows the EDX spectrum for the Rb salt, which indicates that no  $\text{ClO}_4^-$  ion is present in this crystal. The results of the elemental analysis are shown in Table. 2.5. Surprisingly, the elements except for C, H, and N occupy 69.58 wt%. Since the Rb salt has no N source

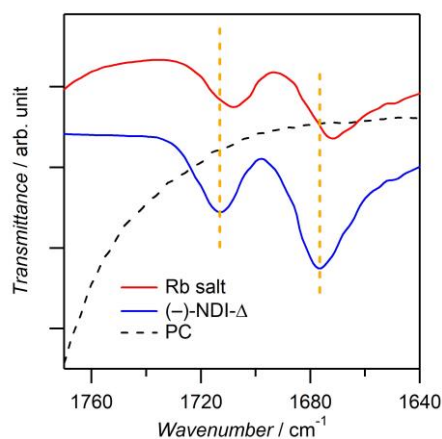


**Figure 2.6.** IR spectra for the neutral (-)-NDI- $\Delta$  and the Rb salt of (-)-NDI- $\Delta$ . Comparison between the C=O stretching vibrations of the neutral (-)-NDI- $\Delta$  and the Rb salt. The C=O stretching vibrations of PC are also shown for comparison.

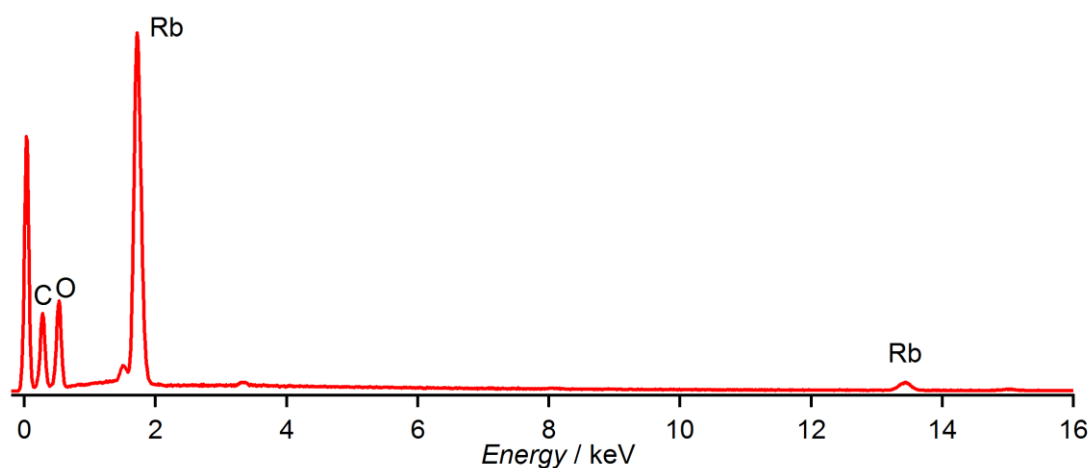
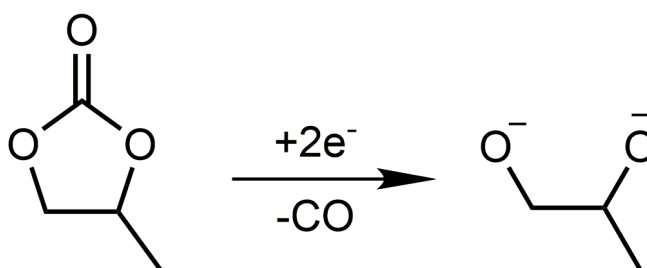


**Figure 2.7.** EDX spectrum for the Rb salt of (-)-NDI- $\Delta$ , indicating no signal of Cl, which usually appears at 2.6 and 2.8 keV.

**Table 2.5.** Results of the elemental analysis of the Rb salt of (-)-NDI- $\Delta$ .

C	H	N	Others
26.52%	2.39%	1.51%	69.58%

except for (-)-NDI- $\Delta$ , the CHN ratios of (-)-NDI- $\Delta$  are calculated as C, 12.95%; H, 0.76%; N, 1.51%. So, the residual CHN ratio is calculated as C, 13.57%; H, 1.63%; N 0%. This analysis indicates a C/H ratio of 8.3, which roughly agrees with that of PC (7.9). Though the result suggests that PC is included in the Rb salt, the actual components for the residual ratios of C and H are not clear. The ICP analysis for Rb ions was carried out for the Rb salt. This analysis revealed (-)-NDI- $\Delta$ : Rb = 1: 40. This abnormal amount of Rb ions is consistent with the large residual elemental ratio of ca. 70%. These results strongly suggest the occurrences of a well-known electrochemical decomposition of PC (Scheme 2.2).<sup>165</sup> The chemical formula is estimated as  $\text{Rb}_{1.4}[(-)\text{-NDI-}\Delta] \cdot 16.8[\text{Rb}_2(\text{propane-1,2-diolate})] \cdot 3.1\text{PC}$  with 26.52% for C, 2.93% for H, and 1.51% for N by assuming that all the decomposed materials are propane-1,2-diolate. Though the actual components in the crystal is still unclear, this type of decomposition reaction might assist the formation of the  $K_4$  structure and the resulting decomposed materials might owe to a structural disorder in the cavity.



**Scheme 2.2.** Electrochemical decomposition of PC into propane-1,2-diolate.

## 2.5 Band Structure of Rb Salt

The band calculation of the Rb salt was carried out, based on the obtained  $K_4$  structure of (-)-NDI- $\Delta$ . Since the three NDI units within the molecule are

crystallographically equivalent, intra- and intermolecular transfer integrals  $t_0$  and  $t_1$  were considered (Figure 2.8(a)). Figure 2.8(b) shows the calculated LUMOs and their energy levels of (-)-NDI- $\Delta$  and NDI dimer calculated by DFT B3LYP/6-31G\* method. The LUMO+1 and LUMO+2 of (-)-NDI- $\Delta$  are degenerated due to a 3-fold rotational symmetry of the molecule. Thus, the energy differences between the LUMO and LUMO+1 corresponded to  $3t_0$  and  $2t_1$  for NDI- $\Delta$  and NDI dimer, respectively. The calculated transfer integrals are summarized in Table 2.6. The absolute value of  $t_1$  is an order of magnitude larger than that of  $t_0$ .

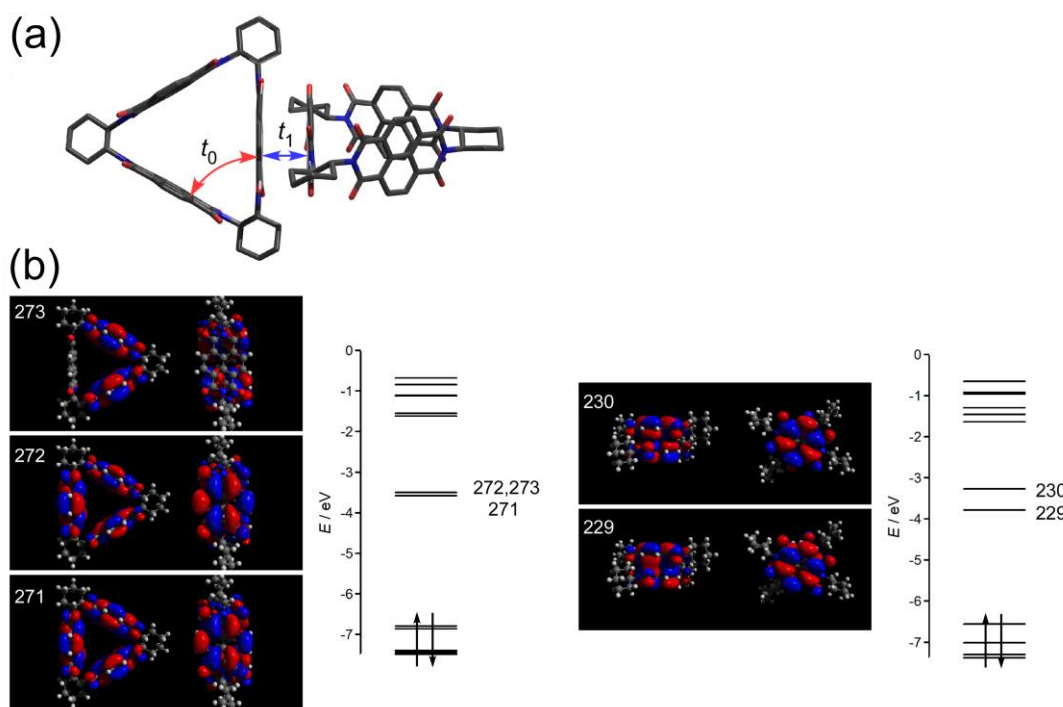


**Figure 2.8.** (a) Definition of the transfer integrals  $t_0$  and  $t_1$ . (b) LUMO and LUMO+1 of (-)-NDI- $\Delta$  and NDI dimer and their energy level diagrams.

**Table 2.6.** Calculation of the transfer integrals in the Rb salt of (-)-NDI- $\Delta$ .

	$E_{\text{LUMO}} / \text{eV}$	$E_{\text{LUMO}+1} / \text{eV}$	$\Delta E / \text{eV}$	$t / \text{eV}$
NDI- $\Delta$	-3.583	-3.497	0.086	-0.029 ( $t_0$ )
NDI dimer	-3.781	-3.266	0.515	-0.258 ( $t_1$ )

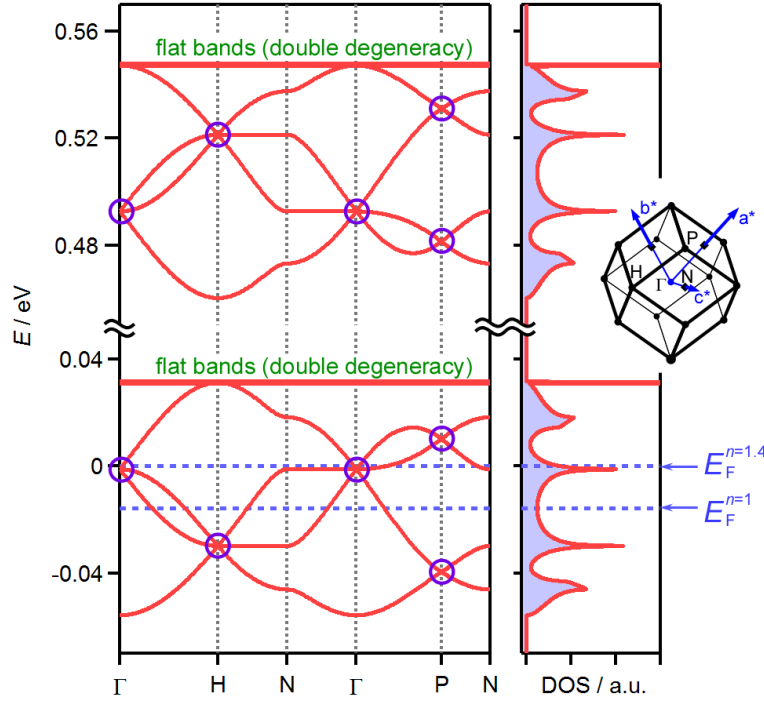


**Figure 2.9.** Band structure and density of states (DOS) for the  $K_4$  structure of the radical anions of (-)-NDI- $\Delta$ . The  $E_F^{n=1}$  and  $E_F^{n=1.4}$  correspond to the Fermi energy for the  $K_4$  structure of  $\text{Rb}[(-)\text{-NDI-}\Delta]$  and  $\text{Rb}_{1.4}[(-)\text{-NDI-}\Delta]$ , respectively. The purple circles indicate the Dirac cones. The inset shows the first Brillouin zone for the band structure.

The band structure was calculated with the tight-binding method by using the obtained transfer integrals. Figure 2.9 shows the band structure and density of states (DOS) for the  $K_4$  structures of the radical anions of (-)-NDI- $\Delta$ . The band widths of the upper six bands and the lower six bands are identical, and correspond to  $3t_0$ . The centers of these two bands are separated by  $2t_1$ . In the mixed valence state of  $n = 1.4$  for  $\text{Rb}_{1.4}[(-)\text{-NDI-}\Delta]$ , the band calculation predicts a metallic ground state and two fascinating features. One is the presence of the Dirac cones at the P,  $\Gamma$ , and H points. Dirac cones are investigated for 2D electronic systems in graphene,<sup>16</sup> BEDT-TTF salt,<sup>17</sup> 3D electronic systems in  $\text{Na}_3\text{Bi}$ ,<sup>166,167</sup> etc. Since the appearance of Dirac cones is not so usual, this system could be a noble experimental platform for Dirac fermions. The other is the

presence of the doubly degenerated flat bands, which suggest a ferromagnetic metal state with a partial occupation. Since the flat bands do not exist in the band structures of the  $K_4$  carbon, they reflect an internal structure of (-)-NDI- $\Delta$ .

## 2.6 Electronic and Magnetic Properties of Rb Salt

The temperature dependence of the conductivity for the Rb salt was measured on a single crystal with a two-probe method (Figure 2.10). The conductivity at 300 K is  $10^{-8}$ – $10^{-9}$  S cm $^{-1}$ , which indicates an insulating property of the Rb salt though a metallic ground state is predicted. The Mott state and/or the random potential in the cavity could owe to this electron delocalization. The small band width of the lower six bands ( $3t_0 = 0.086$  eV) also supports this localization. The thermal activated behavior of the conductivity is fitted by

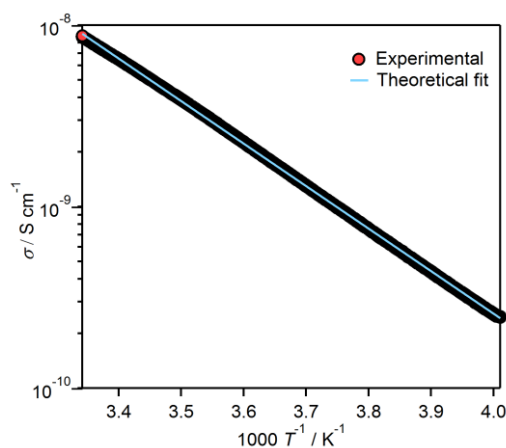


**Figure 2.10.** Temperature dependence of the conductivity for the Rb salt of (-)-NDI- $\Delta$  in the temperature range of 250–300 K. The red circles and blue line indicate the experimental data and the theoretical fit with an activation energy of 0.2 eV, respectively.

$$\sigma = \sigma_0 \exp\left(-\frac{E_a}{k_B T}\right), \quad (2.1)$$

where  $\sigma$ ,  $E_a$ , and  $k_B$  are the conductivity, activation energy, and Boltzmann constant, respectively. The value of  $E_a$  is estimated as 0.2 eV.

The magnetic properties were measured for polycrystalline samples of the Rb salt of (-)-NDI- $\Delta$ . Figure 2.11 shows the temperature dependence of the EPR signals at representative temperatures from 6 to 300 K. The EPR signal exhibited a single Lorentzian absorption at  $g = 2.0035$ , and the intensity increased with decreasing temperature. The temperature dependences of the EPR spin susceptibility, peak-to-peak line width, and  $g$ -factor are shown in Figure 2.12. The line width and the  $g$ -factor depend little on temperature, and the EPR spin susceptibility exhibits a Curie-like behavior. Figure 2.13 shows the temperature dependence of the paramagnetic susceptibility for the Rb salt. This data was fitted by the Curie Weiss law

$$\chi_p = \frac{C}{T - \theta}, \quad (2.2)$$

where  $C$  and  $\theta$  are the Curie and Weiss constants, respectively. The fitting parameters are estimated as follows:  $C = 7.4 \times 10^{-5}$  emu K g<sup>-1</sup> and  $\theta = -10$  K. This negative Weiss constant indicates an antiferromagnetic interaction. The molar Curie constant is estimated as 0.41 emu K mol<sup>-1</sup> by assuming that the chemical formula of Rb<sub>1.4</sub>[(-)-NDI- $\Delta$ ] $\cdot$ 16.8[Rb<sub>2</sub>(propane-1,2-diolate)] $\cdot$ 3.1PC described in Section 2.4. This molar Curie constant roughly agrees with that of the  $S = 1/2$  species (= 0.375 emu K mol<sup>-1</sup>). The Curie-like behavior of the magnetic data indicates the electron localization in this system, which is consistent with the conductivity measurement.

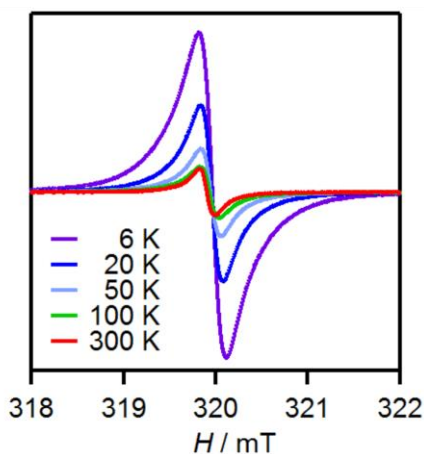


**Figure 2.11.** Temperature dependence of the EPR signals for the Rb salt of (-)-NDI- $\Delta$  at representative temperatures from 6 to 300 K.

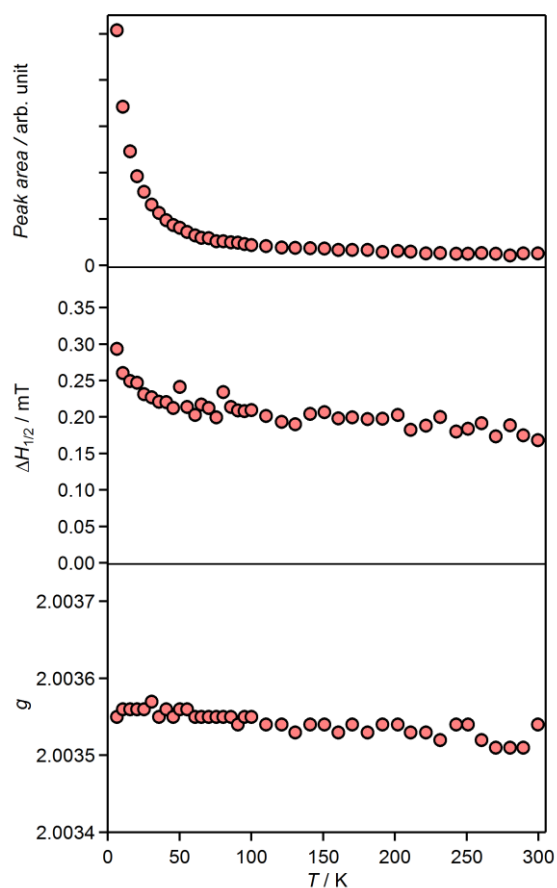


**Figure 2.12.** Temperature dependences of the EPR spin susceptibility, peak-to-peak line width, and g-factor of the EPR signals for the Rb salt of (-)-NDI- $\Delta$ .

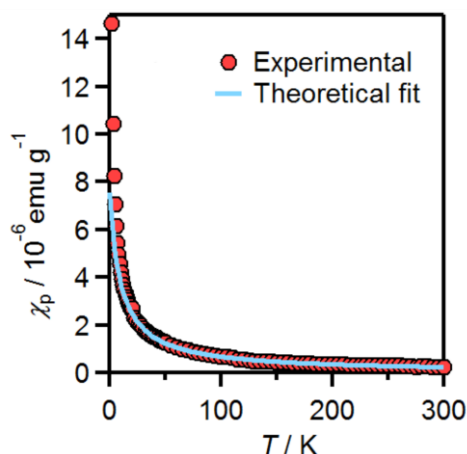


**Figure 2.13.** Temperature dependence of the paramagnetic susceptibility for the Rb salt of (-)-NDI- $\Delta$  in the temperature range of 2–300 K.

## 2.7 Conclusion

Black block crystals of the radical anion salts of (-)-NDI- $\Delta$  were successfully grown in the solutions of the alkali, alkylammonium, and phosphonium electrolytes. The X-ray analyses for the crystals grown in the PC solutions indicated the cubic space group of  $I4_132$ , which is same as that for the  $K_4$  carbon. The X-ray structural analysis of the Rb salt grown in PC revealed the  $K_4$  structure of the radical anions of (-)-NDI- $\Delta$ . This  $K_4$  structure was a chiral structure, which was formed only by the unique twisted  $\pi$ - $\pi$  interactions in all the three directions. Further, the crystal analysis showed the large cavity with a void fraction of 73%.

The chemical components of the Rb salt were analyzed by the elemental analysis and IR, EDX, and ICP measurements. These results suggested the decomposition reaction of PC into an anion species such as propane-1,2-diolate during the electrocrystallization, and the chemical formula was estimated as  $\text{Rb}_{1.4}[(-)\text{-NDI-}\Delta] \cdot 16.8[\text{Rb}_2(\text{propane-1,2-}$

diolate)]·3.1PC. This type of decomposition reaction might assist the formation of the  $K_4$  structure and owe to a structural disorder within the cavity.

The band calculation of the obtained  $K_4$  structure predicted a metallic ground state, the Dirac cones, and the doubly degenerated flat bands. The appearance of the doubly degenerated flat bands reflected the triangle shape of (-)-NDI- $\Delta$  and suggested a ferromagnetic metallic state with a partial occupation.

The temperature dependence of the conductivity for the Rb salt showed an insulating property. The EPR and magnetic susceptibility measurements showed a Curie-like behavior and the Curie-Weiss fitting of the paramagnetic susceptibility indicated an antiferromagnetic interaction of  $-10$  K and the molar Curie constant of  $0.41 \text{ emu K mol}^{-1}$ . This Curie constant roughly agreed with that of the  $S = 1/2$  species and was consistent with the formula derived from the X-ray analysis. These electronic and magnetic measurements indicated the localized-electron nature of this system.

The obtained  $K_4$  crystal is the first example formed by organic radicals. Thus, the crystal is a promising platform for investigating the band structure predicted for the  $K_4$  carbon.

## 2.8 Experimental Section

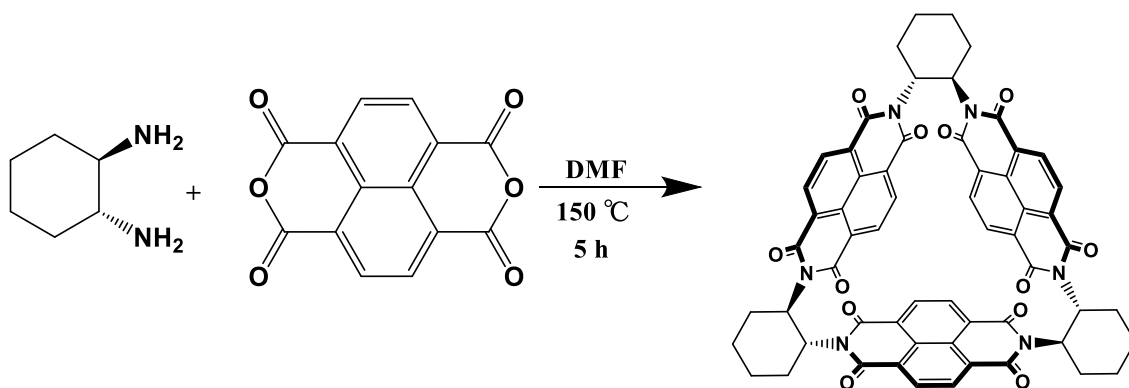
Unless otherwise noted, all chemicals were used without further purification. TOA·Br, Bu<sub>4</sub>N·ClO<sub>4</sub>, Et<sub>4</sub>N·ClO<sub>4</sub>, Me<sub>4</sub>N·ClO<sub>4</sub>, Bu<sub>4</sub>P·Br, PPh<sub>4</sub>·I, Pr<sub>4</sub>N·I, propylene carbonate (PC), 1,2-butylene carbonate, and ethylene carbonate were purchased from Tokyo Chemical Industry Co., Ltd. Na·ClO<sub>4</sub>, HClO<sub>4</sub>, Rb·Cl, Cs·Cl pyridine, iodomethane, Li·ClO<sub>4</sub>, K·ClO<sub>4</sub>, NH<sub>4</sub>·PF<sub>6</sub>, NH<sub>4</sub>·ClO<sub>4</sub>, K<sub>2</sub>(COO)<sub>2</sub>·H<sub>2</sub>O, Na<sub>2</sub>·(COO)<sub>2</sub>,

diglyme,  $\gamma$ -butyrolactone, propylene glycol, CH<sub>3</sub>CN, 1,4-dioxane, 1,2-dimethoxy ethane, and sulfolane were purchased from Waco Pure Chemical Industries, Ltd. Bu<sub>4</sub>P•PF<sub>6</sub> was purchased from Wako Chemical Ltd. Pr<sub>4</sub>P•Br was purchased from Sigma-Aldrich Co. LLC. PC, 1,2-butylene carbonate, ethylene carbonate, diglyme,  $\gamma$ -butyrolactone, propylene glycol, CH<sub>3</sub>CN, 1,4-dioxane, 1,2-dimethoxy ethane, and sulfolane were dried with molecular sieves 4A 1/16 (Waco Pure Chemical Industries, Ltd.) before use. CH<sub>3</sub>CN was dried with molecular sieves 3A 1/16 (Waco Pure Chemical Industries, Ltd.) before use. (-)-NDI- $\Delta$ <sup>138</sup> and MePy•PF<sub>6</sub> (MePy = 1-methylpyridinium)<sup>168</sup> were prepared by the literature methods. Rb•ClO<sub>4</sub> and Cs•ClO<sub>4</sub> were prepared by the reaction between water solutions of Rb•Cl or Cs•Cl, and HClO<sub>4</sub>, and the obtained colorless powders were washed by water. For inductively coupled plasma (ICP) measurements, rubidium ICP-MS standard (100  $\mu$ g mL<sup>-1</sup>) was purchased from AccuStandard, Inc., and gallium standard solution (Ga 1000), HNO<sub>3</sub> (Cat. No. 28163-3B) and H<sub>2</sub>SO<sub>4</sub> (Cat. No. 37390-3B) were purchased from Kanto Chemical Co., Inc. Ultra-pure water for ICP measurements was prepared by a Mill-Q® Academic A10 (Merck Millipore).

### 2.8.1 Synthesis of (-)-NDI- $\Delta$ and Its Radical Anion Salts

(-)-NDI- $\Delta$  was synthesized according to the literature method (Scheme 2.3).<sup>138</sup> A solution of (1*R*,2*R*)-cyclohexane-1,2-diamine (3.94 g, 0.0148 mol) in anhydrous DMF (10 mL) was heated at 150 °C and was quickly added to a solution of 1,4,5,8-naphthalenetetracarboxylic dianhydride (1.74g, 0.0152 mol) in anhydrous DMF (200 mL) with vigorous stirring at 150 °C under N<sub>2</sub> atmosphere. The resulting dark solution was stirred at 150 °C for 5h and the solution was evaporated in vacuo. The dark red residue

was dissolved in  $\text{CH}_2\text{Cl}_2$  and purified by flash column chromatography over silica gel ( $\text{CH}_2\text{Cl}_2/\text{acetone}$ , 0–10 % acetone). The separated solution was precipitated with MeOH and the resulting slightly yellow solid was collected by filtration. The residue was dried under vacuum (300 mg, 5.84%).  $^1\text{H}$  NMR (400 MHz,  $\text{CDCl}_3$ ):  $\delta$  = 8.50 (d,  $J$  = 9.2 Hz, 6H), 8.48 (d,  $J$  = 9.2 Hz, 6H), 6.29–6.17 (m, 6H), 2.58–2.40 (m, 6H), 2.06–1.88 (m, 12H), 1.76–1.62 (m, 6H). MS(FAB): calcd for  $[M+\text{H}]^+$   $m/z$  = 1039, found 1039.



**Scheme 2.3.** Synthesis of (-)-NDI- $\Delta$ .

The synthesis and crystallization of (-)-NDI- $\Delta$  radical anion salts were carried out by galvanostatic electrocrystallization in 0.1 M or saturated electrolyte solutions, containing saturated (-)-NDI- $\Delta$  in the cathode side. H-shaped glass cells equipped with a glass filter and two Pt electrodes, were purged by  $\text{N}_2$  gas, and were used for the electrocrystallizations. The black block crystals of the radical anion salts of (-)-NDI- $\Delta$  were obtained under a constant current of of 3–30  $\mu\text{A}$  within several days. The crystals used for elemental analysis, and EPR, magnetic susceptibility, SEM-EDX, ICP, and conductivity measurements, were washed several times with PC in an  $\text{N}_2$  atmosphere, and were dried under vacuum.

IR spectra were measured on a Perkin Elmer Spectrum One FT-IR Spectrometer in ATR mode. Elemental analysis was performed with a Yanaco MT-6. EDX spectra were obtained on a Hitachi S-4300 field emission SEM equipped with a Horiba EMAX 6853-H EDS system. ICP elemental analysis was performed by a Varian Vista-Pro-AX, ICP-OES, using the single crystals of  $\text{Rb}_{1.4}[(-)\text{-NDI-}\Delta]$ . The solutions of the radical anion salts were prepared by dissolving 0.35 mg of the radical anion salts in  $\text{H}_2\text{SO}_4$  and diluted to 10 mL with water. Calibrations were carried out using 0,  $1.0 \times 10^{-6}$ ,  $5.0 \times 10^{-6}$ ,  $1.0 \times 10^{-5}$ , and  $5.0 \times 10^{-5}$  M Rb cation solutions, prepared by diluting a rubidium ICP-MS standard ( $100 \mu\text{g mL}^{-1}$ ) with 3.7 %  $\text{HNO}_3$ . Gallium standard solutions were added to the Rb sample solutions as an internal standard. Emissions from Rb (780.026 nm) and Ga (294.363 nm) were monitored.

### 2.8.2 X-ray Structural Analysis

The X-ray diffraction data were collected on a Rigaku AFC-10 instrument equipped with a Saturn 70 CCD detector by using graphite-monochromated Mo  $K\alpha$  radiation ( $\lambda = 0.71075 \text{ \AA}$ ) under a cold nitrogen stream. The frame data were integrated and corrected for absorption with the Rigaku/MSO Crystal Clear package.<sup>169</sup> The structure was solved by direct method (SHELXS97<sup>170</sup>) and standard difference map techniques, and was refined with full-matrix least-square procedures on  $F^2$ . All calculations were performed using the crystallographic software package, Crystal Structure,<sup>171</sup> except for refinement, which was performed using SHELXL2013.<sup>170</sup> Anisotropic refinement was applied to all non-hydrogen atoms. All hydrogen atoms were placed at calculated positions and refined using a riding model. The electron densities in

the 3D cavity were flattened, using the SQUEEZE subroutine of PLATON,<sup>157</sup> and only the 3D network structure of the (-)-NDI- $\Delta$  anions and the Rb ions coordinated from the oxygen atoms of (-)-NDI- $\Delta$ , were refined. The void space estimation for the cavity of the Rb salt of (-)-NDI- $\Delta$  was performed, using the CALC VOID subroutine of PLATON.<sup>157</sup>

Although the structure was analyzed by reducing the symmetry ( $I2_13$ ,  $I4_122$ ,  $I4_1$ ,  $R32$ ,  $R3$ ,  $I2_12_12_1$ ,  $F222$ ,  $C2$ ) with the consideration of possible merohedral twin, the structural refinement was not improved. It was hard to locate and resolve the disordered cations and the solvent molecules in the large cavity, which occupied more than 70 volume% of the crystal structure. This is responsible for the high reliability factor.

In the present data taken at 123 K, no diffraction spot was observed at high-angle regions ( $< 0.95$  Å), because a high background, caused by the diffuse scattering from disordered cations and solvent molecules, masked the high-angle spots (Figure 2.14). Nevertheless, the present data quality is sufficient enough to conclude the  $K_4$  structure of (-)-NDI- $\Delta$ .

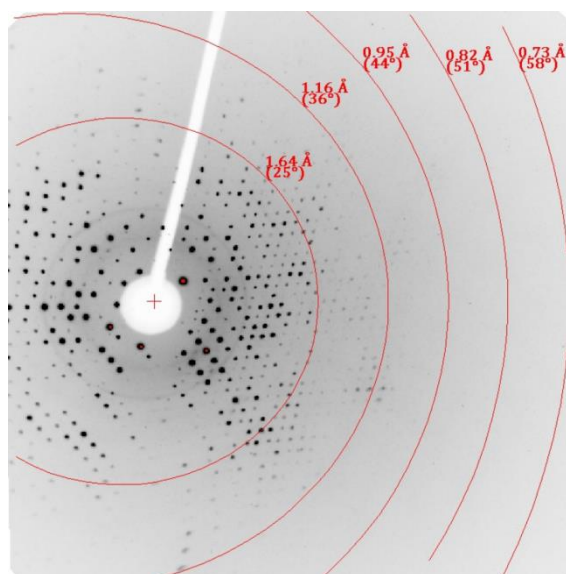


**Figure 2.14.** X-ray diffraction image of  $\text{Rb}_{1.4}[(-)\text{-NDI-}\Delta]$ .

### 2.8.3 Magnetic and Electronic Measurements

EPR measurements were carried out on a JEOL JES-FA 200 ESR Spectrometer. The crystals of  $\text{Rb}_{1.4}[(-)\text{-NDI-}\Delta]$  used for EPR measurements, were sealed in a quartz cell under vacuum after being washed with PC and dried under vacuum. Magnetic susceptibility measurements were carried out using polycrystalline samples on a Quantum Design MPMS-XL magnetometer. A plastic straw was used as the sample folder. Measurements were performed under 0.5 T in the temperature range of 2–300 K. The temperature dependence of the paramagnetic susceptibility  $\chi_p$  of the radical anion salts was calculated, using a diamagnetic susceptibility which was experimentally obtained by assuming that  $\chi_p$  follows the Curie-Weiss law at high temperatures. Conductivity measurements were carried out by a two-probe method using a Quantum Design PPMS and an Advantest R6245 2 Channel Voltage Current Source/Monitor.

### 2.8.4 DFT and Band-Structure Calculations

The intramolecular ( $t_0$ ) and intermolecular ( $t_1$ ) transfer integrals (Figure 2.8) were estimated, as follows. The single point energy calculations for a neutral  $(-)\text{-NDI-}\Delta$  and a neutral dimer of dicyclohexane-NDI units (NDI dimer) were carried out using the B3LYP methods with 6-31G\* basis set. The geometry of the  $(-)\text{-NDI-}\Delta$  and NDI dimer for the calculations were taken from the crystal structure of  $\text{Rb}_{1.4}[(-)\text{-NDI-}\Delta]$ . These calculations were performed with the Gaussian03 package.<sup>172</sup> The energy difference ( $\Delta E$ ) between the LUMO and LUMO+1 for NDI- $\Delta$  correspond to  $3t_0$  and the  $\Delta E$  between the LUMO and LUMO+1 for NDI dimer corresponds  $2t_1$  (Table 2.6). The band structure calculation was carried out by the tight-binding approximation taking into account only two kinds of neighboring interactions ( $t_0$  and  $t_1$ ) and setting the charge of  $(-)\text{-NDI-}\Delta$  as  $-1.4$ .

## Chapter 3 Spin-Frustrations in the Hyperkagome Lattices in the $K_4$ Crystals of (-)-NDI- $\Delta$

### 3.1 Introduction

As described in Section 1.4, many candidates of quantum spin liquids thus far possess 2D triangular and kagome lattices,<sup>98–100,103–115</sup> and magnetic anisotropy,<sup>102,123,124</sup> interlayer interactions<sup>108,119,120</sup> and structural deformations<sup>121</sup> in them strongly affect their ground states. These effects tend to stabilize long-range magnetic ordering instead of spin liquid states. 3D inorganic frustrated magnets with isotropic structures have also been investigated,<sup>101,116,117</sup> and many of them exhibit spin-glass ground states at low temperatures.<sup>173,174</sup> Thus, it is reasonable to expect quantum spin liquid states in 3D frustrated magnets with  $S = 1/2$  Heisenberg spins.

In Chapter 2, the  $K_4$  structure formed by the packing of radical anions of (-)-NDI- $\Delta$ , was revealed, and the valence of (-)-NDI- $\Delta$  was suggested to be  $-1.4$  from the occupancy factor of the Rb cations. Despite a metallic ground state predicted by the band calculation, the conductivity measurements showed an insulating property. It is also notable that the valence of (-)-NDI- $\Delta$  in the Rb salt was ambiguous due to the occupational disorder of the Rb cations. Among the crystals that were mentioned in Chapter 2, the TBA salt grown in the diglyme solution has no occupational disorder of the counter cations. As a result, it is suitable to investigate the detailed magnetic and thermal properties of the  $K_4$  structures with this salt.

In Chapter 3, the author firstly describes the  $K_4$  structure of the TBA salt, and the X-ray analysis clearly indicates a chemical formula of  $(\text{TBA})_{1.5}[(-)\text{-NDI-}\Delta]$ . Then, the valence of  $(-)\text{-NDI-}\Delta$ , the band structure, and the conductivity in  $(\text{TBA})_{1.5}[(-)\text{-NDI-}\Delta]$  reveal that the spin lattice corresponds to the hyperkagome lattice, which exhibits 3D spin frustration. The energy scale of spin frustration is also examined. The magnetic and heat-capacity measurements indicate an unusual nature of a gapless spin liquid state. At last, some characteristic parameters of the spin liquid state of this TBA salt are compared with other organic gapless spin liquids.

## 3.2 X-ray Analysis and Characterization of TBA Salt

### 3.2.1 X-ray Analysis of TBA Salt

As described in Section 2.2, the crystals of the TBA salt were grown in the diglyme solutions of  $\text{Bu}_4\text{N}\cdot\text{ClO}_4$ . The obtained TBA salt showed a structural disorder (large anisotropic displacement parameters) of TBA cations and the structural analysis was achieved with some constraints on the bond lengths and displacement parameters in the TBA cations. Table 3.1 shows the crystallographic data for the TBA salt. The structure of the TBA salt belongs to the cubic space group of  $P4_332$ . Although this is different from that for the Rb salt ( $I4_132$ ), the packing motif of the  $(-)\text{-NDI-}\Delta$  radical anions is the same as in the Rb salt. Therefore, the TBA salt is also a  $K_4$  crystal and the left-handed ( $M$ )-helices are formed in the same manner. It is noteworthy that three NDI units within one molecule in the TBA salt is crystallographically equivalent due to a 3-fold axis as in the Rb salt.

The nearest-neighbor intermolecular arrangement of the (-)-NDI- $\Delta$  radical anions and the location of the TBA cations in the TBA salt, are shown in Figure 3.1. A twisted  $\pi$ - $\pi$  interaction with the twisted angle of  $70.5^\circ$  is observed. This arrangement is totally the same as in the Rb salt. One TBA ion is shared by two neighboring (-)-NDI- $\Delta$  molecules, which makes the ratio between (-)-NDI- $\Delta$  and TBA 1:1.5. Therefore, the chemical formula is (TBA)<sub>1.5</sub>[(-)-NDI- $\Delta$ ], and the valence of (-)-NDI- $\Delta$  is  $-1.5$ .

**Table 3.1.** Crystallographic data for (TBA)<sub>1.5</sub>[(-)-NDI- $\Delta$ ].

Formula	C <sub>84</sub> H <sub>96</sub> N <sub>7.5</sub> O <sub>12</sub>
Formula weight / g mol <sup>-1</sup>	1402.73
Temperature / K	123
Crystal dimensions / mm <sup>3</sup>	0.29 × 0.18 × 0.17
System	Cubic
Space group	<i>P</i> 4 <sub>3</sub> 32 (#212)
<i>a</i> / Å	30.0813(6)
<i>V</i> / Å <sup>3</sup>	27220.1(9)
<i>Z</i>	8
$\rho_{\text{calcd}}$ / g cm <sup>-3</sup>	0.685
$\mu$ (CuK $\alpha$ ) / cm <sup>-1</sup>	3.698
$\lambda$ / Å	1.54187
$2\theta_{\text{max}}$ / °	136.5
Reflections collected	507664
Unique reflections ( <i>R</i> <sub>int</sub> )	8325 (0.0467)
Number of parameters	312
Number of restraints	63
Final <i>R</i> <sub>1</sub> [ <i>I</i> > 2 $\sigma$ ( <i>I</i> )]	0.0712
<i>wR</i> <sub>2</sub> (all data)	0.2328
Goodness of fit	0.935
Flack parameter (SHLEXL)	0.33(5)
Hooft <i>y</i> (PLATON)	0.04(4)
Residual electron density / Å <sup>-3</sup>	0.15 e <sup>-</sup>
Void fraction	54.7%

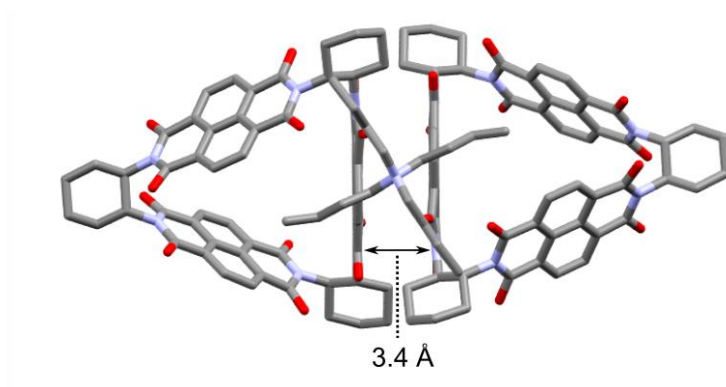
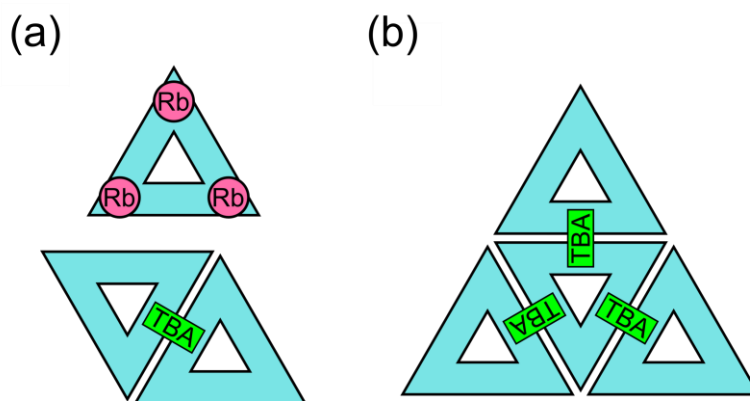


**Figure 3.1.** Nearest-neighbor intermolecular arrangement of the (-)-NDI- $\Delta$  radical anions and the location of the TBA ion in  $(\text{TBA})_{1.5}[(-)\text{-NDI-}\Delta]$ .

### 3.2.2 Comparison between Rb and TBA Salts

Here, the difference between the Rb and TBA salts is discussed. Scheme 3.1 schematically shows a comparison between the locations of the Rb and TBA ions with respect to the (-)-NDI- $\Delta$  radical anions. The  $\text{Rb}^+$  ions are disordered on the top and bottom sides of the triangle in a crystallographically equivalent manner. On the other hand, the top and bottom environment of the triangular molecule in the TBA salt is not equivalent. One  $\text{TBA}^+$  ion is shared by two neighboring (-)-NDI- $\Delta$  molecules on only one side of each (-)-NDI- $\Delta$  in the TBA salt. This difference results in different types of lattices. The IR measurements suggest that the valences of (-)-NDI- $\Delta$  are nearly identical in the Rb and TBA salts (Figure 3.2). Since the valence of (-)-NDI- $\Delta$  in the Rb salt (-1.4) was determined by the occupancy factor of the Rb ions, this value should include a large error bar, namely  $-1.4 \pm 0.1$ . It is highly possible that the valence in the Rb salt is also close to -1.5.



**Scheme 3.1.** (a) Comparison between the location of the Rb<sup>+</sup> ions in Rb<sub>1.4</sub>[(-)-NDI-Δ] and the TBA<sup>+</sup> ions in (TBA)<sub>1.5</sub>[(-)-NDI-Δ]. (b) Expansion view of the intermolecular geometry of (TBA)<sub>1.5</sub>[(-)-NDI-Δ].

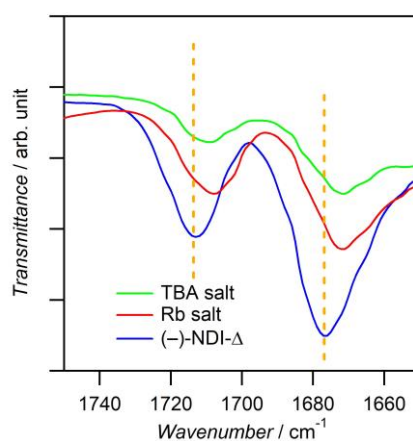


**Figure 3.2.** IR spectra for the neutral (-)-NDI-Δ and its radical anion salts. Comparison between the C=O stretching vibrations of the neutral (-)-NDI-Δ, Rb<sub>1.4</sub>[(-)-NDI-Δ], and (TBA)<sub>1.5</sub>[(-)-NDI-Δ].

### 3.2.3 Characterization of TBA Salt

Further analysis on the composition and the radical character of the (-)-NDI-Δ radical anions in the TBA salt was carried out. The results of the elemental analysis for the TBA salt are shown in Table 3.2. The elements except for C, H, and N occupy 19.67 wt%, which is much smaller than that for the Rb salt in which the abnormal amount of

Rb ions exists (See Section 2.4). Since the EDX spectrum for the TBA salt in Figure 3.3 indicates the presence of  $\text{ClO}_4^-$  ions, this residual elemental ratio is occupied by Cl and O. In the TBA salt, N sources are TBA ions and (-)-NDI- $\Delta$ . By taking these into account, it is found that the experimental data can be well explained by the chemical formula,  $(\text{TBA})_{1.5}[(-)\text{-NDI-}\Delta] \cdot 2.2[\text{TBA} \cdot \text{ClO}_4] \cdot 0.3\text{diglyme}$  with 66.19% for C, 8.25% for H, and 6.18% for N. The experimental data can be reasonably explained without assuming the decomposition of materials as in the Rb salt (See Section 2.4).

**Table 3.2.** Results of the elemental analysis of  $(\text{TBA})_{1.5}[(-)\text{-NDI-}\Delta]$ .

C	H	N	Others
66.19%	7.97%	6.18%	19.67%

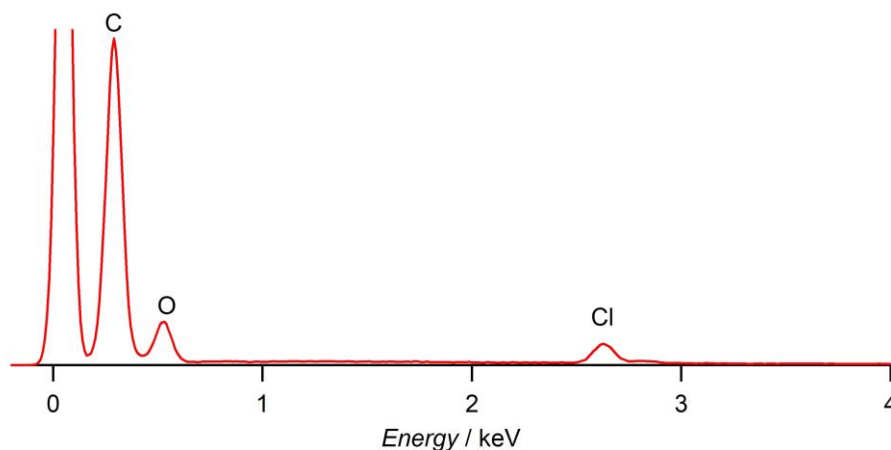


**Figure 3.3.** EDX spectrum for  $(\text{TBA})_{1.5}[(-)\text{-NDI-}\Delta]$ .

To figure out the radical character of the (-)-NDI- $\Delta$  radical anions, the IR and UV-VIS-NIR diffuse reflectance measurements were carried out for the TBA salt. The IR spectrum in Figure 3.4(a) shows a broad band around 0.5 eV for the TBA salt. The reflectance spectrum in Figure 3.4(b) shows that this broad band continues to 1.2 eV and

another broad band appears in the range of 1.5–3.0 eV. The band in the higher-energy region is similar to that in the radical anions of (–)-NDI- $\Delta$  and typical NDIs in solution.<sup>138,140,163,175,176</sup> This indicates the presence of the (–)-NDI- $\Delta$  radical anions in the TBA salt. It is noteworthy that the band in the lower-energy region does not appear in the solution spectra, and is characteristic of the solid-state. The origin of this band is further discussed in Section 3.4.

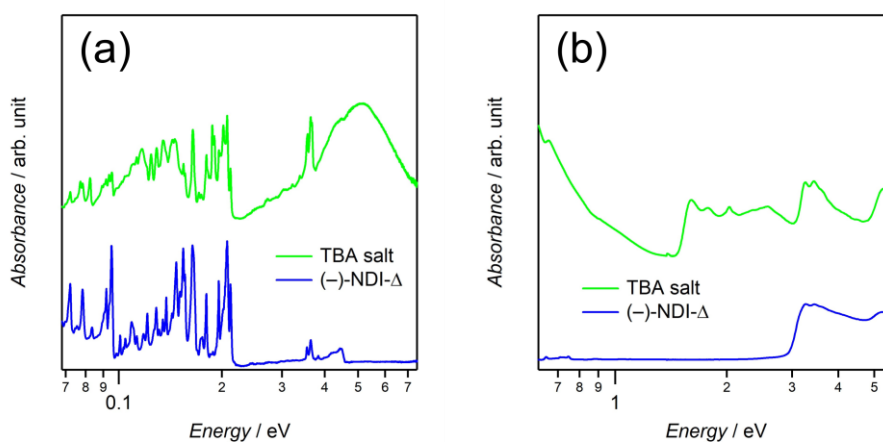


**Figure 3.4.** IR (a) and UV-VIS-NIR diffuse reflectance spectra (b) for the neutral (–)-NDI- $\Delta$  and (TBA)<sub>1.5</sub>[(–)-NDI- $\Delta$ ].

### 3.3 Band Structure and Electronic Properties of TBA Salt

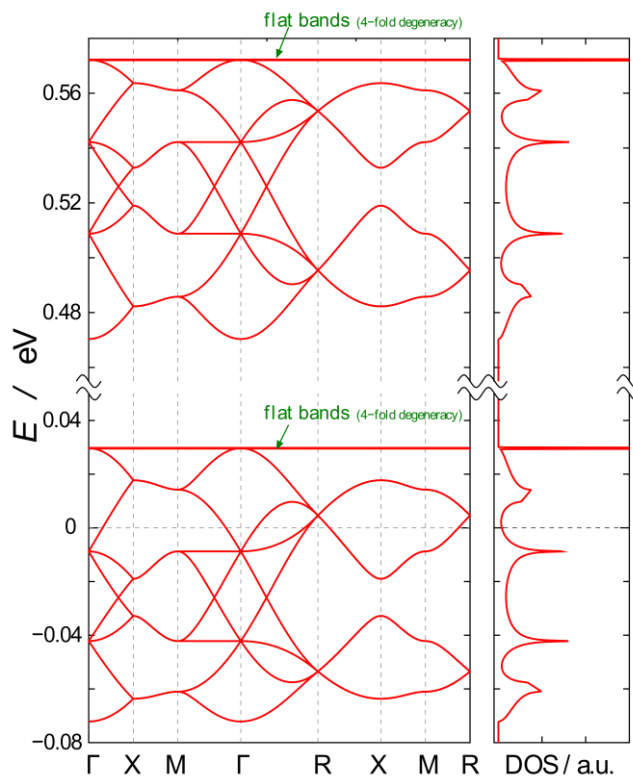
The band calculation for the TBA salt was carried out with the same procedure as described in Section 2.5. Table 3.3 shows the calculated transfer integrals,  $t_0$  and  $t_1$ . They are nearly the same as those for the Rb salt. Note that the absolute value of  $t_1$  is an order of magnitude larger than that of  $t_0$ .

Figure 3.5 shows the band structure and the density of states, which look different from those for the Rb salt (See Figure 2.9). This is caused by the difference in the space

group, namely  $P4_332$  for the TBA salt and  $I4_132$  for the Rb salt. Since the primitive cell in the TBA salt is twice as large as that in the Rb salt, the number of the bands is also doubled. The density of states, however, does not show any difference. This means that the band structure of the TBA salt is essentially equivalent to that of the Rb salt, indicating a metallic ground state, Dirac cones, and degenerate flat bands. The difference in the space group should not affect the expected electronic states.

**Table 3.3.** Calculation of transfer integrals in  $(\text{TBA})_{1.5}[(-)\text{-NDI-}\Delta]$ .

	$E_{\text{LUMO}} / \text{eV}$	$E_{\text{LUMO}+1} / \text{eV}$	$\Delta E / \text{eV}$	$t / \text{eV}$
NDI- $\Delta$	-3.430	-3.329	0.102	-0.034 ( $t_0$ )
NDI dimer	-3.712	-3.170	0.543	-0.271 ( $t_1$ )



**Figure 3.5.** Band structure and density of states (DOS) for the  $K_4$  structure of the radical anions of  $(-)\text{-NDI-}\Delta$ . The Fermi energy for  $(\text{TBA})_{1.5}[(-)\text{-NDI-}\Delta]$  is set to 0 eV.

The temperature dependence of the conductivity for the TBA salt was measured on a single crystal with a two-probe method (Figure 3.6). The theoretical fit to the experimental data with Eq. (2.1) gives an activation energy of 0.2 eV. The conductivity and the activation energy in the TBA salt are in the same order of magnitude as those of the Rb salt (see Section 2.6), indicating that the valence of the (-)-NDI- $\Delta$  radical anions is nearly identical in these salts.

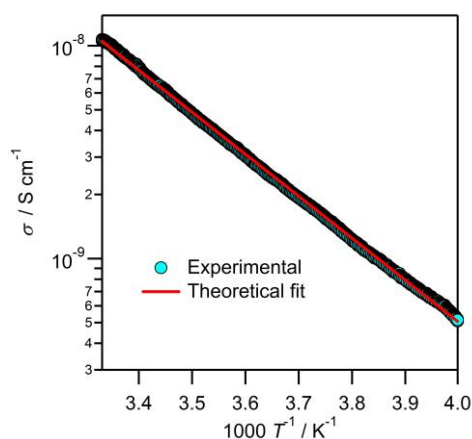


**Figure 3.6.** Temperature dependence of the conductivity for  $(\text{TBA})_{1.5}[(-)\text{-NDI-}\Delta]$  in the temperature range of 250–300 K.

### 3.4 Spin Lattice of TBA Salt: $K_4$ Crystal to Hyperkagome Lattice

In this section, the spin lattice of the  $K_4$  structure of  $(\text{TBA})_{1.5}[(-)\text{-NDI-}\Delta]$  is discussed, considering the valence of (-)-NDI- $\Delta$  and the transfer integrals  $t_0$  and  $t_1$ . As described in Section 3.2, the valence of one (-)-NDI- $\Delta$  is  $-1.5$ , so that a half electron exists on the NDI unit, which is one-third of (-)-NDI- $\Delta$ . Since the intermolecular interaction  $t_1$  is much larger than the intramolecular one  $t_0$ , it is reasonable to conclude

that one unpaired electron is shared within an intermolecular NDI dimer unit as shown in Figure 3.7. The positions of the TBA ions also support this interpretation.

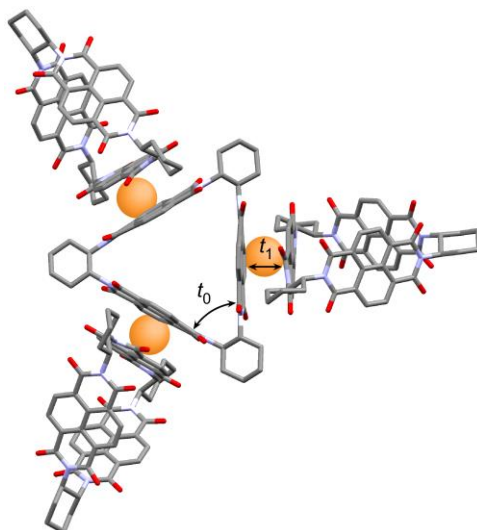


**Figure 3.7.** Nearest-neighbor intermolecular arrangements of the (-)-NDI- $\Delta$  radical anions in  $(\text{TBA})_{1.5}[(-)\text{-NDI-}\Delta]$ . The orange circles indicate the locations of the  $S = 1/2$  unpaired electrons.

Furthermore, the conductivity measurement indicated an insulating property of  $(\text{TBA})_{1.5}[(-)\text{-NDI-}\Delta]$ . This electron localization would be caused by the weak intramolecular interaction  $t_0$ , which corresponds to the interaction between the unpaired electrons. These features closely resemble those of the dimer Mott systems that were found in the organic radical salts of BEDT-TTF and  $\text{Pd}(\text{dmit})_2$ .<sup>10,11,58–61</sup> In these materials, one dmit (BEDT-TTF) dimer unit bears one unpaired electron, and these dimer units form a triangular lattice with spin frustration (see Section 1.2). Based on the dimer Mott model, the  $K_4$  structure of (-)-NDI- $\Delta$  can be transformed into a lattice of unpaired electrons, which turns out to be a hyperkagome lattice, consisting of corner-sharing triangles as shown in Figure 3.8. This is the first example of an organic hyperkagome lattice with

isotropic  $S = 1/2$  spins. As described in Section 1.4, a hyperkagome lattice is a 3D frustrated lattice, and an inorganic material  $\text{Na}_4\text{Ir}_3\text{O}_8$  has been intensively investigated as a quantum spin liquid with a hyperkagome lattice of corner sharing  $\text{Ir}^{4+}$  ions with  $S = 1/2$  spins.<sup>101</sup> Strong spin-orbit coupling of the Ir ions, however, affects the nature of the spin liquid state.<sup>102</sup> Thus, the present organic hyperkagome lattice consisting of light elements such as C, H, N, and O could be a more suitable system of quantum spin liquids.

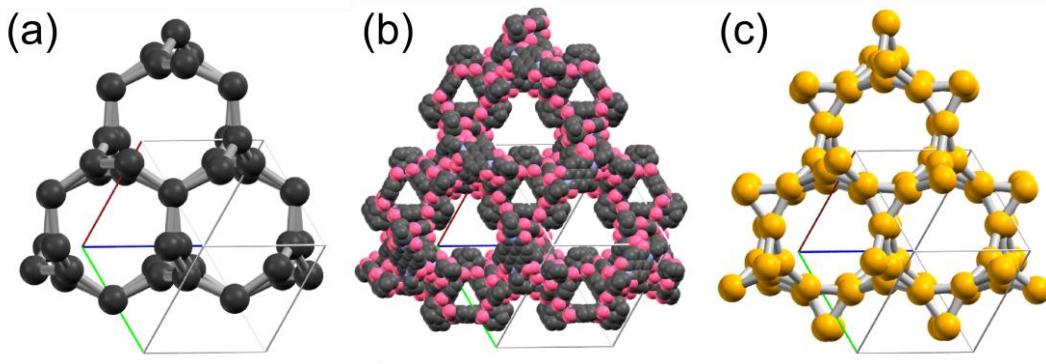


**Figure 3.8.** Comparison of the structures of the  $K_4$  carbon (a), the  $K_4$  structure of (-)-NDI- $\Delta$  (b), and the hyperkagome lattice, formed by the unpaired electrons on the Mott dimers (c).

Figure 3.9(a) shows the important parameters which govern the low-temperature ground state in this frustrated magnet. In this figure,  $t_{\text{eff}}$  and  $U_{\text{eff}}$  are the effective transfer integral and the effective on-site Coulomb repulsion between the unpaired electrons on the NDI-dimer units, respectively.  $t_{\text{eff}}$  is a half of  $t_0$ , and  $U_{\text{eff}}$  is determined by  $t_1$ , the on-site ( $U$ ) and intersite ( $V_1$ ) Coulomb repulsions between the NDI units. In the two-site Hubbard model, the antiferromagnetic interaction  $J$  can be expressed as

$$J = -\frac{U_{\text{eff}} - \sqrt{U_{\text{eff}}^2 + 16t_{\text{eff}}^2}}{2}. \quad (3.1)$$

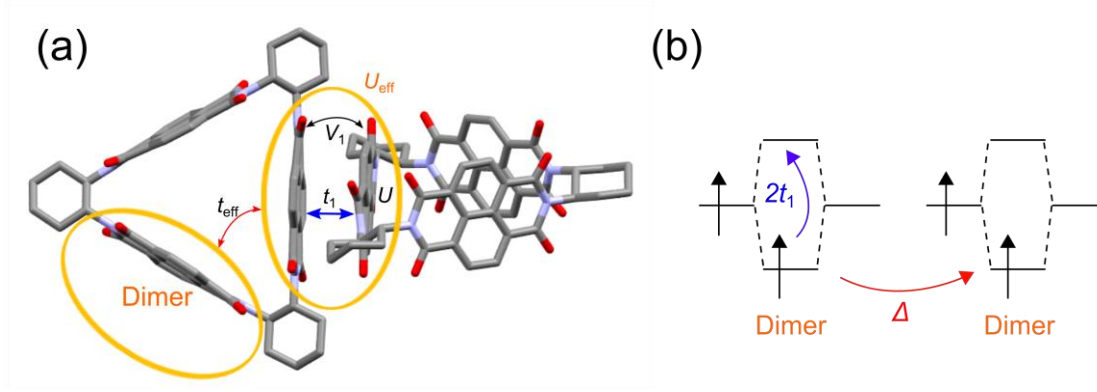


**Figure 3.9.** (a) Definition of the transfer integrals and the Coulomb repulsions in  $(\text{TBA})_{1.5}[(-)\text{-NDI-}\Delta]$ . (b) Two possible electronic transitions, characteristic of the solid state in the  $K_4$  crystal.

In the limit of  $U_{\text{eff}} \gg t_{\text{eff}}$ ,

$$J \approx -\frac{4t_{\text{eff}}^2}{U_{\text{eff}}}. \quad (3.2)$$

$U_{\text{eff}}$  is described as

$$U_{\text{eff}} = \frac{(U + V_1)}{2} - \sqrt{\left(\frac{U - V_1}{2}\right)^2 + 4t_1^2} + 2t_1. \quad (3.3)$$

In the limit of  $U \gg t_1$  and  $U \gg V_1$ ,

$$U_{\text{eff}} \approx 2t_1 + V_1 - \frac{4t_1^2}{U}. \quad (3.4)$$

The value of  $U_{\text{eff}}$  is calculated as  $U_{\text{eff}} = 2t_1 = 0.54$  eV if we ignore  $V_1$  and  $-4t_1^2/U$ . This value is in the range of 0.3–1.0 eV, which is common for the Mott-dimer systems of BEDT-TTF.<sup>177–181</sup>  $J$  can be calculated as  $-2$  meV ( $\sim -20$  K) by using this  $U_{\text{eff}}$  value. The antiferromagnetic interaction  $J$  should cause a spin frustration in the present hyperkagome lattice. The obtained  $U_{\text{eff}}$  value can be rationalized by considering a charge gap  $\Delta$  expressed as

$$\Delta = U_{\text{eff}} - W, \quad (3.5)$$

where  $W$  is the band width in the TBA salt. The experimental value of the charge gap in the TBA salt is calculated from the activation energy for the conductivity  $E_a$ , namely as  $\Delta = 2E_a = 0.4$  eV. This  $\Delta$  is nearly the same as that obtained as  $\Delta = U_{\text{eff}} - W = 0.54 - 0.10 = 0.44$  eV. This agreement justifies the present estimations for  $U_{\text{eff}}$  and  $J$ . The above discussion is also related to the broad absorption band appeared around 0.5 eV in the UV-VIR-NIR spectra (See Figure 3.4), which is characteristic of the solid state. Though the absorption spectra are taken for the polycrystalline samples, the absorptions should be deconvoluted to two types of electron transition in one crystallographically independent NDI unit of the  $K_4$  structure, as shown in Figure 3.9(b). One is the electron transfer transition between the dimers, mediated by  $\Delta = U_{\text{eff}} - W = 2t_1 + V_1 - W$ , and the other is the excitation in the dimer, mediated by  $2t_1$ . The experimental value of  $\Delta$  ( $\sim 0.4$  eV) and the theoretical value of  $2t_1$  ( $\sim 0.5$  eV) are consistent with the absorption energy of 0.5 eV. Furthermore, the predicted magnetic interaction  $J/k_B \sim -20$  K is also consistent with the Weiss temperature, which is described in the next section.

### 3.5 Magnetic Properties of TBA Salt

In Section 3.4, a hyperkagome lattice formed by unpaired electrons in the  $K_4$  structure was revealed. This hyperkagome lattice is a 3D frustrated lattice and the resulting geometrical spin frustration should affect the magnetic and thermal properties. Recently, solid-state NMR measurement is regarded as one of the effective methods to investigate quantum spin liquid states as it can probe the local magnetic environment of the selected atomic nucleus with high sensitivity and provide us a strong evidence of

magnetic ordering. In this section, the effect of spin frustration on the magnetic properties of the TBA salt is discussed, based on the results of EPR, magnetic susceptibility, and  $^{14}\text{N}$  NMR measurements.

The EPR spectra for the TBA salt were measured in the temperature range of 5–300 K. The results are shown in Figure 3.10. Figure 3.11 shows the temperature dependence of the EPR spin susceptibility, peak-to-peak line width, and  $g$ -factor. The EPR signal exhibits a single Lorentzian absorption at  $g = 2.0036$  and no temperature-dependent variation is observed. These results mean that the spins on the (-)-NDI- $\Delta$  radical anions could be regarded as isotropic Heisenberg spins. The EPR spin susceptibility shows Curie-like behavior in the whole temperature range and the line width increases with decreasing temperature.

The temperature dependence of the magnetic susceptibility  $\chi_p$  was also examined. After diamagnetic correction, the obtained paramagnetic susceptibilities  $\chi_p$  are shown in Figure 3.12.  $\chi_p$  increases with decreasing temperature. The Curie Weiss fitting of the high-temperature region gives  $\theta = -15$  K and  $C = 2.1 \times 10^{-4}$  emu K  $g^{-1}$ . This negative Weiss temperature indicates an antiferromagnetic interaction. This is consistent with the predicted magnetic interaction  $J/k_B \sim -20$  K caused by the interdimer interaction  $t_{\text{eff}}$  (See Section 3.4). The antiferromagnetic interaction is expected to induce a spin frustration in the hyperkagome lattice. The value of a molar Curie constant is estimated to be 0.46 emu K  $\text{mol}^{-1}$  by using the chemical formula  $(\text{TBA})_{1.5}[(-)\text{-NDI-}\Delta] \cdot 2.2[\text{TBA} \cdot \text{ClO}_4] \cdot 0.3\text{diglyme}$ , which was explained in Section 3.2.3. This molar Curie constant is higher than that of the  $S = 1/2$  species, but is smaller than the expectation ( $0.375 \times 1.5 = 0.563$  emu K  $\text{mol}^{-1}$ ) from the above formula. This could be related to a relatively large concentration of the lattice defects in this crystal described below.

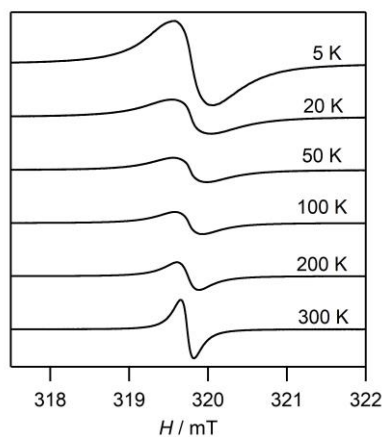


**Figure 3.10.** Temperature dependence of the EPR signals for  $(\text{TBA})_{1.5}[(-)\text{-NDI-}\Delta]$  at representative temperatures from 5 to 300 K.

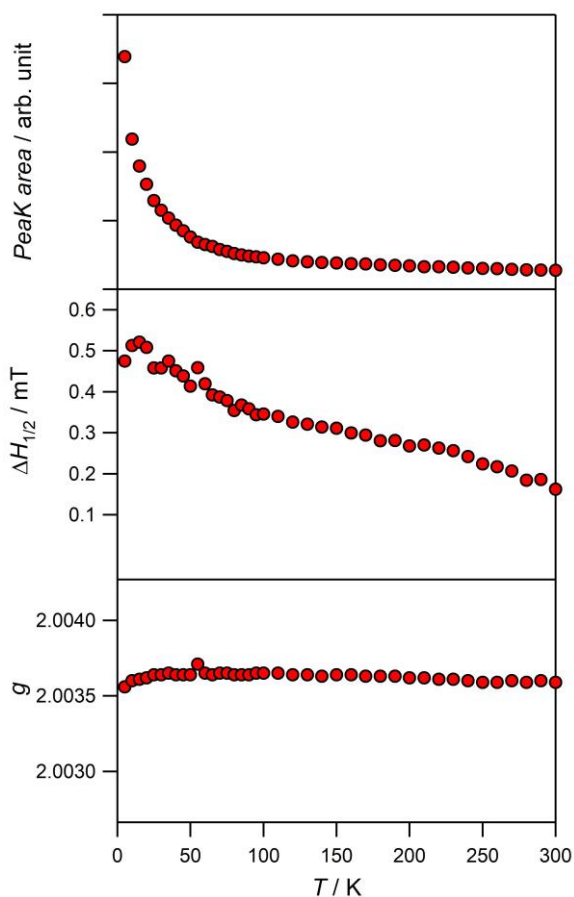


**Figure 3.11.** Temperature dependences of the EPR spin susceptibility, peak-to-peak line width, and  $g$ -factor of the EPR signals for  $(\text{TBA})_{1.5}[(-)\text{-NDI-}\Delta]$ .

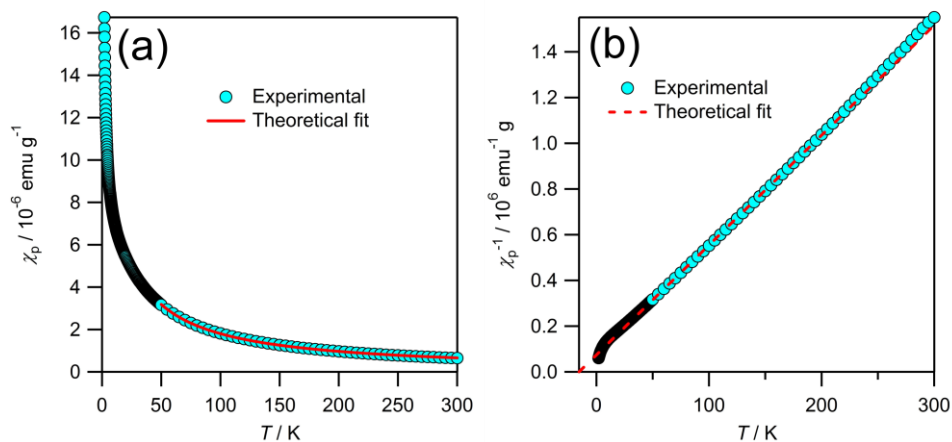


**Figure 3.12.** Magnetic data for  $(\text{TBA})_{1.5}[(-)\text{-NDI-}\Delta]$  in the temperature range of 2–300 K: the temperature dependence of  $\chi_p$  (a) and the reciprocal of  $\chi_p$  (b).

To elucidate the effect of spin frustration on the magnetic behavior of this material, the low-temperature magnetic susceptibility of the TBA salt was measured from 70 mK to 6 K by using a homemade SQUID susceptometer mounted on a dilution refrigerator. The low-temperature data were smoothly connected with the high-temperature data taken on a SQUID susceptometer. Figure 3.13(a) shows the temperature dependence of the paramagnetic susceptibility in the temperature range of 0.07–300 K.  $\chi_p$  increases with decreasing temperature and exhibits a small anomaly around 20 K, which is probably caused by the interdimer interaction  $J$  mediated by  $t_{\text{eff}}$ . After that,  $\chi_p$  continues to increase down to the lowest temperature. The data indicate no long-range magnetic ordering despite the 3D antiferromagnetic interactions with  $\theta = -15$  K. It should be noted that the AC magnetic susceptibility measured from 0.05 to 2 K shows no anomaly as expected for spin glass, and there is no clear difference between the DC and AC magnetic susceptibility. Below 1 K, the temperature dependence of the paramagnetic susceptibility can be explained by

$$\chi_p = \chi_0 + \chi_{\text{def}} = \chi_0 + \frac{C_{\text{def}}}{T - \theta_{\text{def}}}, \quad (3.6)$$

where  $\chi_0$ ,  $\chi_{\text{def}}$ ,  $C_{\text{def}}$ , and  $\theta_{\text{def}}$  are the constant paramagnetic susceptibility, paramagnetic susceptibility caused by the lattice defects, Curie constant and Weiss temperature for the lattice defects, respectively. The theoretical best fit is obtained with the following parameters:  $\chi_0 = (8.5 \pm 0.5) \times 10^{-6} \text{ emu g}^{-1}$ ,  $C_{\text{def}} = (2.0 \pm 0.05) \times 10^{-5} \text{ emu K g}^{-1}$  and  $\theta_{\text{def}} = -3 \pm 2 \text{ mK}$ . The value of  $C_{\text{def}}$  corresponds to 9.6% of the total spins. The purple broken line in Fig. 3.13(a) shows the temperature dependence of  $\chi_{\text{def}}$ . The red curve in Figure 3.13(a) is the intrinsic paramagnetic susceptibility  $\chi_{\text{int}}$ , which is calculated by

$$\chi_{\text{int}} = \chi_p - \chi_{\text{def}}. \quad (3.7)$$

The results of this analysis clearly suggest the presence of  $\chi_{\text{int}}$  even at 0.5 K despite the 3D magnetic interactions with  $\theta = -15 \text{ K}$ .

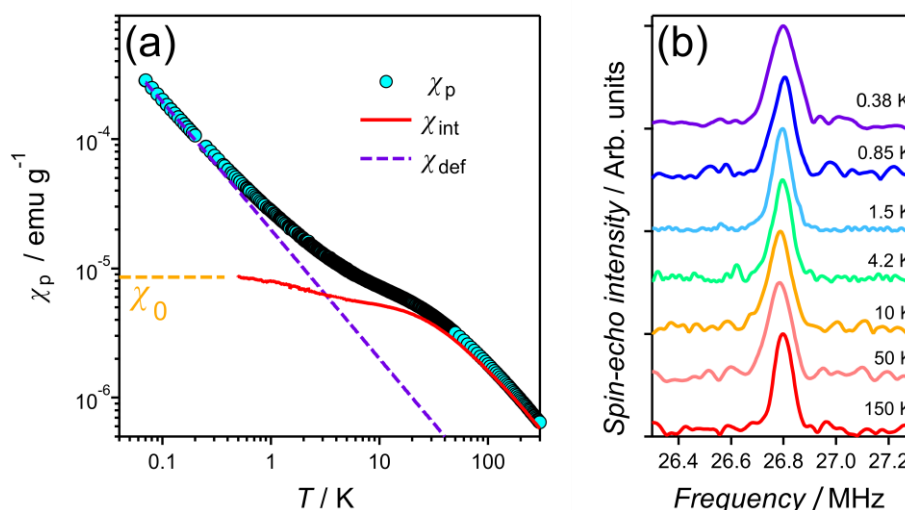


**Figure 3.13.** (a) Temperature dependence of the paramagnetic susceptibility  $\chi_p$  in the temperature range 0.07–300 K for  $(\text{TBA})_{1.5}[(-)\text{-NDI-}\Delta]$ . The purple broken line and the red curve indicate those of  $\chi_{\text{def}}$  and  $\chi_{\text{int}}$ , respectively. See the text. (b) Temperature dependence of the  $^{14}\text{N}$  NMR signals for  $(\text{TBA})_{1.5}[(-)\text{-NDI-}\Delta]$  at representative temperatures.

The variable-temperature  $^{14}\text{N}$  NMR measurements of  $(\text{TBA})_{1.5}[(-)\text{-NDI-}\Delta]$  were performed from 0.38 K to 150 K by measuring spin-echo spectra at a constant magnetic field of 8.71 T. Figure 3.13(b) shows the signals at representative temperatures. The NMR signal shapes are governed by nuclear quadrupole interactions for the nuclear spin  $^{14}I = 1$ . It is clearly demonstrated that, though the NMR signal shapes become slightly broader with a decrease in temperature, there is no drastic change such as that seen in long-range magnetic ordering transition. Although this type of small linewidth broadening is recognized in the spin liquid states of  $\kappa\text{-(BEDT-TTF)}_2\text{Cu}_2\text{CN}_3$  and  $\text{EtMe}_3\text{Sb}[\text{Pd}(\text{dmit})_2]_2$ ,<sup>99,110–112</sup> the origin is still not clear. These magnetic data strongly suggest the presence of spin frustration on the hyperkagome lattice and the formation of a spin liquid state, instead of long-range magnetic ordering.

### 3.6 Thermal Properties of TBA Salt

The magnetic data in Section 3.5 strongly suggested the formation of a quantum spin liquid state. Theoretical studies on quantum spin liquid states have predicted degenerated ground states caused by quantum fluctuations, and the degenerated gapless states have been recently revealed by thermal measurements at low temperatures for various inorganic and organic quantum-spin-liquid systems.<sup>32,95,125</sup> Especially, heat-capacity measurement has been intensively used as a valuable tool to reveal the magnetic ground states of these materials. In this section, the nature of the quantum spin liquid state is discussed, based on the results of the heat capacity measurements down to 68 mK.

The temperature dependence of the heat capacity  $c_p$  for  $(\text{TBA})_{1.5}[(-)\text{-NDI-}\Delta]$  was measured in the temperature range of 2–50 K and 0.068–4.5 K on a Quantum Design

Physical Property Measurement System (PPMS) and a homemade calorimeter mounted on a dilution refrigerator, respectively. Figure 3.14(a) shows the temperature dependence of  $c_p$  in the whole temperature range. The values of  $c_p$  gradually decrease with decreasing temperature, and slightly increase below 0.1 K. This is consistent with the absence of long-range magnetic ordering. To estimate the lattice contribution, a  $c_p/T$  vs  $T^2$  is plotted for  $T < 5$  K as shown in Figure 3.14(b). With a decrease in temperature, the values of  $c_p/T$  show a linear decrease, followed by a sudden increase below ca. 0.1 K. Such increase at extremely low temperatures has often been observed in organic spin systems, and has been attributed to a high-temperature tail of a Schottky peak, formed by nuclear spins, weak magnetic interactions between paramagnetic defects, or internal molecular rotations.<sup>182</sup> Above 1 K, a linear relation between  $c_p/T$  and  $T^2$  is observed. This type of linear relation can be fitted by

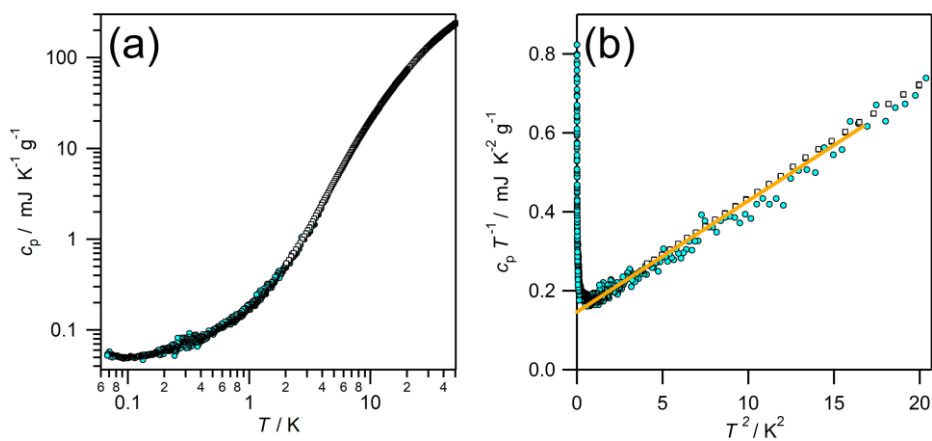


**Figure 3.14.** (a) Temperature dependence of the heat capacity  $c_p$  for  $(\text{TBA})_{1.5}[(-)\text{-NDI-}\Delta]$ . (b)  $c_p/T$  vs  $T^2$  plots in the low-temperature range. The orange line shows a linear relation between  $c_p/T$  and  $T^2$  with a lattice capacity coefficient of  $\beta = 0.028 \text{ mJ K}^{-4} \text{ g}^{-1}$ .

$$c_p = \gamma T + \beta T^3, \quad (3.8)$$

where  $\gamma$  and  $\beta$  are the linear heat capacity coefficient and lattice heat capacity coefficient, respectively. The fitting line shows a lattice heat capacity coefficient of  $\beta = 0.028 \text{ mJ K}^{-4} \text{ g}^{-1}$  and a nonzero  $\gamma$  value. Generally, a nonzero  $\gamma$  value indicates an electronic specific heat of a metallic state. However, since the present material is an insulator, this linear term means the presence of a large heat capacity for the spin liquid state.

A detailed analysis on the heat capacity data was carried out to estimate the temperature dependence of  $c_p$  for the spin liquid state. Figure 3.15 shows the plots of  $c_p/T$  vs  $\log T$  below 5 K, in which the increases in  $c_p/T$  at the high- and low-temperature sides are the lattice contribution and the high-temperature tail of the Schottky anomaly, respectively. It is found that this temperature dependence can be well explained by

$$c_p = aT^{-2} + bT^\xi + \beta T^3, \quad (3.9)$$

where the first term is for the contribution of the Schottky tail below 0.1 K, the second term is for the spin liquid state, and the third term is for the lattice contribution above 1 K. The theoretical best fit with  $\xi = 0.62$  is obtained by optimizing the values of  $a$ ,  $b$ , and  $\xi$ . It is shown as the bold gray curve in Figure 3.15. The blue, bold red, and black curves indicate the contributions of the first, second, and third terms, respectively. Any reasonable fitting cannot be obtained without adding the second term. The contributions of the first and third terms are negligibly small in the temperature range between 0.2 and 0.6 K. The agreement between the experimental plots and the theoretical curve in this temperature range strongly justifies that  $c_p$  is proportional to  $T^{0.62}$  in the spin liquid state.

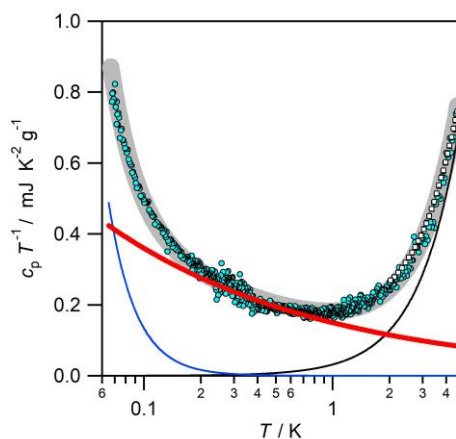


**Figure 3.15.**  $c_p/T$  vs  $T$  plots in the temperature range 0.068–5 K. The open squares and the blue circles indicate the data, taken on a PPMS and a homemade calorimeter, respectively. The blue, bold red, and black curves indicate the contributions of the first, second, and third terms in the equation  $c_p = aT^{-2} + bT^\xi + \beta T^3$ , respectively.

It is reported that  $c_p$  of 3D inorganic hyperkagome systems, such as  $\text{Na}_4\text{Ir}_3\text{O}_8$ ,<sup>101</sup> possesses a  $T^2$  term. However, a simple comparison between the inorganic and present organic systems does not make sense, as strong magnetic interactions and magnetic anisotropies caused by spin-orbit interactions are involved in the inorganic systems. In the context of the heavy fermion problem, the low-temperature heat capacities near the quantum critical points in the 2D and 3D systems are theoretically predicted to exhibit  $T^{2/3}$  and  $T \ln(1/T)$  dependences, respectively.<sup>183</sup> However, any reasonable fitting with a  $T \ln(1/T)$  term, instead of the  $T^\xi$  term could not be achieved in the TBA salt. It is not certain whether the fairly good agreement between the observed  $T^{0.62}$  behavior and the  $T^{2/3}$  dependence for the 2D system is meaningful or not. Anyhow, the theoretical understanding of the present hyperkagome system of organic Heisenberg spins will be a future challenge.

### 3.7 Comparison with Organic Gapless Quantum Spin Liquids

The magnetic and heat-capacity measurements revealed the spin liquid nature of the present system with an unusual temperature dependence of the heat capacity:  $c_p \propto T^{0.62}$  for the quantum spin liquid state. In this section, several parameters, which are often used for spin liquid systems, are described to compare with those of other spin liquid materials.

An empirical measure of spin frustration proposed by Ramirez<sup>184</sup> is written as

$$f = \frac{|\theta|}{T_c}, \quad (3.10)$$

where  $T_c$  is any cooperative-ordering transition temperature. The frustration parameter can be calculated as  $f > 200$ , which indicates strong spin frustration in this system. The Wilson ratio  $R$ , which is originally defined in the context of Fermi liquids, is also used as an indicator of quantum spin liquid states.<sup>95</sup> The Wilson ratio is defined as

$$R = \frac{4\pi^2 k_B^2 \chi_0}{3(g\mu_B)^2 \gamma}, \quad (3.11)$$

where  $\mu_B$  is the Bohr magneton. Many quantum-spin-liquid materials exhibit the Wilson ratios which are in the range of 1–9, and a strong spin-orbit coupling is considered to increase  $\chi_0$  and  $R$  values. The values of molar  $\chi_0$  and  $\gamma$  for  $(\text{TBA})_{1.5}[(-)\text{-NDI-}\Delta]$  were estimated in order to compare with those of other organic gapless spin liquids. The  $\chi_0$  value ( $= 8.5 \times 10^{-6} \text{ emu g}^{-1}$ ), which is the extrapolation of the intrinsic paramagnetic susceptibility to the absolute zero temperature in Fig. 3.13(a), roughly corresponds to  $7.9 \times 10^{-3} \text{ emu mol}^{-1}$  for the unit molar mass of the unpaired electrons ( $\text{C}_{56}\text{H}_{64}\text{N}_5\text{O}_8$  with molecular mass = 935). This reflects the existence of gapless magnetic excitations in the

spin liquid state. Although the heat capacity for the spin liquid state in the TBA salt was proportional to  $T^{0.62}$ , the value of  $c_p/T$  at  $T = 1$  K ( $= 0.15$  mJ K $^{-2}$  g $^{-1}$ ) can be used as a parameter corresponding to  $\gamma$ . This value is approximately converted to  $1.4 \times 10^2$  mJ K $^{-2}$  mol $^{-1}$ . The Wilson ratio for (TBA) $_{1.5}$ [(-)-NDI- $\Delta$ ] is calculated to be 4.2. Table 3.4 lists organic gapless quantum spin liquids. In this table,  $c_{\text{QSL}}$  describes the heat capacity for quantum spin liquid states. The values of  $\chi_0$  and  $\gamma$  for (TBA) $_{1.5}$ [(-)-NDI- $\Delta$ ] are an order of magnitude larger than those for the other organic triangular systems. The Wilson ratio is in the same order of magnitude as those of the other spin liquids with weak spin-orbit coupling.

**Table 3.4.** Comparison between the organic gapless quantum spin liquids.

Entry	Material	Lattice	$c_{\text{QSL}}$	$\gamma$ / mJ K $^{-2}$ mol $^{-1}$	$\chi_0$ / emu mol $^{-1}$	$R$
1	$\kappa$ -(BEDT-TTF) $_2$ Cu $_2$ (CN) $_3$	Triangular	$\gamma T$ ( $-\gamma_{2/3} T^{2/3}$ )	12	$2.9 \times 10^{-4}$	1.76
2	EtMe $_3$ Sb[Pd(dmit) $_2$ ] $_2$	Triangular	$\gamma T$	19.9	$4.4 \times 10^{-4}$	1.61
3	$\kappa$ -H $_3$ (Cat-EDT-TTF) $_2$	Triangular	$\gamma T^n + a T^2$ ( $n = 2/3 - 1$ )	58.8	$1.2 \times 10^{-3}$	1.49
4	$\kappa$ -(BEDT-TTF) $_2$ Ag $_2$ (CN) $_3$	Triangular	$\gamma T^n$ ( $n = 2/3 - 1$ )	10	-	-
5	This work	Hyperkagome	$b T^{0.62}$	$1.4 \times 10^2$	$7.9 \times 10^{-3}$	4.2

Ref. [99, 185, 186] for entry 1. Ref. [110, 187] for entry 2. Ref [63, 188] for entry 3. Ref. [189] for entry 4.

### 3.8 Conclusion

The crystal structure of the TBA salt grown in diglyme was successfully solved, and the  $K_4$  structure with the cubic space group of  $P4_332$  was revealed.  $\text{TBA}^+$  ions were shared by the intermolecular dimers, and the valence of  $(-)\text{-NDI-}\Delta$  in  $(\text{TBA})_{1.5}[(-)\text{-NDI-}\Delta]$  was determined as  $-1.5$ .

The band calculation of the TBA salt predicted a metallic ground state, Dirac cones, and degenerated flat bands. Despite the different space group of the TBA salt, the band structure was essentially same as that for the Rb salt. The temperature dependence of the conductivity for the TBA salt showed insulating properties.

The determined valence along with the insulating ground state strongly indicated that the present system should be regarded as a Mott-dimer insulator and that the spin structure, formed by  $S = 1/2$  unpaired electrons, should correspond to a hyperkagome lattice with spin frustration.

The temperature dependence of the EPR spectra indicated isotropic Heisenberg spins in this system. The temperature dependence of the paramagnetic susceptibility indicated no long-range magnetic ordering down to 70 mK in spite of the 3D antiferromagnetic interactions with  $\theta = -15$  K. The Curie defects contribution was observed at low temperatures and the large intrinsic paramagnetic susceptibility was obtained even at 0.5 K after subtracting the Curie defects contribution. The  $^{14}\text{N}$  NMR measurements indicated no magnetic ordering down to 0.38 K. The temperature dependence of the heat capacity showed no indication of magnetic ordering down to 68 mK and a  $T^{0.62}$  dependence of the heat capacity for the spin liquid state. These magnetic

and thermal properties strongly suggested the presence of spin frustration on the hyperkagome lattice and the formation of a spin liquid state.

The present system is the first example of an organic hyperkagome lattice with isotropic  $S = 1/2$  spins. So far, theoretical and experimental works on frustrated magnets with a hyperkagome lattice with  $S = 1/2$  spins are very limited; to the best of the author's knowledge, an inorganic material,  $\text{Na}_4\text{Ir}_3\text{O}_8$ , is the only quantum spin liquid in which the strong spin-orbit coupling of the Ir ions affects the nature of the spin liquid state. Since the gapless nature characterized by  $T^{0.62}$  dependence of the heat capacity for the spin liquid state has not been predicted for 3D frustrated magnets, the theoretical understanding of the present hyperkagome system will be a future challenge.

## **3.9 Experimental Section**

### **3.9.1 Preparation of (–)-NDI- $\Delta$ Radical Anion Salts**

The synthesis and crystallization of (–)-NDI- $\Delta$  radical anion salts are described in Section 2.8.1. The crystals of the TBA salt used for magnetic, electronic, and thermal measurements were washed several times with diglyme in an  $\text{N}_2$  atmosphere, and were dried under vacuum. Elemental analysis, and IR and EDX measurements for the TBA salt were carried out with the same procedures as described in Section 2.8.1. Diffuse reflectance UV-VIS-NIR spectrum was examined on a JASCO V-570 UV/VIS/NIR spectrophotometer equipped with an ISN-470 integrating sphere apparatus by using the diluted samples in  $\text{BaSO}_4$  powder.

### 3.9.2 X-ray Structural Analysis

The X-ray diffraction data were collected on a Rigaku R-Axis RAPID diffractometer equipped with a MicroMax007HF microfocus generator, a VariMax DW optic, and a RAPID IP detector by using Cu-K $\alpha$  radiation ( $\lambda = 1.54187 \text{ \AA}$ ) under a cold nitrogen stream at 123 K. No diffraction spot was observed at high-angle regions ( $< 0.99 \text{ \AA}$ ) as shown in Figure 3.16. The frame data were integrated and corrected for absorption with the Rigaku RAPID AUTO package.<sup>190</sup> The structure was solved by direct method (SHELXS97<sup>170</sup>) and standard difference map techniques, and was refined with full-matrix least-square procedures on  $F^2$ . All calculations were performed using the crystallographic software package, Crystal Structure,<sup>191</sup> except for refinement, which was performed using SHELXL Version 2016/4.<sup>170</sup> Anisotropic refinement was applied to all non-hydrogen atoms. The tetrabutylammonium cation was refined with restraints on the bond length (DFIX commands) and on the anisotropic displacement parameters (SIMU and DELU commands). All hydrogen atoms were placed at calculated positions and refined using a riding model. The electron densities in the 3D cavity were flattened, using the SQUEEZE subroutine of PLATON,<sup>157</sup> and only the 3D network structure of the (-)-NDI- $\Delta$  anions and the TBA ions near (-)-NDI- $\Delta$ , were refined. The absolute structure parameter Hooft  $y$ <sup>192</sup> corresponding to Flack parameter was calculated using BIJVOET pair analysis of PLATON.<sup>157</sup> The space group was determined to be  $P4_332$  (not  $P4_132$ ) since the Hooft  $y = 0.04(4)$  for this structure indicates the absolute structure is correct.

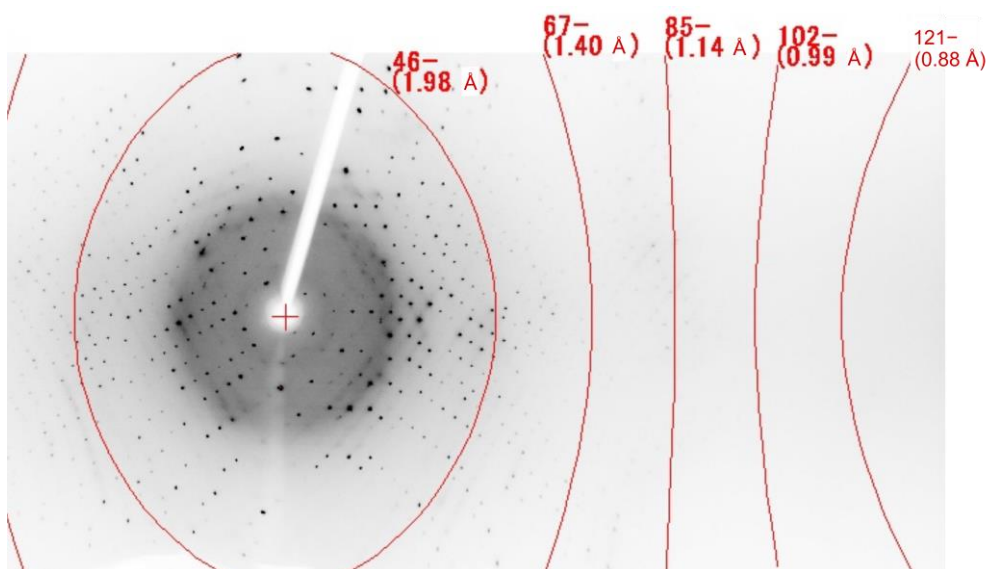


**Figure 3.16.** X-ray diffraction image of TBA<sub>1.5</sub>[(-)-NDI-Δ].

### 3.9.3 Magnetic and Electronic Measurements

EPR and conductivity measurements were carried out with the same procedures as described in Section 2.8.3. Magnetic susceptibility measurements were carried out using polycrystalline samples on a Quantum Design Magnetic Property Measurement System MPMS-XL magnetometer (2–300 K) and on a home-made SQUID susceptometer mounted on a dilution refrigerator (0.07–6 K). On the Quantum Design MPMS-XL magnetometer, a plastic straw was used as the sample folder, and the measurement was performed under 0.5 T in the temperature range of 2–300 K. The home-made susceptometer is designed as the same as that by Karaki et.al.<sup>193</sup> Between 0.05 and 2 K, AC susceptibility by the SQUID was measured at the frequency 175 Hz and the amplitude 6 mG under the residual magnetic field below a few mG, where the earth magnetic field about 300 mG is shielded by a  $\mu$ -metal. Between 0.07 and 6 K, DC susceptibility was measured under 9 G. The temperature dependence of the paramagnetic susceptibility  $\chi_p$  of the radical anion salts was calculated, using a diamagnetic susceptibility which was

experimentally obtained by assuming that  $\chi_p$  follows the Curie-Weiss law at high temperatures.  $^{14}\text{N}$ -NMR measurements were carried out for polycrystalline samples in the range between 0.38 K and 150 K, using a commercial spectrometer for solid-state NMR. The spin-echo spectrum was measured at a constant magnetic field of 8.713 T.

### 3.9.4 Heat-Capacity Measurements

Heat-capacity measurements were carried out in the temperature range of 2–50 K and 0.068–4.5 K on a PPMS and a home-made calorimeter mounted on a dilution refrigerator, respectively. Addenda heat capacity (background) was measured with Apiezon N high vacuum grease and crystals were mounted on the platform. The data (Figures 3.14 and 3.15) obtained on a PPMS were calibrated with copper as a standard because it was claimed that the measurements on this instrument might contain a relatively-large error at low temperatures.<sup>194,195</sup> The data were divided by the ratio of the electronic coefficient between an experimental value  $\gamma_{\text{exp}}$  and a reference value  $\gamma_{\text{ref}}$ <sup>196</sup> ( $\gamma_{\text{exp}}/\gamma_{\text{ref}} = 0.756/0.695 = 1.09$ ). Thermometer of the home-made calorimeter<sup>197</sup> was calibrated to 50 mK by the paramagnetic susceptibility of CMN ( $\text{Ce}_2\text{Mg}_3(\text{NO}_3)_{12}\cdot 24\text{H}_2\text{O}$ ) and a Ge thermometer calibrated above 0.3 K. The heat capacity was measured with the quasi-adiabatic heat pulse method. The absolute value of the heat capacity was confirmed by measuring the heat capacity of silver.

### 3.9.5 DFT and Band-Structure Calculations

The DFT and band calculations were carried out with the same procedures as described in Section 2.8.4. The DFT calculations were performed with the Gaussian09 package.<sup>198</sup>

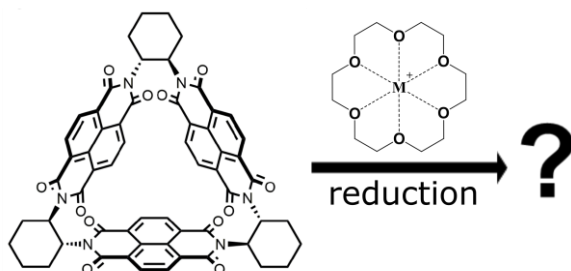
# Chapter 4 Preparation of 3D Chiral Crystals of Radical Anions of (-)-NDI- $\Delta$ : Formation of (*M*)- and (*P*)-Helices from a Chiral Molecule

## 4.1 Introduction

Chirality of supramolecular structures plays an important role in our lives as seen in the double helices of DNA<sup>199</sup> and the  $\alpha$ -helices of proteins.<sup>200</sup> These types of helical structures are responsible for their molecular recognition, catalytic reaction, self-replication, etc.<sup>201–203</sup> In addition, chirality is also important for the function of cholesteric liquid crystals, which reflect circularly polarized light in a manner dependent on the helical pitch in them.<sup>204</sup> It is well known that the supramolecular chirality is transferred from the molecular chirality in self-assembled systems.<sup>158</sup> Actually, the  $K_4$  crystals formed by the (-)-NDI- $\Delta$  radical anions exhibited the left-handed (*M*)-helices stereospecifically formed by the  $\pi$ - $\pi$  interactions between the chiral (-)-NDI- $\Delta$  molecules, as described in Chapters 2 and 3. The control of the supramolecular chirality is an interesting challenge in terms of the crystal engineering based on (-)-NDI- $\Delta$ .

Crown ethers are well-studied cyclic multidentate ligands, which have strong coordination ability to various metal ions.<sup>205,206</sup> They are utilized to increase the solubility of ions,<sup>207</sup> and also used in supramolecular chemistry as a component of rotaxanes and catenanes due to their cyclic structures.<sup>208</sup> These coordination ability and cyclic molecular structures are strongly characteristic for the crown ethers. They are also applicable to the

electrochemical crystallizations of (-)-NDI- $\Delta$  (Scheme 4.1), in which the solubility of the electrolytes is increased, and the cyclic structures along with the coordination ability affect the crystal packing by acting as “large cations” together with metal ions.



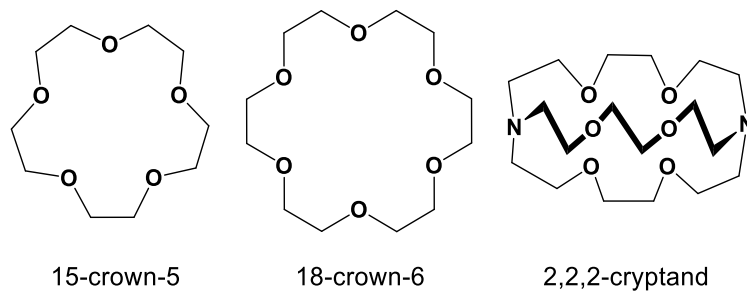
**Scheme 4.1.** Preparation of the radical anion salts of (-)-NDI- $\Delta$  with cyclic multidentate ligands.

In Chapter 4, the author focuses on novel structures formed by using alkali metal complexes of multidentate ligands as bulky cations. Novel chiral 3D structures formed by the radical anions of (-)-NDI- $\Delta$  are revealed to be induced by multidentate ligands, and the detailed analysis of the crystal components is described. The electronic, magnetic, and thermal properties of these radical anion salts are also described.

## 4.2 Preparation and X-ray Analysis of Radical Anion Salts of (-)-NDI- $\Delta$

Electrochemical crystallization of the radical anion salts of (-)-NDI- $\Delta$  was carried out in PC electrolyte solutions containing cyclic multidentate ligands. Scheme 4.2 shows the three multidentate ligands, 18-crown-6, 15-crown-5, and 2,2,2-cryptand, used in the electrocrystallization. Table 4.1 lists the crystallization conditions and the lattice parameters of the obtained crystals. The electrolytes and the ligands were mixed with the

molar ratios of 1:2 for 15-crown-5 and 18-crown-6, and of 1:1 for 2,2,2-cryptand. The radical anion salts were obtained as black block or black needle crystals.



**Scheme 4.2.** Cyclic multidentate ligands used in the electrocrystallization.

**Table 4.1.** Combinations of the electrolytes and the multidentate ligands used for the crystallization of the (-)-NDI- $\Delta$  radical anion salts, crystal habits, and lattice parameters and crystal systems of the obtained crystals.

15-crown-5			
Electrolyte	Crystal habit	Lattice parameters	Crystal system
Na•ClO <sub>4</sub>	No crystal	n/a	n/a
K•ClO <sub>4</sub>		$a = 30.5216(6) \text{ \AA}$	
Rb•ClO <sub>4</sub>	Black block	$a = 30.5208(6) \text{ \AA}$	Cubic, $I4_132$
Cs•ClO <sub>4</sub>		$a = 30.6354(8) \text{ \AA}$	
18-crown-6			
K•ClO <sub>4</sub>		$a = b = 57.4679(10) \text{ \AA},$ $c = 29.3139(5) \text{ \AA}$	
Rb•ClO <sub>4</sub>	Black block	$a = b = 57.3567(10) \text{ \AA},$ $c = 29.2250(5) \text{ \AA}$	Tetragonal, $I4_1$
Cs•ClO <sub>4</sub>	Black block	$a = 30.7813(8) \text{ \AA}$	Cubic, $I4_132$
	Black needle	n/a	n/a
2,2,2-cryptand			
K•ClO <sub>4</sub>		$a = 30.7625(6) \text{ \AA}$	
Rb•ClO <sub>4</sub>	Black block	$a = 30.8007(6) \text{ \AA}$	Cubic, $I4_132$

The crystals grown with 15-crown-5 or 2,2,2-cryptand, belong to the cubic space group of  $I4_132$  with  $a = 30.5\text{--}30.8$  Å. This space group is the same as that for the  $K_4$  structure, and the values of the lattice constant  $a$  are nearly the same as those for the  $K_4$  crystals in Section 2.3. On the other hand, the crystals grown with 18-crown-6, and  $K\cdot\text{ClO}_4$  or  $\text{Rb}\cdot\text{ClO}_4$ , belong to the tetragonal space group of  $I4_1$ .

The detailed X-ray analyses were carried out for the obtained crystals belonging to the tetragonal space group. The structural refinement was successful only for the crystal of the  $\text{Rb}@18\text{-crown-6}$  salt of  $(-)\text{-NDI-}\Delta$  highlighted in red in Table 4.1. Hereafter, the author calls it  $[\text{Rb}@18\text{-crown-6}]_x[(-)\text{-NDI-}\Delta]$ . Since the structure of this salt had a large void space, the electron densities in the cavity were flattened by using the SQUEEZE subroutine of PLATON,<sup>157</sup> and only the 3D framework of the  $(-)\text{-NDI-}\Delta$  radical anions, and the Rb ions, 18-crown-6 molecules, and PCs near the  $(-)\text{-NDI-}\Delta$  radical anions were refined. Tables 4.2 and 4.3 show the selected crystallographic parameters before and after the SQUEEZE, and the crystallographic data after the SQUEEZE, respectively. After the SQUEEZE procedure, the reliability factors were significantly improved.

**Table 4.2.** Selected crystallographic parameters before and after the SQUEEZE procedure for  $[\text{Rb}@18\text{-crown-6}]_x[(-)\text{-NDI-}\Delta]$ .

	non-SQUEEZE	SQUEEZE
$R_1 [I > 2\sigma(I)]$	0.1823	0.0472
$R$ (all data)	0.2326	0.0950
$wR_2$ (all data)	0.4454	0.1611
Goodness of fit	1.467	0.874
Flack parameter	0.059(4)	0.027(4)

**Table 4.3.** Crystallographic data for [Rb@crown]<sub>x</sub>[(-)-NDI-Δ].

Formula	C <sub>224</sub> H <sub>210</sub> N <sub>18</sub> O <sub>60</sub> Rb <sub>3.94</sub>
Formula weight / g mol <sup>-1</sup>	4448.39
Temperature / K	123
Crystal dimensions / mm <sup>3</sup>	0.26 × 0.24 × 0.16
System	Tetragonal
Space group	<i>I</i> 4 <sub>1</sub> (#80)
<i>a</i> / Å	57.3567(10)
<i>c</i> / Å	29.2250(5)
<i>V</i> / Å <sup>3</sup>	96144(3)
<i>Z</i>	8
$\rho_{\text{calcd}}$ / g cm <sup>-3</sup>	0.615
$\mu$ (CuK $\alpha$ ) / cm <sup>-1</sup>	8.274
$\lambda$ / Å	1.54187
$2\theta_{\text{max}}$ / °	136.5
Reflections collected	904631
Unique reflections ( <i>R</i> <sub>int</sub> )	87867 (0.0495)
Number of parameters	2793
Number of restraints	282
Final <i>R</i> <sub>1</sub> [ <i>I</i> > 2σ( <i>I</i> )]	0.0472
<i>wR</i> <sub>2</sub> (all data)	0.1611
Goodness of fit	0.874
Flack parameter	0.027(4)
Residual electron density / Å <sup>-3</sup>	0.26 e <sup>-</sup>

The left figure in Figure 4.1(a) shows two asymmetric units of [Rb@crown]<sub>x</sub>[(-)-NDI-Δ], in which one asymmetric unit consists of three (-)-NDI-Δ molecules, three 18-crown-6 molecules, 3.94 Rb ions, and 2PCs. In the right figure in Figure 4.1(a), the centroids of the (-)-NDI-Δ molecules and the interactions between them, are represented by the balls and sticks, respectively. The numbers in this figure represent five non-equivalent intermolecular interactions between the (-)-NDI-Δ radical anions. They have 3-way π-π interactions, and the pairs of the (-)-NDI-Δ and 18-crown-6 molecules, drawn

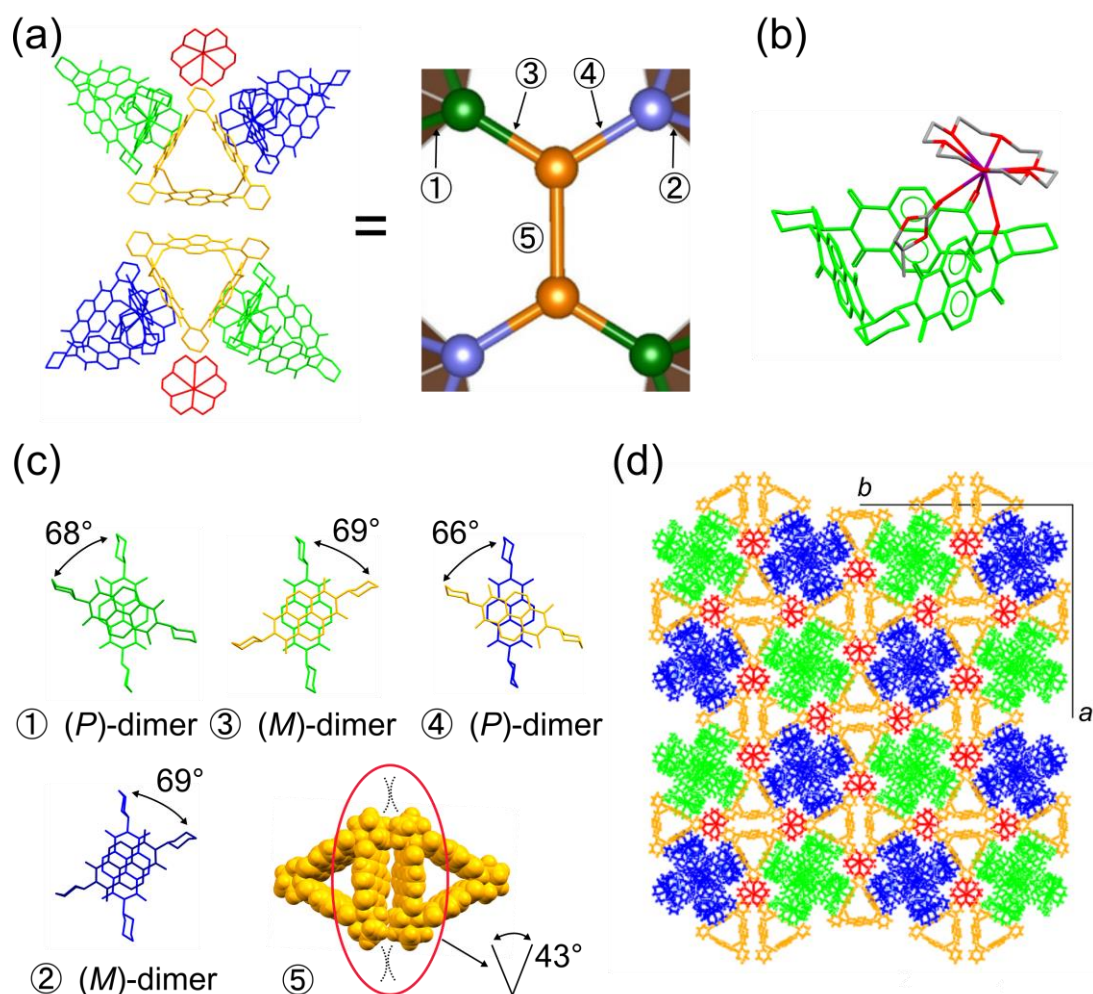


**Figure 4.1.** Crystal structure of  $[\text{Rb@crown}]_x[(-)\text{-NDI-}\Delta]$ . A part of this figure is made by VESTA.<sup>96</sup> (a) Local structure, which includes the two asymmetric units. The right figure shows a schematic view, in which the balls and sticks represent the centroids for each  $(-)\text{-NDI-}\Delta$  and the interactions between the  $(-)\text{-NDI-}\Delta$  radical anions, respectively. (b) Coordination structure in the green part. (c) Five non-equivalent intermolecular arrangements. (d) Projection of the crystal structure along the  $c$  axis.

in green and blue, include coordination bondings to the Rb ions. Figure 4.1(b) shows the coordination structure in the green part in Figure 4.1(a). The Rb ion is coordinated from the  $(S)\text{-PC}$ , 18-crown-6, and  $(-)\text{-NDI-}\Delta$ . The similar coordination geometry is observed in the blue part, in which the PC can be analyzed as a mixture of  $(S)\text{-PC}$  and  $(R)\text{-PC}$  with

the occupancy factors of 0.757(5) and 0.243(5), respectively. Figure 4.1(c) shows the five non-equivalent intermolecular arrangements. Four of the five arrangements show  $\pi$ - $\pi$  interactions characterized by two types of chiral dimers, (*M*)- and (*P*)-helical dimers. The twisted angles of 66–69° are slightly smaller than that of the  $K_4$  structure (70.5°), and the short interplanar distances of 3.2–3.3 Å between the NDI units are observed. The coexistence of the two chiral arrangements is in stark contrast to the  $K_4$  and 1D helical structures<sup>138</sup> of (–)-NDI- $\Delta$  which contain only (*M*)-helical dimers. On the other hand, the intermolecular arrangement shown in orange doesn't include  $\pi$ - $\pi$  interactions. The orange NDI units within the red circle shows a dihedral angle of 43°, which is much smaller than the cross angle of 60° in a regular triangle. This suggests that the intermolecular interaction between the orange NDI units is stronger than the intramolecular interaction in (–)-NDI- $\Delta$ . Figure 4.1(d) shows the projection of the crystal structure along the *c* axis, which includes a 3D network structure of (–)-NDI- $\Delta$ . For clarify, the schematic views of the overall structure are shown below.

Figures 4.2(a) and 4.2(b) show a comparison between the schematic views of the structures of [Rb@*crown*]<sub>x</sub>[(–)-NDI- $\Delta$ ] viewed along the *c* and *a* axes, respectively. All of the (–)-NDI- $\Delta$  molecules are connected by the  $\pi$ - $\pi$  interactions, forming a 3D network structure with a huge 3D cavity with a void fraction of 63%. In Figure 4.2(b), the left-handed (*M*)- and right-handed (*P*)-helices are formed along the *c* axis, and these helices are connected by the orange parts. The coexistence of the two types of helices formed by the  $\pi$ - $\pi$  interactions is a very interesting feature of this structure. Though a single chiral (–)-NDI- $\Delta$  is used in the crystallization, its molecular chirality is no longer transferred to the supramolecular chirality. The formation of the two types of chiral helices formed by the single chiral molecules is very rare.

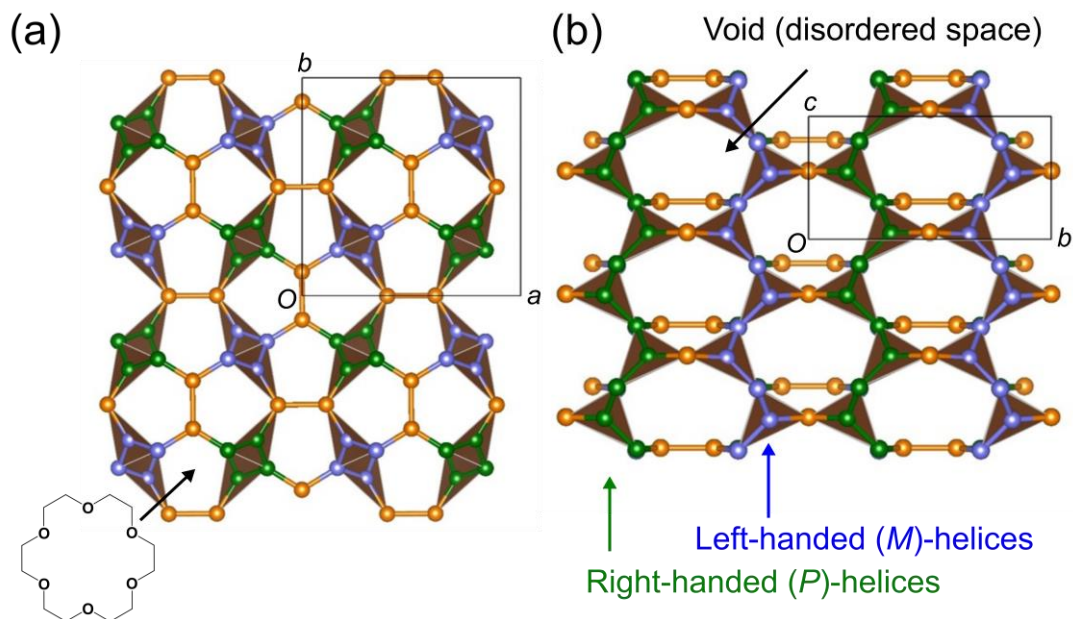


**Figure 4.2.** Comparison between the schematic views of  $[\text{Rb@crown}]_x[(-)\text{-NDI-}\Delta]$  viewed along the *c* (a) and *a* axes (b). This figure is made by VESTA.<sup>96</sup>

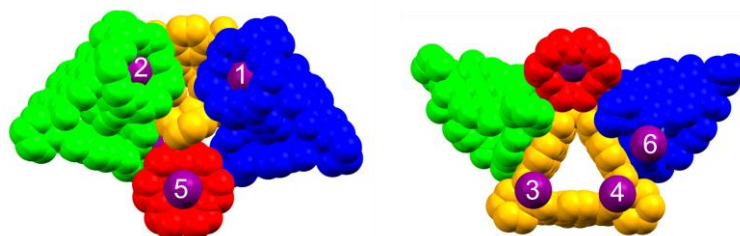


**Figure 4.3.** Positions and occupancy factors of the Rb ions in  $[\text{Rb@crown}]_x[(-)\text{-NDI-}\Delta]$ .

Next, the positions and occupancy factors of the Rb ions in  $[\text{Rb@crown}]_x[(-)\text{-NDI-}\Delta]$  are described. Figure 4.3 shows the positions of the Rb ions in this salt, where the six non-equivalent Rb ions are present. Table 4.4 lists the occupancy factors of the Rb ions. The occupancy factors of the Rb ions, Rb3-Rb6, are smaller than 1, indicating that the positions of the Rb ions are disordered and their distributions are inhomogeneous. The valence of  $(-)\text{-NDI-}\Delta$  is calculated from the occupancy factors of the Rb ions, Rb1-Rb4, and Rb6, which are coordinated from the  $(-)\text{-NDI-}\Delta$  molecules. Table 4.5 lists the valence

of the (-)-NDI- $\Delta$  radical anions. Presumably, they are mono radical anions, but due to the inhomogeneous distribution of the Rb ions, the detailed discussion on the solid-state properties is difficult.

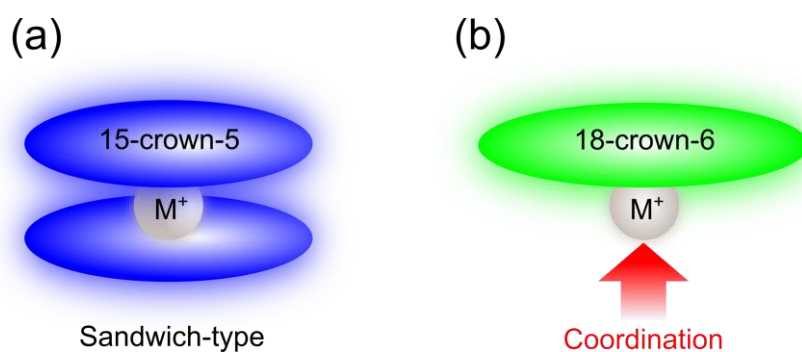
**Table 4.4.** Occupancy factors of the Rb ions in [Rb@*crown*]<sub>x</sub>[(-)-NDI- $\Delta$ ].

Rb1	Rb2	Rb3	Rb4	Rb5	Rb6
1	1	0.722(3)	0.540(3)	0.474(2)	0.203(3)

**Table 4.5.** Valence of the (-)-NDI- $\Delta$  radical anions estimated by the Rb ions around them in [Rb@*crown*]<sub>x</sub>[(-)-NDI- $\Delta$ ].

Green	Orange	Blue
-1	-1.26	-1.20

At last, the formation of the novel 3D crystal is discussed, on the basis of the crystal structure and the formation constants of alkali metal salt complexes with the multidentate ligands. Reported formation constants of the alkali metal ions with the crown ethers and the cryptand suggest the expected numbers of the multidentate ligands coordinated to the metal ions under the crystallization conditions.<sup>209–214</sup> From these knowledge, K, Rb, and Cs ions are expected to be fully encapsulated by 15-crown-5 and 2,2,2-cryptand with 1:2 sandwich-type coordination (Scheme 4.3(a)) and 1:1 cage-type coordination, respectively. On the other hand, K, Rb, and Cs ions with 18-crown-6 are expected to leave accessible coordination sites by forming 1:1 coordination as shown in Scheme 4.3(b). This expectation well agrees with the coordination structure observed in [Rb@*crown*]<sub>x</sub>[(-)-NDI- $\Delta$ ] (See Figure 4.1(b)). The coordination structure of the 18-crown-6 molecules to the Rb ions is considered as an important factor to induce the present 3D structure.



**Scheme 4.3.** Schematic structures of the sandwich-type (a) and 1:1 complexes (b) of crown ethers.

### 4.3 Characterization of Rb@18-crown-6 Salt

In Section 4.2, the X-ray analysis revealed the 3D network structure formed by the (-)-NDI- $\Delta$  radical anions, characterized by the two types of helices with different chirality. In this section, the chemical components of  $[\text{Rb@crown}]_x[(-)\text{-NDI-}\Delta]$  are discussed, on the basis of the results of elemental analysis and IR, EDX, and UV-VIS-NIR measurements.

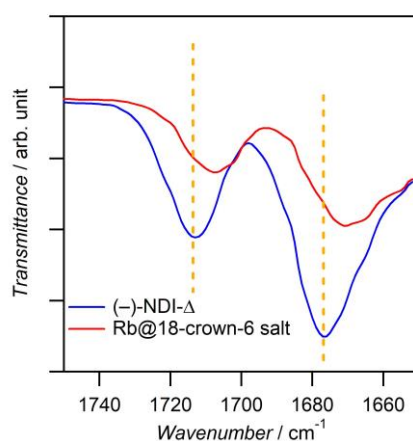


**Figure 4.4.** IR spectra for the neutral (-)-NDI- $\Delta$  and  $[\text{Rb@crown}]_x[(-)\text{-NDI-}\Delta]$ . Comparison between the C=O stretching vibrations of the neutral (-)-NDI- $\Delta$  and  $[\text{Rb@crown}]_x[(-)\text{-NDI-}\Delta]$ .

Figure 4.4 shows the IR spectra for the neutral (-)-NDI- $\Delta$  and  $[\text{Rb@crown}]_x[(-)\text{-NDI-}\Delta]$ . The frequencies of the Rb salt are lower than those of the neutral (-)-NDI- $\Delta$  as seen for the Rb and TBA salts in Chapters 2 and 3. The results of the elemental analysis for  $[\text{Rb@crown}]_x[(-)\text{-NDI-}\Delta]$  are shown in Table 4.6. The elements except for C, H, and N occupy 32.65 wt%. Figure 4.5 shows the EDX spectrum for  $[\text{Rb@crown}]_x[(-)\text{-NDI-}\Delta]$ , indicating the presence of Rb ions and the absence of  $\text{ClO}_4^-$  ions. Although the whole chemical formula of  $[\text{Rb@crown}]_x[(-)\text{-NDI-}\Delta]$  were not figured out probably due to the presence of water (See Figure 4.6(a) and the description below), it can be concluded that (-)-NDI- $\Delta$  occupies 53.15 wt% of this salt, from the N wt-ratio.

**Table 4.6.** Results of the elemental analysis of  $[\text{Rb@crown}]_x[(-)\text{-NDI-}\Delta]$ .

C	H	N	Others
57.50%	5.55%	4.30%	32.65%

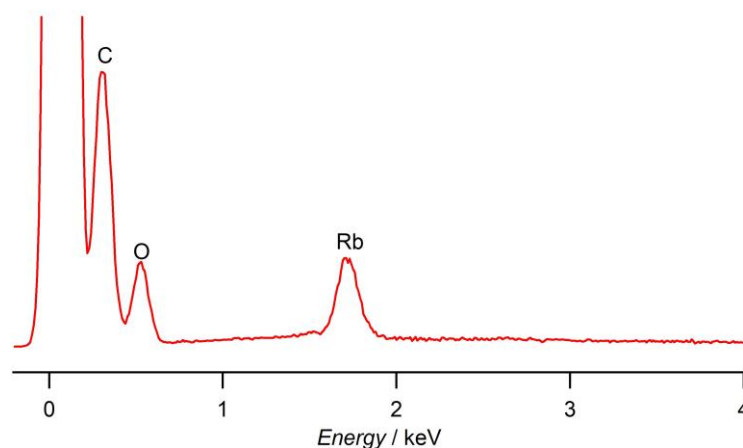


**Figure 4.5.** EDX spectrum for  $[\text{Rb@crown}]_x[(-)\text{-NDI-}\Delta]$ .

To figure out the radical character of the (-)-NDI- $\Delta$  radical anions, the IR and UV-VIS-NIR diffuse reflectance spectra were measured for  $[\text{Rb@crown}]_x[(-)\text{-NDI-}\Delta]$ .

Figure 4.6(a) shows the IR spectra for the neutral (–)-NDI- $\Delta$  and [Rb@crown]<sub>x</sub>(–)-NDI- $\Delta$ . The spectrum for [Rb@crown]<sub>x</sub>(–)-NDI- $\Delta$  indicates a broad band around 0.6 eV accompanied by a narrower band between 0.4 and 0.5 eV. The narrower band is assignable to O–H stretching vibrations broadened by hydrogen bonds, suggesting the presence of water in this salt. The diffuse reflectance spectrum for [Rb@crown]<sub>x</sub>(–)-NDI- $\Delta$  in Figure 4.6(b) shows that this broad band continues to 1.2 eV and another broad band appears in the range of 1.5–3.0 eV. The band in the higher-energy region is similar to that in the radical anions of various NDIs in solution.<sup>138,140,163,175,176</sup> This indicates the presence of the (–)-NDI- $\Delta$  radical anions in the TBA salt. The band in the lower-energy region (0.6 eV) is characteristic of the solid-state, which is similar to that in the TBA salt (0.5 eV) described in Section 3.2.3. This band could have the similar origin as discussed in Section 3.4.

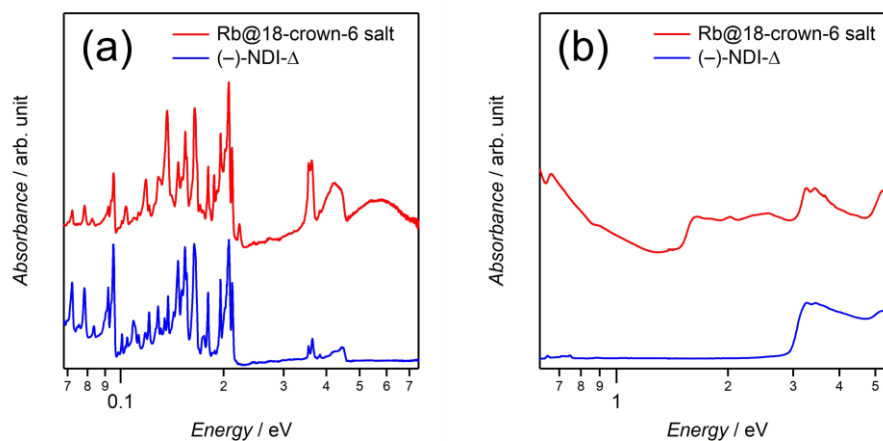


**Figure 4.6.** IR (a) and UV-VIS-NIR diffuse reflectance spectra (b) for the neutral (–)-NDI- $\Delta$  and [Rb@crown]<sub>x</sub>(–)-NDI- $\Delta$ .

## 4.4 Magnetic, Electronic, and Thermal Properties of Rb@18-crown-6 Salt

In this section, the magnetic, electronic, and thermal properties of the present 3D structure are described. The magnetic susceptibility was measured for polycrystalline samples of [Rb@*crown*]<sub>x</sub>[(-)-NDI-Δ]. Figure 4.7 shows the temperature dependence of the paramagnetic susceptibility. This data was fitted with the Curie Weiss law and the fitting parameters are estimated as  $C = 1.5 \times 10^{-4} \text{ emu K g}^{-1}$  and  $\theta = -7.6 \text{ K}$ . This negative Weiss constant indicates an antiferromagnetic interaction. The molar Curie constant is estimated as  $0.30 \text{ emu K mol}^{-1}$  by using the ratios of (-)-NDI-Δ estimated from the elemental analysis in Section 4.3. This value is 80% of the theoretical one for  $S = 1/2$  spins with  $g = 2$ , indicating that (-)-NDI-Δ is in a mono radical state. This is nearly consistent with the valence of (-)-NDI-Δ suggested from the X-ray analysis.

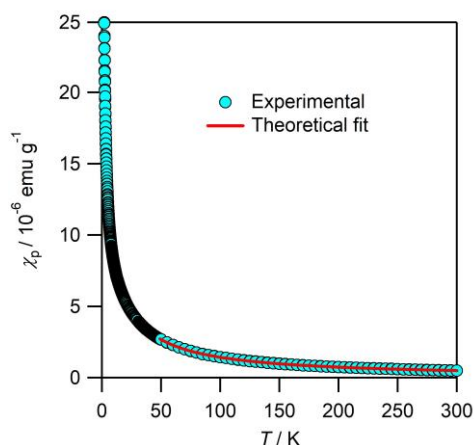


**Figure 4.7.** Temperature dependence of the paramagnetic susceptibility  $\chi_p$  for [Rb@*crown*]<sub>x</sub>[(-)-NDI-Δ].

The temperature dependence of the conductivity for  $[\text{Rb@crown}]_x[(-)\text{-NDI-}\Delta]$  was measured on a single crystal with a two-probe method along the  $c$ -axis (Figure 4.8). The theoretical fit to the experimental data with Eq. (2.1) gives an activation energy of 0.2 eV. The insulating property is consistent with the Curie-Weiss behavior in the magnetic measurements.

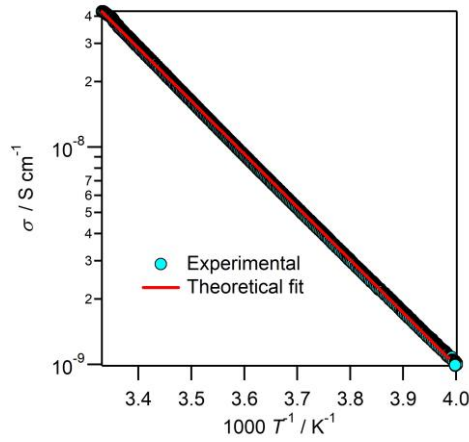


**Figure 4.8.** Temperature dependence of the conductivity for  $[\text{Rb@crown}]_x[(-)\text{-NDI-}\Delta]$  along the  $c$ -axis in the temperature range of 250–300 K.

The magnetic and conductivity measurements indicated a localized-electron nature of  $[\text{Rb@crown}]_x[(-)\text{-NDI-}\Delta]$ . This electron localization could cause a spin frustration in the present system in a similar manner as discussed in the TBA salt in Chapter 3. Thus, the temperature dependence of the heat capacity was measured for  $[\text{Rb@crown}]_x[(-)\text{-NDI-}\Delta]$  to examine a gapless excitation related to spin frustration. Figure 4.9(a) shows the temperature dependence of the heat capacity  $c_p$  for  $[\text{Rb@crown}]_x[(-)\text{-NDI-}\Delta]$  in the temperature range of 2–50 K. The values of  $c_p$  gradually decrease with decreasing temperature, and no long-range magnetic ordering is observed in this measurement. Figure 4.9(b) shows  $c_p/T$  vs  $T^2$  plots in the low-temperature range.

The red line shows a linear relation between  $c_p/T$  and  $T^2$  and the fitting parameters are estimated with Eq. (3.8) as follows:  $\beta = 0.032 \text{ mJ K}^{-4} \text{ g}^{-1}$  and  $\gamma = 0.074 \text{ mJ K}^{-1} \text{ g}^{-1}$ . These values can be converted to  $\beta = 63 \text{ mJ K}^{-4} \text{ mol}^{-1}$  and  $\gamma = 144 \text{ mJ K}^{-1} \text{ mol}^{-1}$  by using the ratios of (-)-NDI- $\Delta$  estimated from the elemental analysis. This large  $\gamma$  value indicates a gapless excitation in this system. It is worth noting that, although the present system includes a structural disorder in the void space, the contribution from such randomness would be negligible compared to the observed value, because the typical  $\gamma$  values for the structurally glassy organic materials are lower than  $0.028 \text{ mJ K}^{-2} \text{ g}^{-1}$ .<sup>215</sup> Since the present system is insulating, the gapless excitation could be related to the spin frustration.

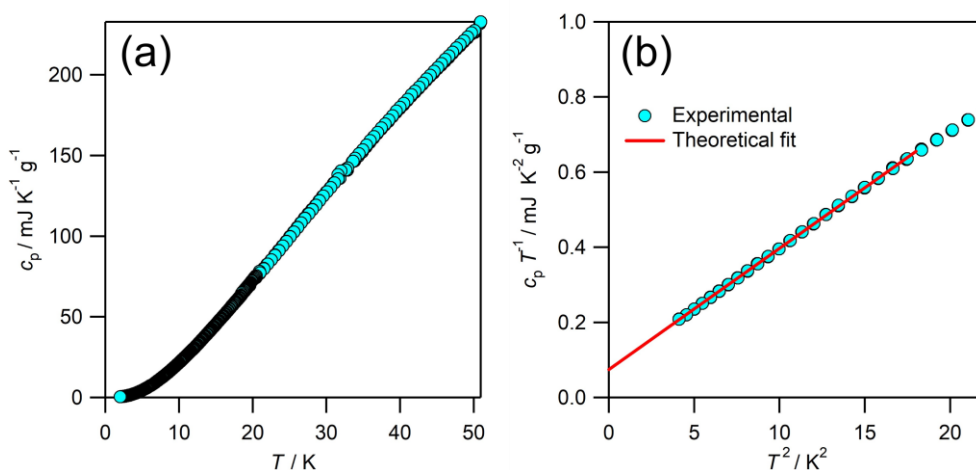


**Figure 4.9.** (a) Temperature dependence of the heat capacity  $c_p$  for  $[\text{Rb@crown}]_x[(-)\text{-NDI-}\Delta]$ . (b)  $c_p/T$  vs  $T^2$  plots in the low-temperature range.

## 4.5 Conclusion

Black block or black needle crystals of the radical anion salts of (-)-NDI- $\Delta$  were successfully grown in the PC solutions of the alkali electrolytes and the cyclic multidentate ligands. The X-ray analyses for the crystals grown with the 18-crown-6

molecules with Rb or K ions exhibited the tetragonal space group of  $I4_1$ , which is different from that for the  $K_4$  crystals.

The X-ray structural analysis of  $[\text{Rb@crown}]_x[(-)\text{-NDI-}\Delta]$  revealed the novel 3D network of the radical anions of  $(-)\text{-NDI-}\Delta$ , with the helices of two different chirality. The coordination structure of the 18-crown-6, PC, and  $(-)\text{-NDI-}\Delta$  to the Rb ions was solved, and the two types of chiral dimers, (*P*)- and (*M*)-helical dimers, were observed. The two types of chiral dimers led to the coexistence of the helices of two different chirality which were formed by the  $\pi$ - $\pi$  interactions between the chiral  $(-)\text{-NDI-}\Delta$  molecules. The coordination structure of the 18-crown-6 molecules to the Rb ions is considered as an important factor to induce the present 3D structure. The inhomogeneous distribution of the Rb ions was also observed.

The chemical components of  $[\text{Rb@crown}]_x[(-)\text{-NDI-}\Delta]$  were analyzed by the elemental analysis and IR, EDX, and UV-VIS-NIR measurements. The results of the elemental analysis indicated that 53.12% of this salt was  $(-)\text{-NDI-}\Delta$ . The IR and UV-VIS-NIR measurements indicated the presence of the radical anions of  $(-)\text{-NDI-}\Delta$  and the broad band which was characteristic of the solid-state.

The temperature dependence of the paramagnetic susceptibility for  $[\text{Rb@crown}]_x[(-)\text{-NDI-}\Delta]$  showed the Curie-Weiss behavior with an antiferromagnetic interaction of  $-7.6$  K and a molar Curie constant of  $0.30 \text{ emu K mol}^{-1}$ . This Curie constant roughly agreed with that of  $S = 1/2$  spins with  $g = 2$ . The temperature dependence of the conductivity for  $[\text{Rb@crown}]_x[(-)\text{-NDI-}\Delta]$  showed insulating properties. These electronic and magnetic measurements indicated the localized-electron nature of this system. The temperature dependence of the heat capacity for  $[\text{Rb@crown}]_x[(-)\text{-NDI-}\Delta]$  showed no indication of magnetic ordering down to 2 K, and the presence of the linear

heat capacity coefficient  $\gamma$  was revealed. Though the valence of (-)-NDI- $\Delta$  was not clear, the finite  $\gamma$  value along with the insulating properties suggested the spin frustration in this system.

## 4.6 Experimental Section

Unless otherwise noted, all chemicals were used without further purification. 15-crown-5, 18-crown-6, 2,2,2-cryptand, HClO<sub>4</sub>, Rb•Cl, Cs•Cl, and K•ClO<sub>4</sub> were purchased from Waco Pure Chemical Industries, Ltd. PC was purchased from Tokyo Chemical Industry Co., Ltd., and was dried with molecular sieves 4A 1/16 (Waco Pure Chemical Industries, Ltd.) before use. 18-crown-6 and 2,2,2-cryptand were roughly dried under vacuum for an hour right before use. (-)-NDI- $\Delta$ , Rb•ClO<sub>4</sub>, and Cs•ClO<sub>4</sub> were prepared with the same procedures as described in Section 2.8.

### 4.6.1 Preparation of (-)-NDI- $\Delta$ Radical Anion Salts

Electrolyte solutions of PC containing electrolytes and cyclic multidentate ligands (18-crown-6 or 15-crown-5 or 2,2,2-cryptand) were prepared. The concentration of the electrolyte was set to 0.1 M, and the electrolyte and the ligand were mixed with the molar ratios of 1:2 for 15-crown-5 and 18-crown-6, and of 1:1 for 2,2,2-cryptand. (-)-NDI- $\Delta$  was placed on the cathode side of the glass cells, and the electrocrystallization was carried out with the same procedure as described in Section 2.8.1. The crystals used for magnetic, electronic, and thermal measurements were washed several times with PC in an N<sub>2</sub> atmosphere, and were dried under vacuum. Elemental analysis and IR, EDX, and diffuse

reflectance UV-VIS-NIR measurements for  $[\text{Rb@crown}]_x[(-)\text{-NDI-}\Delta]$  were carried out with the same procedures as described in Sections 2.8.1 and 3.9.1.

#### 4.6.2 X-ray Structural Analysis

The X-ray diffraction data were collected on a Rigaku R-AXIS RAPID diffractometer equipped with a MicroMax007HF microfocus generator, a VariMax DW optic, and a RAPID IP detector by using Cu-K $\alpha$  radiation ( $\lambda = 1.54187 \text{ \AA}$ ) under a cold nitrogen stream at 123 K. No diffraction spot was observed at high-angle regions ( $< 0.99 \text{ \AA}$ ) as shown in Figure 4.10.

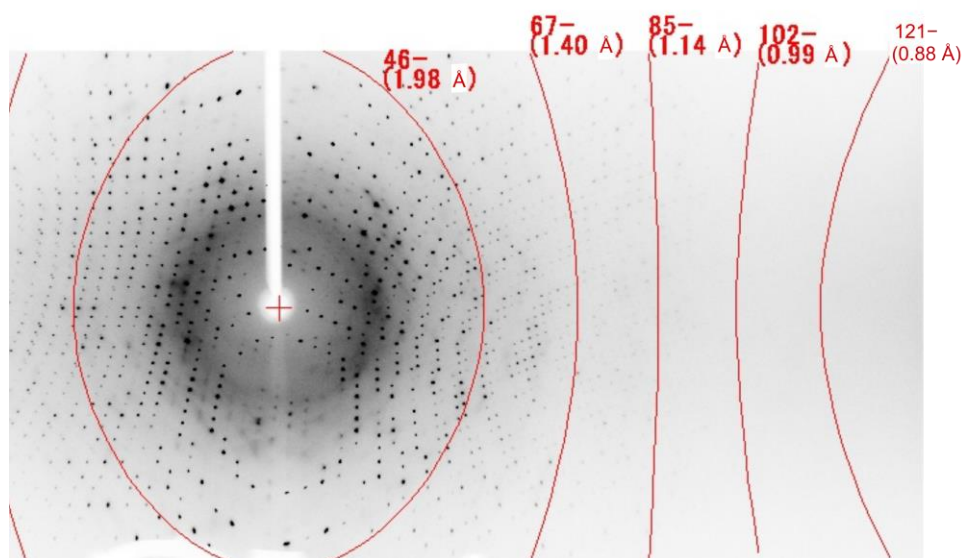


**Figure 4.10.** X-ray diffraction image of  $[\text{Rb@crown}]_x[(-)\text{-NDI-}\Delta]$ .

The frame data were integrated and corrected for absorption with the Rigaku RAPID AUTO package.<sup>190</sup> The structure was solved by direct method (SHELXS97<sup>170</sup>) and standard difference map techniques, and was refined with full-matrix least-square procedures on  $F^2$ . All calculations were performed using the crystallographic software

package, Crystal Structure,<sup>216</sup> except for refinement, which was performed using SHELXL Version 2016/4.<sup>170</sup> Anisotropic refinement was applied to all non-hydrogen atoms. A part of a disordered (-)-NDI- $\Delta$  was refined with restraints on the anisotropic displacement parameters (SIMU and DELU commands). A disordered PC was refined with restraints on the bond lengths (DFIX and DANG commands) and constraints on the anisotropic displacement parameters (EADP commands). All hydrogen atoms were placed at calculated positions and refined using a riding model. The electron densities in the 3D cavity were flattened, using the SQUEEZE subroutine of PLATON,<sup>157</sup> and only the 3D network structure of (-)-NDI- $\Delta$  radical anions, and Rb ions, PCs, and 18-crown-6 molecules near (-)-NDI- $\Delta$ , were refined.

### **4.6.3 Magnetic, Electronic, and Heat-capacity Measurements**

Magnetic and conductivity measurements were carried out with the same procedures as described in Section 2.8.3. Heat-capacity measurements were carried out in the temperature range of 2–50 K on a PPMS and the data were calibrated with copper as described in Section 3.9.4.

# Chapter 5 Supramolecular Crystal Structures of Charge-Transfer Complexes of (-)-NDI- $\Delta$

## 5.1 Introduction

Dimensionality is one of the most important factors for molecular conductors and magnets, as described in Sections 1.1 and 1.2. Development of molecular conductors and magnets is accompanied by an increase in the dimensionality of the intermolecular interactions, and the radical anion complexes of  $C_{60}$  are successful 3D materials which exhibit high- $T_c$ -superconductivity<sup>37,38</sup> and ferromagnetism.<sup>39,40</sup> Usual planar aromatic molecules tend to be stacked 1D to form face-to-face stacking columns in their crystals. Even though the low dimensionality can induce the unusual properties such as low-dimensional magnetism<sup>30,31</sup> and Peierls instability,<sup>7,8</sup> they are not suitable to realize 3D interactions. One approach to control the dimensionality is proposed by Inabe et al.<sup>51,52</sup> They have developed the radical cation salts of axially-ligated phthalocyanines, in which the steric hindrance of the coordinated  $CN^-$  ions induced the 1D and 2D  $\pi$ - $\pi$  stacking structures. In their works, the different dimensionality was an important factor to govern the electronic and magnetic properties.

In the previous chapters, the excellent ability of (-)-NDI- $\Delta$  as a building block for 3D crystals was indicated. In addition to the 3D structures, (-)-NDI- $\Delta$  may also form 1D and 2D structures by the  $\pi$ - $\pi$  interactions between the triangles. Use of charge-transfer (CT) interactions between donor and acceptor molecules is an important approach to

make molecular conductors and magnets. Thus, the triangular molecule along with the CT interactions may result in novel crystal packings with novel functionality.

In Chapter 5, the author firstly describes the preparation and the X-ray analyses of single crystals of CT complexes of (-)-NDI- $\Delta$ . Packing motifs of these crystals are much different from those of usual CT complexes due to the triangular shape of (-)-NDI- $\Delta$ , and the dimensionality in them is significantly affected by solvents and donor molecules. The diffuse reflectance spectra of the CT complexes are described to discuss the CT interactions between (-)-NDI- $\Delta$  and donor molecules.

## **5.2 Preparation and X-ray Analysis of CT Complexes of (-)-NDI- $\Delta$**

In this section, the crystal structures of the CT complexes between (-)-NDI- $\Delta$  and donor molecules are described. The CT complexes of (-)-NDI- $\Delta$  were prepared with the following donors, TTF, perylene, and pyrene, by slow evaporation of the solutions of the parent compounds. Table 5.1 lists the crystallization conditions and the obtained crystals. 1,2-dichloroethane (DCE) and 1,2-dibromoethane (DBE) were used as solvents to control the structures by halogen-halogen interactions. The single crystals of the eight CT complexes were obtained and the X-ray analyses were carried out for these crystals. Four of the eight crystals were successfully analyzed, and the chemical formulae in Table 5.1 correspond to the asymmetric units of these complexes. The structural analyses of the other crystals were not successful due to a significant disorder of the solvents and the degradation of the crystallinity caused by the solvent loss.

**Table 5.1.** Combinations of the donors and the solvents used for the crystallization of the CT complexes of (-)-NDI- $\Delta$ .

TTF		
Solvent	Crystal habit	Chemical Formula
CH <sub>3</sub> CN	Green block	$[(-)\text{-NDI-}\Delta]_2[\text{TTF}]_4 \cdot 6(\text{CH}_3\text{CN})$
DCE	Green needle	$[(-)\text{-NDI-}\Delta]_2[\text{TTF}]_2 \cdot 6(\text{DCE})$
DBE	Brown precipitation	n/a
Perylene (Pery)		
CH <sub>3</sub> CN	Green needle	$[(-)\text{-NDI-}\Delta]_4[\text{Pery}]_5 \cdot 6(\text{CH}_3\text{CN})$
DCE		n/a
DBE	Green block	n/a
Pyrene (Py)		
CH <sub>3</sub> CN	Red needle	$[(-)\text{-NDI-}\Delta][\text{Py}]$
DCE		n/a
DBE	Red block	n/a

### 5.2.1 TTF Complexes

Table 5.2 lists the crystallographic data for the TTF complexes,  $[(-)\text{-NDI-}\Delta]_2[\text{TTF}]_4 \cdot 6(\text{CH}_3\text{CN})$  and  $[(-)\text{-NDI-}\Delta]_2[\text{TTF}]_2 \cdot 6(\text{DCE})$ . The electron densities corresponding to the disordered solvents in  $[(-)\text{-NDI-}\Delta]_2[\text{TTF}]_4 \cdot 6(\text{CH}_3\text{CN})$  were flattened by using SQUEEZE subroutine of PLATON.<sup>157</sup> These crystals belong to the same space group, the *P1*, though their crystal packings are completely different. Figure 5.1(a) shows the asymmetric unit of  $[(-)\text{-NDI-}\Delta]_2[\text{TTF}]_4 \cdot 6(\text{CH}_3\text{CN})$ . The asymmetric unit consists of four TTFs, and two (-)-NDI- $\Delta$  and six CH<sub>3</sub>CN molecules. Each (-)-NDI- $\Delta$  molecule has  $\pi$ - $\pi$  interactions with two TTFs, and no continuous 1D  $\pi$ - $\pi$  stacking is observed between the donor and acceptor molecules. Figures 5.1(b) and 5.1(c) show a dimeric stacked structure formed between two (-)-NDI- $\Delta$  molecules viewed along the stacking direction and the side view of the stacking, respectively. The C-H $\cdots$ O hydrogen bonds are observed between the dimeric (-)-NDI- $\Delta$  molecules.

**Table 5.2.** Crystallographic data for the TTF complexes.

	$[(-)\text{-NDI-}\Delta]_2$ [TTF] <sub>4</sub> •6(CH <sub>3</sub> CN)	$[(-)\text{-NDI-}\Delta]_2$ [TTF] <sub>2</sub> •6(DCE)
Formula	C <sub>78</sub> H <sub>59</sub> N <sub>9</sub> O <sub>12</sub> S <sub>8</sub>	C <sub>72</sub> H <sub>48</sub> Cl <sub>6</sub> N <sub>6</sub> O <sub>12</sub> S <sub>4</sub>
Formula weight / g mol <sup>-1</sup>	1570.86	1530.16
Temperature / K	123	150
Crystal dimensions / mm <sup>3</sup>	0.14 × 0.11 × 0.09	0.20 × 0.04 × 0.04
System	Triclinic	Triclinic
Space group	<i>P</i> 1 (#1)	<i>P</i> 1 (#1)
<i>a</i> / Å	16.1474(13)	14.8839(3)
<i>b</i> / Å	16.3258(13)	15.4960(3)
<i>c</i> / Å	17.0746(13)	15.6262(3)
$\alpha$ / °	68.987(4)	99.2960(7)
$\beta$ / °	67.837(4)	104.0400(7)
$\gamma$ / °	70.889(4)	94.5410(7)
<i>V</i> / Å <sup>3</sup>	3794.1(5)	3423.99(11)
<i>Z</i>	2	2
$\rho_{\text{calcd}}$ / g cm <sup>-3</sup>	1.375	1.484
$\mu$ / cm <sup>-1</sup>	3.033 (MoK $\alpha$ )	40.022 (CuK $\alpha$ )
$\lambda$ / Å	0.71070	1.54187
$2\theta_{\text{max}}$ / °	55.0	136.5
Reflections collected	30597	62570
Unique reflections ( <i>R</i> <sub>int</sub> )	23427 (0.0230)	22547 (0.0810)
Number of parameters	1933	1812
Number of restraints		16
Final <i>R</i> <sub>1</sub> [ <i>I</i> > 2σ( <i>I</i> )]	0.0472	0.0827
<i>wR</i> <sub>2</sub> (all data)	0.1139	0.2497
Goodness of fit	1.046	1.068
Flack parameter	0.03(3)	0.030(12)
Residual electron density / Å <sup>-3</sup>	1.03 e <sup>-</sup>	0.52 e <sup>-</sup>
Void fraction	9.4%	

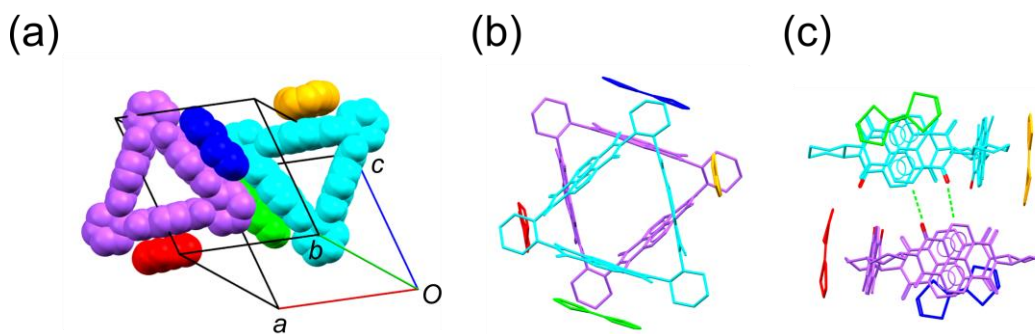


**Figure 5.1.** Crystal structure of  $[(-)\text{-NDI-}\Delta]_2[\text{TTF}]_4\cdot 6(\text{CH}_3\text{CN})$ .  $\text{CH}_3\text{CN}$  molecules are omitted for clarify. (a) Asymmetric unit, (b) dimeric stacked structure of the two  $(-)\text{-NDI-}\Delta$  molecules, and (c)  $\text{C-H}\cdots\text{O}$  hydrogen bonds between the  $(-)\text{-NDI-}\Delta$  molecules in the dimer.

Next, the crystal structure of  $[(-)\text{-NDI-}\Delta]_2[\text{TTF}]_2\cdot 6(\text{DCE})$  is described. Figure 5.2(a) shows a 1D columnar stacking formed between the  $(-)\text{-NDI-}\Delta$  molecules along the  $c$  axis. Along this stacking direction, the  $\text{C-H}\cdots\text{O}$  hydrogen bonds are observed in a similar fashion as seen in  $[(-)\text{-NDI-}\Delta]_2[\text{TTF}]_4\cdot 6(\text{CH}_3\text{CN})$ . Liu et al.<sup>141</sup> discuss this type of 1D columnar stacking of  $(-)\text{-NDI-}\Delta$ , on the basis of the  $\text{C-H}\cdots\text{O}$  hydrogen bonds between  $(-)\text{-NDI-}\Delta$  molecules and the halogen-halogen interactions between DCE or DBE molecules in the cavity (see Section 1.5). In the present crystal,  $[(-)\text{-NDI-}\Delta]_2[\text{TTF}]_2\cdot 6(\text{DCE})$ , the 1D cavity space incorporates DCE molecules, while no short contact between the Cl atoms is observed. Thus, the halogen-halogen interactions may not be important for the 1D columnar stacking in this crystal. Regarding the  $\pi$ - $\pi$  interactions, each  $(-)\text{-NDI-}\Delta$  molecule has  $\pi$ - $\pi$  interactions with one TTF. It is notable that all of the NDI units don't show the  $\pi$ - $\pi$  interactions with the TTFs. This is much different from usual CT complexes in which all of the donor and acceptor molecules show  $\pi$ - $\pi$  interactions. Figure 5.2(b) shows the projection of the structure along the  $[00\bar{1}]$  direction, indicating no  $\pi$ - $\pi$  interaction between the 1D stacking columns.

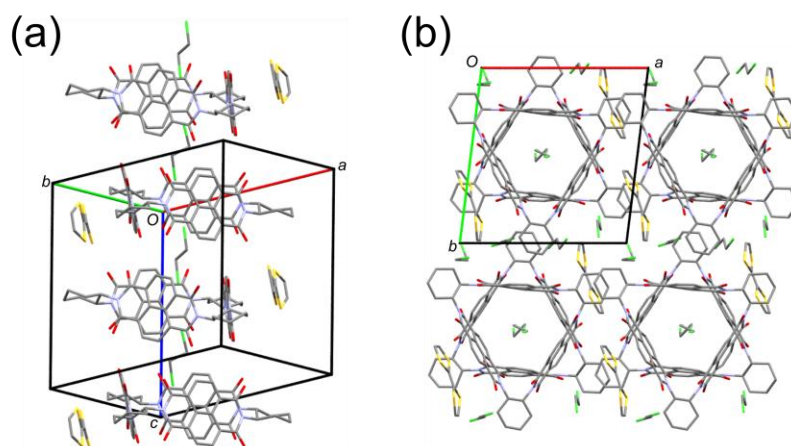


**Figure 5.2.** 1D columnar stacking of (-)-NDI- $\Delta$  along the  $c$  axis (a), and projection of the structure along the  $[00\bar{1}]$  direction (b) in  $[(-)\text{-NDI-}\Delta]_2[\text{TTF}]_2 \cdot 6(\text{DCE})$ .

The degree of the CT  $\rho$  is estimated by the empirical method;<sup>217</sup> the  $\rho$  values can be calculated by using the lengths of C=C bond, and C-S bonds next to the C-C double bond in TTF. Table 5.3 lists the obtained values of  $\rho$ , which indicate that they are neutral CT complexes.

**Table 5.3.** Degree of the CT  $\rho$  of the TTF complexes of (-)-NDI- $\Delta$ .

	No.	$\rho$
	1	-0.13
$[(-)\text{-NDI-}\Delta]_2[\text{TTF}]_4 \cdot 6(\text{CH}_3\text{CN})$	2	0.07
	3	0.08
	4	0.18
	1	0.25
$[(-)\text{-NDI-}\Delta]_2[\text{TTF}]_2 \cdot 6(\text{DCE})$	2	0.31

### 5.2.2 Pyrene and Perylene Complexes

In this section, the crystal structures of the pyrene and perylene complexes of (-)-NDI- $\Delta$  are described for comparison with those of the TTF complexes. Table 5.4 lists the crystallographic data for  $[(-)\text{-NDI-}\Delta][\text{Py}]$  and  $[(-)\text{-NDI-}\Delta]_4[\text{Pery}]_5 \cdot 6(\text{CH}_3\text{CN})$ . The

electron densities corresponding to the disordered solvents were flattened by using SQUEEZE subroutine of PLATON.<sup>157</sup> Figure 5.3 shows the crystal structure of [(-)-NDI- $\Delta$ ][Py]. In Figure 5.3(a), the pyrene and (-)-NDI- $\Delta$  molecules are alternately stacked along the *b* axis, and a 1D donor-acceptor chain is formed along this direction. The (-)-NDI- $\Delta$  molecules exhibit 2-way  $\pi$ - $\pi$  interactions with the pyrenes. Figure 5.3(b) shows the projection of the structure along the  $[0\bar{1}0]$  direction, which indicates that the 1D donor-acceptor chains are packed in a herringbone manner.

Next, the crystal structure of [(-)-NDI- $\Delta$ ]<sub>4</sub>[Pery]<sub>5</sub>•6(CH<sub>3</sub>CN) is described. Figure 5.4(a) shows a layer structure formed by perylene and (-)-NDI- $\Delta$ . Two of the four non-equivalent (-)-NDI- $\Delta$  molecules exhibit 3-way  $\pi$ - $\pi$  interactions and the others exhibit 2-way  $\pi$ - $\pi$  interactions. These interactions result in a hexagonal structure expanding to one direction, and there is no  $\pi$ - $\pi$  interaction between the orange and red triangles. This structure is similar to that of graphene nanoribbons which are strips of graphene. Thus, the structure is not regarded as a honeycomb lattice, but as a molecule-based “graphene nanoribbon.” The hexagonal structure is a unique structure, which strongly reflects the triangle shape of (-)-NDI- $\Delta$ . Figure 5.4(b) shows the intralayer arrangement. Interestingly, the relative positions of the perylenes to the NDI units show three types of positions, up, middle, and down. Figure 5.4(c) shows the interlayer arrangement. The next layers don't show eclipsed overlap; (-)-NDI- $\Delta$  molecules in the next layer exist above the perylenes. A part of the perylenes with the up and down positions exist in the intramolecular cavities of (-)-NDI- $\Delta$ , having short contacts with the NDI units inside the (-)-NDI- $\Delta$  molecules.

**Table 5.4.** Crystallographic data for the pyrene and perylene complexes.

	[(-)-NDI- $\Delta$ ][Py]	[(-)-NDI- $\Delta$ ] <sub>4</sub> [Pery] <sub>5</sub> •6(CH <sub>3</sub> CN)
Formula	C <sub>76</sub> H <sub>52</sub> N <sub>6</sub> O <sub>12</sub>	C <sub>352</sub> H <sub>246</sub> N <sub>30</sub> O <sub>48</sub>
Formula weight / g mol <sup>-1</sup>	1241.28	5663.99
Temperature / K	150	150
Crystal dimensions / mm <sup>3</sup>	0.20 × 0.08 × 0.08	0.22 × 0.10 × 0.06
System	Orthorhombic	Triclinic
Space group	<i>P</i> 2 <sub>1</sub> 2 <sub>1</sub> 2 <sub>1</sub> (#19)	<i>P</i> 1 (#1)
<i>a</i> / Å	10.65206(19)	17.0594(3)
<i>b</i> / Å	24.2875(4)	20.5183(4)
<i>c</i> / Å	25.5866(5)	25.0511(5)
$\alpha$ / °		64.9140(7)
$\beta$ / °		87.3550(7)
$\gamma$ / °		85.4830(7)
<i>V</i> / Å <sup>3</sup>	6619.6(2)	7916.1(3)
<i>Z</i>	4	1
$\rho_{\text{calcd}}$ / g cm <sup>-3</sup>	1.245	1.188
$\mu$ (MoK $\alpha$ ) / cm <sup>-1</sup>	6.994	6.528
$\lambda$ / Å	1.54187	1.54187
2 $\theta_{\text{max}}$ / °	136.4	136.5
Reflections collected	121984	145542
Unique reflections ( <i>R</i> <sub>int</sub> )	12108 (0.0628)	52196 (0.0472)
Number of parameters	847	3877
Final <i>R</i> <sub>1</sub> [ <i>I</i> > 2 $\sigma$ ( <i>I</i> )]	0.0496	0.0579
<i>wR</i> <sub>2</sub> (all data)	0.1138	0.1430
Goodness of fit	1.047	0.943
Flack parameter	0.13(8)	0.16(6)
Residual electron density / Å <sup>-3</sup>	0.19 e <sup>-</sup>	0.20 e <sup>-</sup>
Void fraction	20.7%	21.4%

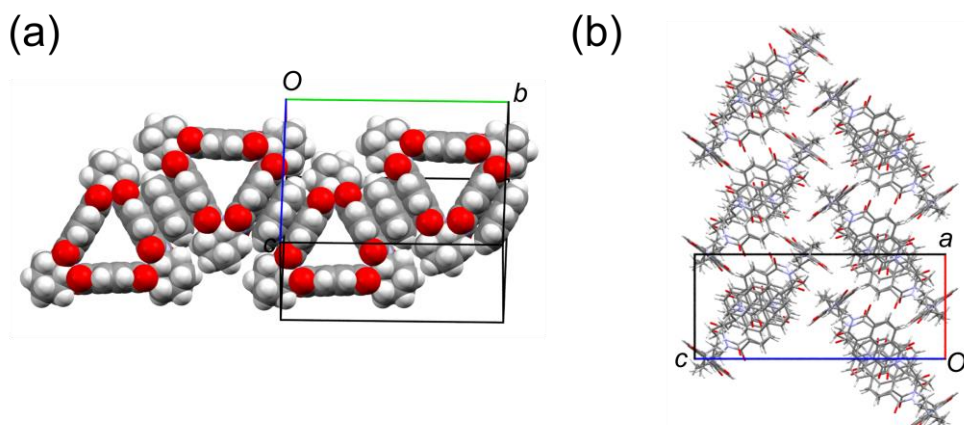


**Figure 5.3.** Crystal structure of [(-)-NDI-Δ][Py]. CH<sub>3</sub>CN molecules are omitted for clarify. (a) 1D donor-acceptor alternated chain along the *b* axis, and (b) herringbone packing of the 1D chains viewed along the  $[0\bar{1}0]$  direction.

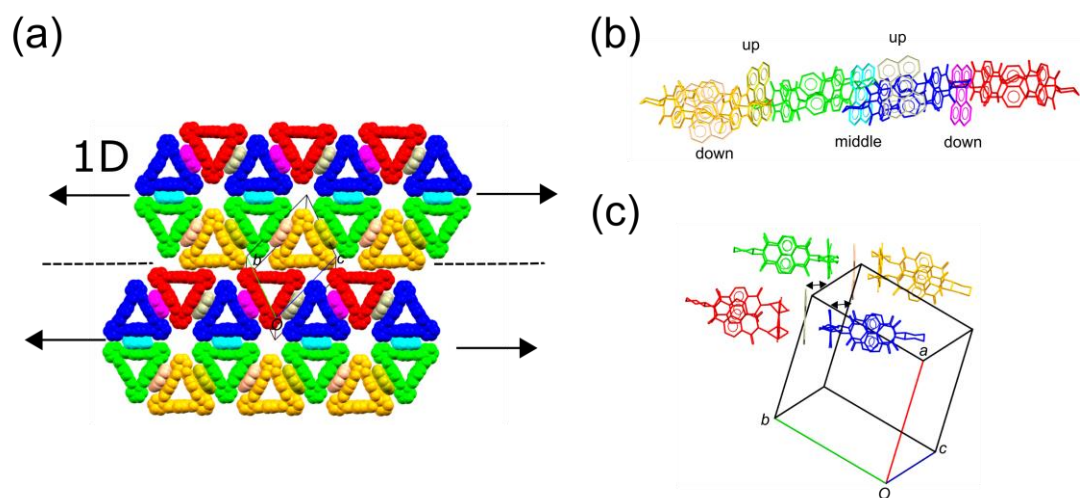


**Figure 5.4.** Hexagonal structure formed by the CT interactions between the perylene and (-)-NDI-Δ molecules (a), intralayer arrangement (b), and interlayer arrangement (c) in [(-)-NDI-Δ]<sub>4</sub>[Pery]<sub>5</sub>•6(CH<sub>3</sub>CN). CH<sub>3</sub>CN molecules are omitted for clarify.

### 5.3 Diffuse Reflectance Spectra of CT Complexes

In the previous chapter, the formation of the CT crystals between (-)-NDI- $\Delta$  and the donor molecules were revealed by X-ray analysis. In this chapter, the diffuse reflectance measurements were carried out for the CT crystals to discuss the CT interactions between (-)-NDI- $\Delta$  and the donor molecules. The UV-VIS-NIR diffuse reflectance spectra were measured for [(-)-NDI- $\Delta$ ]<sub>2</sub>[TTF]<sub>4</sub>•6(CH<sub>3</sub>CN), [(-)-NDI- $\Delta$ ][Py], and [(-)-NDI- $\Delta$ ]<sub>4</sub>[Pery]<sub>5</sub>•6(CH<sub>3</sub>CN). Note that the PXRD spectra of the grinded samples of these complexes didn't show any signals, indicating that their crystallinity were lost probably due to the solvent loss. Figure 5.5 shows the UV-VIS-NIR diffuse reflectance spectra of these complexes. The red curves show broad absorptions which are characteristic of the CT interactions. Table 5.5 lists the peak wavelength and the potentials of the 0/+1 redox processes for the donor molecules. The CT complexes of the stronger donor molecules show the stronger red shifts of the CT bands, which is typical for usual CT complexes. TTF is the strongest donor among the three donor molecules, and the absorption energy for the TTF complex is ca. 1.5 eV (~ 800 nm). By considering the Torrance curve which is an empirical measure of the ionicity for CT complexes,<sup>220</sup> this energy is far from the boundary between neutral and ionic CT complexes (~ 0.7 eV), indicating that these complexes are neutral CT complexes. This is consistent with the obtained values of CT estimated for the TTF complexes of (-)-NDI- $\Delta$ , based on the bond lengths of TTFs. Thus, these CT complexes are not suitable to investigate the electronic and magnetic properties.

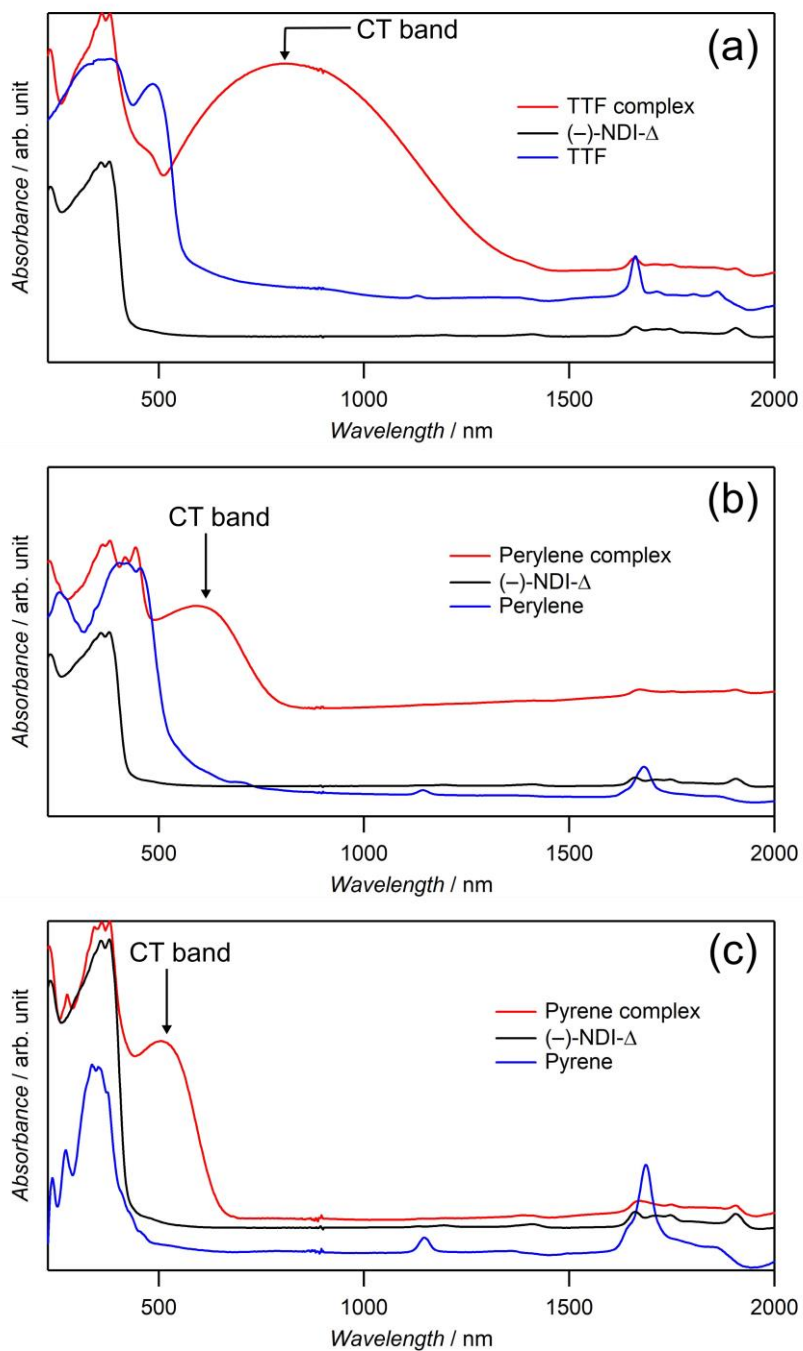


**Figure 5.5.** UV-VIS-NIR diffuse reflectance spectra for  $[(-)\text{-NDI-}\Delta]_2[\text{TTF}]_4 \cdot 6(\text{CH}_3\text{CN})$  (a),  $[(-)\text{-NDI-}\Delta]_4[\text{Pery}]_5 \cdot 6(\text{CH}_3\text{CN})$  (b), and  $[(-)\text{-NDI-}\Delta][\text{Py}]$  (c). The spectra for the parent compounds are also shown for comparison.

**Table 5.5.** Absorption data of the CT complexes of (-)-NDI- $\Delta$  and the potentials of the 0/+1 redox processes for the donor molecules.

Donor	$\lambda_{\max}$ / nm	$E_{\text{ox}}^{1/2}$ / V vs. SCE
TTF	808	0.40 <sup>A</sup>
Perylene	590	0.85 <sup>B</sup>
Pyrene	508	1.16 <sup>B</sup>

<sup>A</sup> Ref. [218]. <sup>B</sup> Ref. [219].

## 5.4 Conclusion

The various CT crystals of the donors and (-)-NDI- $\Delta$  were successfully grown in the various solvents, and their crystal structures with different crystal packings were solved by X-ray analysis. [(-)-NDI- $\Delta$ ]<sub>2</sub>[TTF]<sub>4</sub>•6(CH<sub>3</sub>CN) exhibited the dimeric stacked structure formed between the two (-)-NDI- $\Delta$  molecules with the C-H...O hydrogen bonds. On the other hand, [(-)-NDI- $\Delta$ ]<sub>2</sub>[TTF]<sub>2</sub>•6(DCE) exhibited the 1D columnar stacking of the (-)-NDI- $\Delta$  molecules. In these crystals, no continuous 1D  $\pi$ - $\pi$  stacking was observed between the TTF and (-)-NDI- $\Delta$  molecules. The degrees of the CT estimated for the TTF complexes indicated that they were neutral CT complexes.

[(-)-NDI- $\Delta$ ][Py] exhibited the 1D donor-acceptor alternated chains, which were packed in a herringbone manner. [(-)-NDI- $\Delta$ ]<sub>4</sub>[Pery]<sub>5</sub>•6(CH<sub>3</sub>CN) exhibited the 1D structures, which is regarded as a molecule-based “graphene nanoribbon.” These structures were characteristic of the triangular shape of (-)-NDI- $\Delta$ , and much different from usual 1D alternated stacks of neutral CT complexes. The CT interactions between (-)-NDI- $\Delta$  and the donor molecules were confirmed by the diffuse reflectance measurements for the TTF, pyrene, and perylene complexes of (-)-NDI- $\Delta$ . The CT

complexes of the polyhedral  $\pi$ -conjugated molecule showed the unique molecular arrangements, which are much different from those of usual planar molecules.

## 5.5 Experimental Section

Unless otherwise noted, all chemicals were used without further purification. 1,2-dichloroethane (DCE), and 1,2-dibromoethane (DBE) were purchased from Waco Pure Chemical Industries, Ltd. TTF, perylene, and pyrene were purchased from Tokyo Chemical Industry Co., Ltd. CH<sub>3</sub>CN was purchased from Nacalai Tesque, Inc. (-)-NDI- $\Delta$  was prepared with the same procedures as described in Section 2.8.1. Diffuse reflectance UV-VIS-NIR spectra of CT complexes were measured with the same procedure as described in Section 3.9.1. Powder X-ray diffraction of CT complexes was carried out for the grinded samples on a Rigaku Multiflex by using Cu-K $\alpha$  radiation.

The X-ray diffraction data of [(-)-NDI- $\Delta$ ]<sub>2</sub>[TTF]<sub>4</sub>•6(CH<sub>3</sub>CN) were collected on a Rigaku AFC-10 instrument equipped with a Saturn 70 CCD detector by using graphite-monochromated Mo K $\alpha$  radiation ( $\lambda = 0.71075 \text{ \AA}$ ) under a cold nitrogen stream at 123 K. The X-ray diffraction data of [(-)-NDI- $\Delta$ ]<sub>2</sub>[TTF]<sub>2</sub>•6(DCE), [(-)-NDI- $\Delta$ ]<sub>4</sub>[Pery]<sub>5</sub>•6(CH<sub>3</sub>CN), and [(-)-NDI- $\Delta$ ][Py] were collected on a Rigaku R-Axis RAPID diffractometer equipped with a MicroMax007HF microfocus generator, a VariMax DW optic, and a RAPID IP detector by using Cu-K $\alpha$  radiation ( $\lambda = 1.54187 \text{ \AA}$ ) under a cold nitrogen stream at 150 K. The frame data were integrated and corrected for absorption with the Rigaku/MSO Crystal Clear package<sup>221</sup> or the Rigaku RAPID AUTO package.<sup>190</sup> The structures were solved by direct methods (SIR92,<sup>222</sup> SHELXT Version 2014/5,<sup>223</sup> and SHELXD Version 2013/2<sup>170</sup>) and standard difference map techniques, and were refined

with full-matrix least-square procedures on  $F^2$ . All calculations were performed using the crystallographic software package, Crystal Structure,<sup>216</sup> except for refinement, which was performed using SHELXL Version 2016/4.<sup>170</sup> Anisotropic refinement was applied to all non-hydrogen atoms. DCE molecules including in  $[(-)\text{-NDI-}\Delta]_2[\text{TTF}]_2 \cdot 6(\text{DCE})$  was refined with restraints and constraints on the bond lengths (DFIX commands) and on the temperature parameters (EADP and SADI commands). All hydrogen atoms were placed at calculated positions and refined using a riding model. The electron densities corresponding to the disordered solvents were flattened, using the SQUEEZE subroutine of PLATON<sup>157</sup> except for  $[(-)\text{-NDI-}\Delta]_2[\text{TTF}]_2 \cdot 6(\text{DCE})$ .

## Chapter 6 Conclusions

In this thesis, the radical anion salts and CT complexes of a triangular electron acceptor, (-)-NDI- $\Delta$ , were prepared and the unique crystal structures with the various dimensionality were revealed by X-ray analysis. Spin-frustrations in the hyperkagome lattices formed in the  $K_4$  crystals of (-)-NDI- $\Delta$  were also examined to elucidate the nature of the 3D organic spin liquid.

In Chapter 2, the radical anion salts of (-)-NDI- $\Delta$  were successfully prepared in the various electrolyte solutions. The X-ray analyses indicated the cubic space groups with the lattice constants of 29.9–30.9 Å, and the structural analysis of the Rb salt grown in PC revealed the  $K_4$  structure of the radical anions of (-)-NDI- $\Delta$  formed only by the unique twisted 3-way  $\pi$ - $\pi$  interactions. The chemical formula of  $\text{Rb}_{1.4}[(-)\text{-NDI-}\Delta]$  was also derived from the X-ray analysis. Further, fascinating features of the band structure (a metallic ground state, the Dirac cones, and the doubly degenerated flat bands) were predicted. However, the electronic and magnetic measurements indicated the localized-electron nature of this system probably due to the weak intramolecular interaction. The obtained crystal is the first example of the organic-radical-based  $K_4$  crystals, and indicate polyhedral  $\pi$ -conjugated molecules with triangular shape is a useful building block for making  $K_4$  crystals.

In Chapter 3, the spin-frustrations in the hyperkagome lattices formed in the  $K_4$  crystals of (-)-NDI- $\Delta$  were investigated. The structural analysis of the TBA salt grown in diglyme revealed the  $K_4$  structure with the chemical formula of  $(\text{TBA})_{1.5}[(-)\text{-NDI-}\Delta]$ , indicating the valence of (-)-NDI- $\Delta$  was -1.5. The determined valence along with the insulating ground state strongly indicated that the present system should be regarded as a

Mott dimer system and that the spin structure, formed by  $S = 1/2$  unpaired electrons, should correspond to a hyperkagome lattice with spin frustration. The temperature dependences of the paramagnetic susceptibility and the  $^{14}\text{N}$  NMR signals indicated no long-range magnetic ordering down to 70 mK and 0.38 K, respectively, in spite of the 3D antiferromagnetic interactions with  $\theta = -15$  K. The temperature dependence of the heat capacity indicated no magnetic ordering down to 68 mK and  $T^{0.62}$  dependence of the heat capacity for the spin liquid state. These magnetic and thermal properties strongly suggested the presence of spin frustration in the hyperkagome lattice and the formation of a spin liquid state. The theoretical understanding of the observed  $T^{0.62}$  dependence of the heat capacity in the present hyperkagome system is a future challenge.

In Chapter 4, the radical anion salts of (–)-NDI- $\Delta$  were prepared in the PC solutions of the alkali electrolytes and the cyclic multidentate ligands. The tetragonal space group of  $I4_1$  was observed for the crystals grown with the 18-crown-6 complexes of Rb or K ions. The X-ray structural analysis of  $[\text{Rb@crown}]_x[(\text{–})\text{-NDI-}\Delta]$  revealed the unusual 3D network of the radical anions of (–)-NDI- $\Delta$  with the helices of two different chirality. The coordination structure of the 18-crown-6 molecules to the Rb ions were related to the structural formation. The solid-state properties suggested the presence of 3D spin frustration in this system.

In Chapter 5, the CT complexes of (–)-NDI- $\Delta$  were prepared with TTF, pyrene, and perylene, and the crystal structures with different dimensionality were solved by X-ray analysis. The structures were characteristic of the triangular shape of (–)-NDI- $\Delta$ , and much different from usual 1D alternated stacks of neutral CT complexes.

In conclusion, the crystal structures and the supramolecular chirality of the radical anion salts and CT complexes of (–)-NDI- $\Delta$  were successfully modulated from 1D to 3D.

It is found that polyhedral  $\pi$ -conjugated organic radicals can produce the exotic crystal structures with high symmetry. Development of novel polyhedral  $\pi$ -conjugated molecules with strong donor (acceptor) moieties are useful to realize unusual solid-state properties with different dimensionality.

## Bibliography

- [1] D. D. Eley, *Nature*, **1948**, 162, 819.
- [2] H. Akamatsu, and H. Inokuchi, *J. Chem. Physics*, **1950**, 18, 810.
- [3] D. D. Eley, G. D. Parfitt, M. J. Perry, and D. H. Taysum, *Trans. Faraday Soc.*, **1953**, 49, 79.
- [4] H. Inokuchi, *Bull. Chem. Soc. Jpn.*, **1954**, 27, 22.
- [5] H. Akamatsu, H. Inokuchi, and Y. Matsunaga, *Nature*, **1954**, 23, 168.
- [6] A. J. Epstein, S. Etemad, A. F. Garito, and A. J. Heeger, *Phy. Rev. B*, **1972**, 5, 952.
- [7] L. B. Coleman, M. J. Cohen, D. J. Sandman, F. G. Yamagishi, A. F. Garito, and A. J. Heeger, *Solid State Commun.*, **1973**, 12, 1125.
- [8] J. Ferraris, D. O. Cowan, V. Walatka, and J. H. Perlstein, *J. Am. Chem. Soc.*, **1973**, 95, 948.
- [9] H. Kobayashi, A. Kobayashi, and H. Tajima, *Chem. Asian J.*, **2011**, 6, 1688.
- [10] G. Saito, and Y. Yoshida, *Frontiers of Organic Conductors and Superconductors. In: Metzger R. (eds) Unimolecular and Supramolecular Electronics I. Topics in Current Chemistry* (Springer, Berlin, Heidelberg, 2011), Vol. 312.
- [11] R. Kato, *Chem. Rev.*, **2004**, 104, 5319.
- [12] D. Jérôme, A. Mazaud, M. Ribault, and K. Bechgaard, *J. Physique Lett.*, **1980**, 41, L95.
- [13] H. Urayama, H. Yamochi, G. Saito, K. Nozawa, T. Sugano, M. Kinoshita, S. Saito, K. Oshima, A. Kawamot, and J. Tanaka, *Chem. Lett.*, **1988**, 1, 55.
- [14] H. Tanaka, Y. Okano, H. Kobayashi, W. Suzuki, and A. Kobayashi, *Science*, **2001**, 291, 285.
- [15] H. Tanaka, M. Tokumoto, S. Ishibashi, D. Graf, E. S. Choi, J. S. Brooks, S. Yasuzuka, Y. Okano, H. Kobayashi, and A. Kobayashi, *J. Am. Chem. Soc.*, **2004**, 126, 10518.
- [16] K. S. Novoselov, A. K. Geim, S. V. Morozov, D. Jiang, M. I. Katsnelson, I. V. Grigorieva, S. V. Dubonos, and A. A. Firsov, *Nature*, **438**, 197.
- [17] K. Kajita, Y. Nishio, N. Tajima, Y. Suzumura, and A. Kobayashi, *J. Phys. Soc. Jpn.*, **2014**, 83, 072002.
- [18] R. Kato, H. B. Cui, T. Tsumuraya, T. Miyazaki, and Y. Suzumura, *J. Am. Chem. Soc.*, **2017**, 139, 1770.
- [19] H. M. McConnell, *J. Chem. Phys.*, **1963**, 39, 1910.
- [20] K. Itoh, *Chem. Phys. Lett.*, **1967**, 1, 235.
- [21] E. Wasserman, R. W. Murray, W. A. Yager, A. M. Trozzolo, and G. Smolinsky, *J. Am. Chem. Soc.*, **1967**, 89, 5076.
- [22] Y. Teki, T. Takui, K. Itoh, H. Iwamura, and K. Kobayashi, *J. Am. Chem. Soc.*, **1983**, 105, 3722.

- [23] T. Sugawara, S. Bandow, K. Kiura, H. Iwamura, and K. Itoh, *J. Am. Chem. Soc.*, **1984**, 6449, 106.
- [24] K. Mukai, *Bull. Chem. Soc. Jpn.*, **1969**, 42, 40.
- [25] K. Awaga, T. Sugano, and M. Kinoshita, *Synth. Metals*, **1988**, 27, B631.
- [26] K. Awaga, and Y. Maruyama, *Chem. Phys. Lett.*, **1989**, 158, 556.
- [27] M. Tamura, Y. Nakazawa, D. Shiomi, K. Nozawa, Y. Hosokoshi, M. Ishikawa, M. Takahashi, and M. Kinoshita, *Chem. Phys. Lett.*, **1991**, 186, 401.
- [28] C. M. Robertson, A. A. Leitch, K. Cvrkalj, R. W. Reed, D. J. T. Myles, P. A. Dube, and R. T. Oakley, *J. Am. Chem. Soc.*, **2008**, 130, 8414.
- [29] A. J. Banister, N. Bricklebank, I. Lavender, J. M. Rawson, C. I. Gregory, B. K. Tanner, W. Clegg, M. R. J. Elsegood, and F. Palacio, *Angew. Chem. Int. Ed. Engl.*, **1996**, 35, 2533.
- [30] H. Imai, T. Inabe, T. Otsuka, T. Okuno, and K. Awaga, *Phys. Rev. B*, **1996**, 54, 6838.
- [31] K. Awaga, T. Okuno, A. Yamaguchi, M. Hasegawa, T. Inabe, Y. Maruyama, and N. Wada, *Phys. Rev. B*, **1994**, 49, 3975.
- [32] K. Kanoda, and R. Kato, *Annu. Rev. Condens. Matter Phys.*, **2011**, 2, 167.
- [33] W. J. M. Naber, S. Faez, and W. G. van der Wiel, *J. Phys. D: Appl. Phys.*, **2007**, 40, R205.
- [34] T. Sugawara, and M. M. Matsushita, *J. Mater. Chem.*, **2009**, 19, 1738.
- [35] H. W. Kroto, J. R. Heath, S. C. O'Brien, R. F. Curl, and R. E. Smalley, *Nature*, **1985**, 318, 162.
- [36] W. Krätschmer, L. D. Lamb, K. Fostiropoulos, and D. R. Huffman, *Nature*, **1990**, 347, 354.
- [37] P.-M. Allemand, K. C. Khemani, A. Koch, F. Wudl, K. Holczer, S. Donovan, G. Grüner, and J. D. Thompson, *Science*, **1991**, 253, 301.
- [38] H. Yamaoka, T. Kambe, T. Sato, Y. Ishida, M. Matsunami, R. Eguchi, Y. Senba, and H. Ohashi, *Phys. Rev. B*, **2011**, 84, 161404(R).
- [39] Y. Iwasa, and T. Takenobu, *J. Phys.: Condens. Matter*, **2003**, 15, R495.
- [40] K. Tanigaki, T. W. Ebbesen, S. Saito, J. Mizuki, J. S. Tsai, Y. Kubo, and S. Kuroshima, *Nature*, **1991**, 352, 222.
- [41] T. Yildirim, L. Barbedette, J. E. Fischer, C. L. Lin, J. Robert, P. Petit, and T. T. M. Palstra, *Phys. Rev. Lett.*, **1996**, 77, 167.
- [42] O. Gunnarsson, *Rev. Mod. Phys.*, **1997**, 69, 575.
- [43] K. Prassides, *Curr. Opin. Solid State Mater. Sci.*, **1997**, 2, 433.
- [44] S. Kagoshima, T. Ishiguro, and H. Anzai, *J. Phys. Soc. Jpn.*, **1975**, 39, 1143.
- [45] F. Denoyer, F. Comès, A. F. Garito, and A. J. Heeger, *Phys. Rev. Lett.*, **1975**, 35, 445.
- [46] J. B. Goodenough, *Phys. Rev.*, **1955**, 100, 564.
- [47] J. B. Goodenough, *J. Phys. Chem. Solids*, **1958**, 6, 287.
- [48] J. Kanamori, *J. Phys. Chem. Solids*, **1959**, 10, 87.

- [49] K. E. Preuss, *Polyhedron*, **2014**, 79, 1.
- [50] J. Huang, S. Kingsbury, and M. Kertesz, *Phys. Chem. Chem. Phys.*, **2008**, 10, 2625.
- [51] M. Ishikawa, T. Asari, M. Matsuda, H. Tajima, N. Hanasaki, T. Naito, and T. Inabe, *J. Mater. Chem.*, **2010**, 20, 4432.
- [52] T. Asari, M. Ishikawa, T. Naito, M. Matsuda, H. Tajima, and T. Inabe, *Chem. Lett.*, **2005**, 34, 936.
- [53] H. M. Yamamoto, Y. Kosaka, R. Maeda, J. Yamaura, A. Nakao, T. Nakamura, and R. Kato, *ACS Nano*, **2008**, 2, 143.
- [54] H. M. Yamamoto, J. Yamaura, and R. Kato, *J. Am. Chem. Soc.*, **1998**, 120, 5905.
- [55] T. Imakubo, T. Maruyama, H. Sawa, and K. Kobayashi, *Chem. Commun.*, **1998**, 2021.
- [56] T. Imakubo, M. Kibune, H. Yoshino, T. Shirahata, and K. Yoza, *J. Mater. Chem.*, **2006**, 16, 4110.
- [57] T. Imakubo, and R. Murayama, *CrystEngComm*, **2013**, 15, 3072.
- [58] B. J. Powell, and R. H. McKenzie, *Rep. Prog. Phys.*, **2011**, 74, 056501.
- [59] R. Kato, and C. Hengbo, *Crystals*, **2012**, 2, 861.
- [60] R. Kato, *Bull. Chem. Soc. Jpn.*, **2014**, 87, 355374.
- [61] R. Kato, *Superstripes 2017*, edited by A. Bianconi (Superstripes Press, Rome, 2017), p. 173-174.
- [62] T. Isono, H. Kamo, A. Ueda, K. Takahashi, A. Nakao, R. Kumai, H. Nakao, K. Kobayashi, Y. Murakami, and H. Mori, *Nat. Commun.*, **2013**, 4, 1344.
- [63] T. Isono, H. Kamo, A. Ueda, K. Takahashi, M. Kimata, H. Tajima, S. Tsuchiya, T. Terashima, S. Uji, and H. Mori, *Phys. Rev. Lett.*, **2014**, 112, 177201.
- [64] A. Ueda, S. Yamada, T. Isono, H. Kamo, A. Nakao, R. Kumai, H. Nakao, Y. Murakami, K. Yamamoto, Y. Nishio, and H. Mori, *J. Am. Chem. Soc.*, **2014**, 136, 12184.
- [65] T. Sunada, *Not. Am. Math. Soc.*, **2008**, 55, 208.
- [66] T. Sunada, *Topological Crystallography With a View Towards Discrete Geometric Analysis Surveys and Tutorials in the Applied Mathematical Sciences*, edited by L. Sirovich, S. Antman, M. P. Brenner, P. Holmes, L. Mahadevan, A. Singer, K. R. Sreenivasan, and J. Victor (Springer, Tokyo, 2013), Vol. 6.
- [67] M. Itoh, M. Kotani, H. Naito, T. Sunada, Y. Kawazoe, and T. Adschiri, *Phys. Rev. Lett.*, **2009**, 102, 055703.
- [68] J. L. Mañes, *Phys. Rev. B*, **2012**, 85, 155118.
- [69] M. Tsuchiizu, *Phys. Rev. B*, **2016**, 94, 195426.
- [70] Y. Yao, J. S. Tse, J. Sun, D. D. Klug, R. Martoňák, and T. Iitaka, *Phys. Rev. Lett.*, **2009**, 102, 229601.
- [71] S. T. Hyde, M. O'Keeffe, and D. M. Proserpio, *Angew. Chem. Int. Ed.*, **2008**, 47, 7996.
- [72] A. H. Schoen, *Not. Am. Math. Soc.*, **2008**, 55, 663.
- [73] F. Laves, *Z. Kristallogr.*, **1932**, 82, 1.

- [74] H. Heesch, and F. Laves, *Z. Kristallogr.*, **1933**, 85, 443.
- [75] H. S. Coxeter, *Canad. J. Math.*, **1955**, 7, 18.
- [76] A. F. Wells, *Acta. Cryst.*, **1954**, 7, 535.
- [77] A. F. Wells, *Acta. Cryst.*, **1976**, B32, 2619.
- [78] K. Janzon, H. Schäfer, and A. Weiss, *Angew. Chem. Int. Ed.*, **1965**, 4, 245.
- [79] G. E. Pringle, *Acta. Cryst.*, **1972**, B28, 2326.
- [80] A. H. Schoen, *NASA Technical Note*, **1970**, TN D-5541.
- [81] C. T. Kresge, M. E. Leonowicz, W. J. Roth, J. C. Vartuli, and J. S. Beck, *Nature*, **1992**, 359, 710.
- [82] J. S. Beck, J. C. Vartuli, W. J. Roth, M. E. Leonowicz, C. T. Kresge, K. D. Schmitt, C. T. W. Chu, D. H. Olson, E. W. Sheppard, S. B. McCullen, J. B. Higgins, and J. L. Schlenker, *J. Am. Chem. Soc.*, **1992**, 114, 10834.
- [83] A. Monnier, F. Schüth, Q. Huo, D. Kumar, D. Margolese, R. S. Maxwell, G. D. Stucky, M. Krishnamurty, P. Petroff, A. Firouzi, M. Janicke, and B. F. Chmelka, *Science*, **1993**, 261, 1299.
- [84] V. Luzzati, and P. A. Spegt, *Nature*, **1967**, 215, 701.
- [85] D. A. Hajduk, P. E. Harper, S. M. Gruner, C. C. Honeker, G. Kim, E. L. Thomas, and L. J. Fetters, *Macromolecules*, **1994**, 27, 4063.
- [86] M. F. Schulz, F. S. Bates, K. Almdal, and K. Mortensen, *Phys. Rev. Lett.*, **1994**, 73, 86.
- [87] A. J. Meuler, M. A. Hillmyer, and F. S. Bates, *Macromolecules*, **2009**, 42, 7221.
- [88] M. D. Turner, M. Saba, Q. Zhang, B. P. Cumming, G. E. Schröger-Turk, and M. Gu, *Nat. Photonics*, **2013**, 7, 801.
- [89] C. Mille, E. C. Tyrode, and R. W. Corkery, *Chem. Commun.*, **2011**, 47, 9873.
- [90] Z. Qin, G. S. Jung, M. J. Kang, and M. J. Buehler, *Sci. Adv.*, **2017**, 3, e1601536.
- [91] M. I. Eremets, A. G. Gavriliuk, I. A. Trojan, D. A. Dzivenko, and R. Boehler, *Nat. Mater.*, **2004**, 3, 558.
- [92] S. Decurtins, H. W. Schmalle, P. Schneuwly, and H. R. Oswald, *Inorg. Chem.*, **1993**, 32, 1888.
- [93] Z. J. Chen, and D. B. Tian, *J. Appl. Phys.*, **2011**, 109, 033506.
- [94] M. Clemente-León, E. Coronado, C. J. Gómez-García, and A. Soriano-Portillo, *Inorg. Chem.*, **2006**, 45, 5653.
- [95] L. Balents, *Nature*, **2010**, 464, 199.
- [96] K. Momma, and F. Izumi, *J. Appl. Crystallogr.*, **2011**, 44, 1272.
- [97] P. W. Anderson, *Mater. Res. Bull.*, **1973**, 8, 153.
- [98] Z. Hiroi, H. Yoshida, Y. Okamoto, and M. Takigawa, *J. Phys. Conf. Ser.*, **2009**, 145, 012002.
- [99] Y. Shimizu, K. Miyagawa, K. Kanoda, M. Maesato, and G. Saito, *Phys. Rev. Lett.*, **2003**, 91, 107001.
- [100] Y. Okamoto, H. Yoshida, and Z. Hiroi, *J. Phys. Soc. Jpn.*, **2009**, 78, 033701.
- [101] Y. Okamoto, M. Nohara, H. Aruga-Katori, and H. Takagi, *Phys. Rev. Lett.*, **2007**, 99, 137207.

- [102] G. Chen, and L. Balents, *Phys. Rev. B*, **2008**, 78, 094403.
- [103] K. Ishida, M. Morishita, K. Yawata, and H. Fukuyama, *Phys. Rev. Lett.*, **1997**, 79, 3451.
- [104] E. Collin, S. Triqueneaux, R. Harakaly, M. Roger, C. Bäuerle, Yu. M. Bunkov, and H. Godfrin, *Phys. Rev. Lett.*, **2001**, 86, 2447.
- [105] R. Masutomi, Y. Karaki, and H. Ishimoto, *Phys. Rev. Lett.*, **2004**, 92, 025301.
- [106] S. Nakatsuji, Y. Nambu, H. Tonomura, O. Sakai, S. Jonas, C. Broholm, H. Tsunetsugu, Y. Qiu, and Y. Maeno, *Science*, **2005**, 309, 1697.
- [107] H. D. Zhou, E. S. Choi, G. Li, L. Balicas, C. R. Wiebe, Y. Qiu, J. R. D. Copley, and J. S. Gardner, *Phys. Rev. Lett.*, **2011**, 106, 147204.
- [108] J. G. Cheng, G. Li, L. Balicas, J. S. Zhou, J. B. Goodenough, C. Xu, and H. D. Zhou, *Phys. Rev. Lett.*, **2011**, 107, 197204.
- [109] Y. Li, B. Pan, S. Li, W. Tong, L. Ling, Z. Yang, J. Wang, Z. Chen, Z. Wu, and Q. Zhang, *New J. Phys.*, **2014**, 16, 093011.
- [110] T. Itou, A. Oyamada, S. Maegawa, M. Tamura, and R. Kato, *J. Phys. Condens. Matter*, **2007**, 19, 145247.
- [111] T. Itou, A. Oyamada, S. Maegawa, M. Tamura, and R. Kato, *Phys. Rev. B*, **2008**, 77, 104413.
- [112] T. Itou, A. Oyamada, S. Maegawa, and R. Kato, *Nat. Phys.*, **2010**, 6, 673.
- [113] H. Yamaguchi, M. Okada, Y. Kono, S. Kittaka, T. Sakakibara, T. Okabe, Y. Iwasaki, and Y. Hosokoshi, *Sci. Rep.*, **2017**, 7, 16144.
- [114] N. Wada, T. Kobayashi, H. Yano, T. Okuno, A. Yamaguchi, and K. Awaga, *J. Phys. Soc. Jpn.*, **1997**, 66, 961.
- [115] Y. Li, H. Liao, Z. Zhang, S. Li, F. Jin, L. Ling, L. Zhang, Y. Zou, L. Pi, Z. Yang, J. Wang, Z. Wu, and Q. Zhang, *Sci. Rep.*, **2015**, 5, 16419.
- [116] B. Koteswararao, R. Kumar, P. Khuntia, Sayantika Bhowal, S. K. Panda, M. R. Rahman, A. V. Mahajan, I. Dasgupta, M. Baenitz, Kee Hoon Kim, and F. C. Chou, *Phys. Rev. B*, **2014**, 90, 035141.
- [117] J. A. M. Paddison, H. Jacobsen, O. A. Petrenko, M. T. Fernández-Díaz, P. P. Deen, and A. L. Goodwin, *Science*, **2015**, 350, 179.
- [118] B. Zhang, P. J. Baker, Y. Zhang, D. Wang, Z. Wang, S. Su, D. Zhu, and F. L. Pratt, *J. Am. Chem. Soc.*, **2018**, 140, 122.
- [119] R. Coldea, D. A. Tennant, and Z. Tylczynski, *Phys. Rev. B*, **2003**, 68, 134424.
- [120] Y. Shirata, H. Tanaka, A. Matsuo, and K. Kindo, *Phys. Rev. Lett.*, **2012**, 108, 057205.
- [121] T. Hiramatsu, Y. Yoshida, G. Saito, A. Otsuka, H. Yamochi, M. Maesato, Y. Shimizu, H. Ito, and H. Kishida, *J. Mater. Chem. C*, **2015**, 3, 1378.
- [122] M. Yamashita, N. Nakata, Y. Senshu, M. Nagata, H. M. Yamamoto, R. Kato, T. Shibauchi, and Y. Matsuda, *Science*, **2010**, 328, 1246.

- [123] A. Zorko, S. Nellutla, J. van Tol, L. C. Brunel, F. Bert, F. Duc, J.-C. Trombe, M. A. de Vries, A. Harrison, and P. Mendels, *Phys. Rev. Lett.*, **2008**, 101, 026405.
- [124] E. Chappel, M. D. Núñez-Regueiro, G. Chouteau, O. Isnard, and C. Darie, *Eur. Phys. J. B*, **2000**, 17, 615.
- [125] Y. Zhou, K. Kanoda, and T.-K. Ng, *Rev. Mod. Phys.*, **2017**, 89, 025003.
- [126] S. V. Bhosale, C. H. Jani, and S. J. Langford, *Chem. Soc. Rev.*, **2008**, 37, 331.
- [127] M. A. Kobaisi, S. V. Bhosale, K. Latham, A. M. Raynor, and S. V. Bhosale, *Chem. Rev.*, **2016**, 116, 11685.
- [128] S.-L. Suraru, and F. Würthner, *Angew. Chem. Int. Ed. Engl.*, **2014**, 53, 7428.
- [129] N. Sakai, J. Mareda, E. Vauthey, and S. Matile, *Chem. Commun.*, **2010**, 46, 4225.
- [130] A. Diac, M. Matache, I. Grosu, and N. D. Hadade, *Adv. Synth. Catal.*, 10.1002/adsc.201701362.
- [131] J. Jazwinski, A. J. Blacker, J.-M. Lehn, M. Cesario, J. Guilhem, and C. Pascard, *Tetrahedron Lett.*, **1987**, 28, 6057.
- [132] G. D. Fallon, M. A.-P. Lee, S. J. Langford, and P. J. Nichols, *Org. Lett.*, **2004**, 6, 655.
- [133] M. E. Ozser, D. Uzun, I. Elci, H. Icil, and M. Demuth, *Photochem. Photobiol. Sci.*, **2003**, 2, 218.
- [134] S. Gabutti, M. Knutzen, M. Neuburger, G. Schull, R. Berndt, and M. Mayor, *Chem. Commun.*, **2008**, 2370.
- [135] S. P. Black, J. K. M. Sanders, and A. R. Stefankiewicz, *Chem. Soc. Rev.*, **2014**, 43, 1861.
- [136] N. Ponnuswamy, F. B. L. Cougnon, J. M. Clough, G. D. Pantoş, and J. K. M. Sanders, *Science*, **2012**, 338, 783.
- [137] J. Gawroński, M. Brzostowska, K. Gawrońska, J. Koput, U. Rychlewska, P. Skowronek, and B. Nordén, *Chem. Eur. J.*, **2002**, 8, 2484.
- [138] S. T. Schneebeli, M. Frasconi, Z. Liu, Y. Wu, D. M. Gardner, N. L. Strutt, C. Cheng, R. Carmieli, M. R. Wasielewski, and J. F. Stoddart, *Angew. Chem. Int. Ed.*, **2013**, 52, 13100.
- [139] Y. Wu, M. Frasconi, D. M. Gardner, P. R. McGonigal, S. T. Schneebeli, M. R. Wasielewski, and J. F. Stoddart, *Angew. Chem. Int. Ed.*, **2014**, 53, 9476.
- [140] Y. Wu, S. K. M. Nalluri, R. M. Young, M. D. Krzyaniak, E. A. Margulies, J. Fraser Stoddart, and M. R. Wasielewski, *Angew. Chem. Int. Ed.*, **2015**, 54, 1.
- [141] Z. Liu, G. Liu, Y. Wu, D. Cao, J. Sun, S. T. Schneebeli, M. S. Nassar, C. A. Mirkin, and J. F. Stoddart, *J. Am. Chem. Soc.*, **2014**, 136, 16651.
- [142] Z. Liu, J. Sun, Y. Zhou, Y. Zhang, Y. Wu, S. K. M. Nalluri, Y. Wang, A. Samanta, C. A. Mirkin, G. C. Schatz, and J. F. Stoddart, *J. Org. Chem.*, **2016**, 81, 2581.
- [143] Y. Wu, R. M. Young, M. Frasconi, S. T. Schneebeli, P. Spenst, D. M. Gardner, K. E. Brown, F. Würthner, J. F. Stoddart, and M. R. Wasielewski, *J. Am. Chem. Soc.*, **2015**, 137, 13236.
- [144] D. Chen, A.-J. Avestro, Z. Chen, J. Sun, S. Wang, M. Xiao, Z. Erno, M. M. Algaradah, M. S. Nassar, K. Amine, Y. Meng, and J. F. Stoddart, *Adv. Mater.*, **2015**, 27, 2907.

- [145] S. K. M. Nalluri, Z. Liu, Y. Wu, K. R. Hermann, A. Samanta, D. J. Kim, M. D. Krzyaniak, M. R. Wasielewski, and J. F. Stoddart, *J. Am. Chem. Soc.*, **2016**, 138, 5968.
- [146] D. J. Kim, K. R. Hermann, A. Prokofjevs, M. T. Otley, C. Pezzato, M. Owczarek, and J. F. Stoddart, *J. Am. Chem. Soc.*, **2017**, 139, 6635.
- [147] Y. Wu, M. D. Krzyaniak, J. F. Stoddart, and M. R. Wasielewski, *J. Am. Chem. Soc.*, **2017**, 139, 2948.
- [148] Z. Liu, S. K. M. Nalluri, and J. F. Stoddart, *Chem. Soc. Rev.*, **2017**, 46, 2459.
- [149] S. Kumar, M. R. Ajayakumar, G. Hundal, and P. Mukhopadhyay, *J. Am. Chem. Soc.*, **2014**, 136, 12004.
- [150] G. Bélanger-Chabot, A. Ali, and F. P. Gabbaï, *Angew. Chem. Int. Ed.*, **2017**, 56, 9958.
- [151] G. Heywang, L. Born, H.-G. Filzky, T. Hassel, J. Hocker, H.-K. Müller, B. Pittel, and S. Roth, *Angew. Chem. Int. Ed. Engl.*, **1989**, 28, 483.
- [152] F. Arias, Q. Xi, Y. Wu, Q. Lu, S. R. Wilson, and L. Echegoyen, *J. Am. Chem. Soc.*, **1994**, 116, 6388.
- [153] K. Yamamura, H. Miyake, S. Himeno, S. Inagaki, and K. Nakasuji, *Chem. Lett.*, **1988**, 17, 1819.
- [154] N. G. Connelly, and W. E. Geiger, *Chem. Rev.*, **1996**, 96, 877.
- [155] T. Fujikawa, Y. Segawa, and K. Itami, *J. Am. Chem. Soc.*, **2015**, 137, 7763.
- [156] T. Fujikawa, N. Mitoma, A. Wakamiya, A. Saeki, Y. Segawa, and K. Itami, *Org. Biomol. Chem.*, **2017**, 15, 4697.
- [157] A. L. Spek, *Acta Crystallogr., Sect. D*, **2009**, 65, 148.
- [158] M. Liu, L. Zhang, and T. Wang, *Chem. Rev.*, **2015**, 115, 7304.
- [159] S. Kitagawa, R. Kitaura, and S. Noro, *Angew. Chem., Int. Ed.*, **2004**, 43, 2334.
- [160] M. Kurmoo, *Chem. Soc. Rev.*, **2009**, 38, 1353.
- [161] X. Feng, X. Ding, and D. Jiang, *Chem. Soc. Rev.*, **2012**, 41, 6010.
- [162] S.-Y. Ding, and W. Wang, *Chem. Soc. Rev.*, **2013**, 42, 548.
- [163] J.-F. Penneau, B. J. Stallman, P. H. Kasai, and L. L. Miller, *Chem. Mater.*, **1991**, 3, 791.
- [164] M. R. Ajayakumar, P. Mukhopadhyay, S. Yadav, and S. Ghosh, *Org. Lett.*, **2010**, 12, 2646.
- [165] I. A. Shkrob, Y. Zhu, T. W. Marin, and D. J. Abraham, *Phys. Chem. C*, **2013**, 117, 19255.
- [166] Z. Wang, Y. Sun, X.-Q. Chen, C. Franchini, G. Xu, H. Weng, X. Dai, and Z. Fang, *Phys. Rev. B*, **2012**, 85, 195320.
- [167] Z. K. Liu, B. Zhou, Y. Zhang, Z. J. Wang, H. M. Weng, D. Prabhakaran, S.-K. Mo, Z. X. Shen, Z. Fang, X. Dai, Z. Hussain, and Y. L. Chen, *Science*, **2014**, 343, 864.
- [168] P. Bolduc, A. Jacques, and S. K. Collins, *J. Am. Chem. Soc.*, **2010**, 132, 12790.
- [169] *CrystalClear: Data Collection and Processing Software*, Rigaku Corporation, Tokyo, Japan, 2014.

- [170] G. M. Sheldrick, *Acta Crystallogr. Sect. A*, **2008**, 64, 112.
- [171] *CrystalStructure 4.1: Crystal Structure Analysis Package*, Rigaku Corporation, Tokyo, Japan, 2014.
- [172] M. J. Frisch, G. W. Trucks, H. B. Schlegel, G. E. Scuseria, M. A. Robb, J. R. Cheeseman, J. A. Montgomery, Jr. T. Vreven, K. N. Kudin, J. C. Burant, J. M. Millam, S. S. Iyengar, J. Tomasi, V. Barone, B. Mennucci, M. Cossi, G. Scalmani, N. Rega, G. A. Petersson, H. Nakatsuji, M. Hada, M. Ehara, K. Toyota, R. Fukuda, J. Hasegawa, M. Ishida, T. Nakajima, Y. Honda, O. Kitao, H. Nakai, M. Klene, X. Li, J. E. Knox, H. P. Hratchian, J. B. Cross, V. Bakken, C. Adamo, J. Jaramillo, R. Gomperts, R. E. Stratmann, O. Yazyev, A. J. Austin, R. Cammi, C. Pomelli, J. W. Ochterski, P. Y. Ayala, K. Morokuma, G. A. Voth, P. Salvador, J. J. Dannenberg, V. G. Zakrzewski, S. Dapprich, A. D. Daniels, M. C. Strain, O. Farkas, D. K. Malick, A. D. Rabuck, K. Raghavachari, J. B. Foresman, J. V. Ortiz, Q. Cui, A. G. Baboul, S. Clifford, J. Cioslowski, B. B. Stefanov, G. Liu, A. Liashenko, P. Piskorz, I. Komaromi, R. L. Martin, D. J. Fox, T. Keith, M. A. Al-Laham, C. Y. Peng, A. Nanayakkara, M. Challacombe, P. M. W. Gill, B. Johnson, W. Chen, M. W. Wong, C. Gonzalez, and J. A. Pople, *Gaussian 03, Revision D. 01*, Gaussian, Inc., Wallingford, CT, 2004.
- [173] A. C. Shockley, F. Bert, J-C. Orain, Y. Okamoto, and P. Mendels, *Phys. Rev. Lett.*, **2015**, 115, 047201.
- [174] P. Schiffer, A. P. Ramirez, D. A. Huse, P. L. Gammel, U. Yaron, D. J. Bishop, and A. J. Valentino, *Phys. Rev. Lett.*, **2015**, 74, 2379.
- [175] S. Guha, and S. Saha, *J. Am. Chem. Soc.*, **2010**, 132, 17674.
- [176] D. Gosztola, Mark P. Niemczyk, W. Svec, A. S. Lukas, and M. R. Wasielewski, *J. Phys. Chem. A*, **2000**, 104, 6545.
- [177] K. Nakamura, Y. Yoshimoto, T. Kosugi, R. Arita, and M. Imada, *J. Phys. Soc. Jpn.*, **2009**, 78, 083710.
- [178] K. Kanoda, *Hyperfine Interact.*, **1997**, 104, 235.
- [179] H. Taniguchi, T. Okuhata, T. Nagai, K. Satoh, N. Mōri, Y. Shimizu, M. Hedo, and Y. Uwatoko, *J. Phys. Soc. Jpn.*, **2007**, 76, 113709.
- [180] R. M. Vlasova, B. V. Petrov, and V. N. Semkin, *Phys. Solid State*, **2011**, 53, 1781.
- [181] H. Kino, and H. Fukuyama, *J. Phys. Soc. Jpn.*, **1995**, 64, 2726.
- [182] M. Sorai, S. Murakawa, T. Kotani, and H. Suga, *J. Phys. Chem. Solids*, **1983**, 44, 1133.
- [183] T. Senthil, M. Vojta, and S. Sachdev, *Phys. Rev. B*, **2004**, 69, 035111.
- [184] A. P. Ramirez, *Annu. Rev. Mater. Sci.*, **1994**, 24, 453.
- [185] S. Yamashita, Y. Nakazawa, M. Oguni, Y. Oshima, H. Nojiri, Y Shimizu, K. Miyagawa, and K. Kanoda, *Nat. Phys.*, **2008**, 4, 459.
- [186] A. P. Ramirez, *Nat. Phys.*, **2008**, 4, 442.

- [187] S. Yamashita, T. Yamamoto, Y. Nakazawa, M. Tamura, and R. Kato, *Nat. Commun.*, **2011**, 2, 275.
- [188] S. Yamashita, Y. Nakazawa, A. Ueda, and H. Mori, *Phys. Rev. B*, **2017**, 95, 184425.
- [189] Y. Shimizu, T. Hiramatsu, M. Maesato, A. Otsuka, H. Yamochi, A. Ono, M. Itoh, M. Yoshida, M. Takigawa, Y. Yoshida, and G. Saito, *Phys. Rev. Lett.*, **2016**, 117, 107203.
- [190] *RAPID-AUTO Ver. 2.40*, Rigaku Corporation, Tokyo, Japan, 2006.
- [191] *CrystalStructure 4.2.2: Crystal Structure Analysis Package*, Rigaku Corporation, Tokyo, Japan, 2016.
- [192] R. W. W. Hooft, L. H. Straver, and A. L. Spek, *J. Appl. Crst.*, **2008**, 41, 96.
- [193] Y. Karaki, K. Kuga, K. Kimura, S. Nakatsuji, K. Matsubayashi, and Y. Uwatoko, *J. Phys. Soc. Jpn.*, **2015**, 84, 084708.
- [194] J. C. Lashley, M. F. Hundley, A. Migliori, J. L. Sarrao, P. G. Pagliuso, T. W. Darling, M. Jaime, J. C. Cooley, W. L. Hults, L. Morales, D. J. Thoma, J. L. Smith, J. Boerio-Goates, B. F. Woodfield, G. R. Stewart, R. A. Fisher, and N. E. Phillips, *Cryogenics*, **2003**, 43, 369.
- [195] C. A. Kennedy, M. Stancescu, R. A. Marriott, and M. A. White, *Cryogenics*, **2007**, 47, 107.
- [196] S. W. V. Sciver, *Helium Cryogenics Second Edition, International Cryogenics Monograph Series*, edited by K. D. Timmerhaus, and C. Rizzuto (Springer, New York, 2012) p. 24.
- [197] T. Matsushita, N. Hori, S. Takata, N. Wada, N. Amaya, and Y. Hosokoshi, *Phys. Rev. B*, **2017**, 95, 020408.
- [198] M. J. Frisch, G. W. Trucks, H. B. Schlegel, G. E. Scuseria, M. A. Robb, J. R. Cheeseman, G. Scalmani, V. Barone, B. Mennucci, G. A. Petersson, H. Nakatsuji, M. Caricato, X. Li, H. P. Hratchian, A. F. Izmaylov, J. Bloino, G. Zheng, J. L. Sonnenberg, M. Hada, M. Ehara, K. Toyota, R. Fukuda, J. Hasegawa, M. Ishida, T. Nakajima, Y. Honda, O. Kitao, H. Nakai, T. Vreven, J. A. Montgomery, Jr., J. E. Peralta, F. Ogliaro, M. Bearpark, J. J. Heyd, E. Brothers, K. N. Kudin, V. N. Staroverov, R. Kobayashi, J. Normand, K. Raghavachari, A. Rendell, J. C. Burant, S. S. Iyengar, J. Tomasi, M. Cossi, N. Rega, J. M. Millam, M. Klene, J. E. Knox, J. B. Cross, V. Bakken, C. Adamo, J. Jaramillo, R. Gomperts, R. E. Stratmann, O. Yazyev, A. J. Austin, R. Cammi, C. Pomelli, J. W. Ochterski, R. L. Martin, K. Morokuma, V. G. Zakrzewski, G. A. Voth, P. Salvador, J. J. Dannenberg, S. Dapprich, A. D. Daniels, Ö. Farkas, J. B. Foresman, J. V. Ortiz, J. Cioslowski, and D. J. Fox, *Gaussian 09, Revision E.01*, Gaussian, Inc., Wallingford CT, 2009.
- [199] J. D. Watson, and F. H. C. Crick, *Nature*, **1953**, 171, 737.
- [200] L. Pauling, R. B. Corey, and H. R. Branson, *Proc. Natl. Acad. Sci. U. S. A.*, **1951**, 37, 205.
- [201] E. Yashima, and K. Maeda, *Macromolecules*, **2008**, 41, 3.
- [202] E. Yashima, K. Maeda, and Y. Furusho, *Acc. Chem. Res.*, **2008**, 41, 1166.
- [203] E. Yashima, K. Maeda, H. Iida, Y. Furusho, and K. Nagai, *Chem. Rev.*, **2009**, 109, 6102.
- [204] H. de Vries, *Acta Cryst.*, **1951**, 4, 219.

- [205] C. J. Pederson, *J. Am. Chem. Soc.*, **1967**, 89, 7017.
- [206] J. J. Christensen, D. J. Eatough, and R. M. Izatt, *Chem. Rev.*, **1974**, 74, 351.
- [207] G. Saito, H. Urayama, H. Yamochi, and K. Oshima, *Synth. Met.*, **1988**, 27, A331.
- [208] B. Zheng, F. Wang, S. Dong, and F. Huang, *Chem. Soc. Rev.*, **2012**, 41, 1621.
- [209] H.-J. Buschmann, *Polyhedron*, **1988**, 7, 721.
- [210] D. Ph. Zollinger, E. Bulten, A. Christenhusz, M. Bos, and W. E. van der Linden, *Anal. Chim. Acta*, **1987**, 198, 207.
- [211] H.-J. Buschmann, *J. Incl. Phenom. Mol. Recognit. Chem.*, **1989**, 7, 581.
- [212] R. D. Boss, and A. I. Popov, *Inorg. Chem.*, **1986**, 25, 1747.
- [213] R. T. Streeper, and S. Khazaeli, *Polyhedron*, **1991**, 10, 221.
- [214] E. Mei, A. I. Popov, and J. L. Dye, *J. Phys. Chem.*, **1977**, 81, 1677.
- [215] M. A. Ramos, C Talón, R. J. Jiménez-Riobóo, and S. Vieira, *J. Phys.: Condens. Matter*, **2003**, 15, S1007.
- [216] *CrystalStructure 4.2.5: Crystal Structure Analysis Package*, Rigaku Corporation, Tokyo, Japan, 2017.
- [217] T. C. Umland, S. Allie, T. Kuhlmann, and P. Coppens, *J. Phys. Chem.*, **1988**, 92, 6456.
- [218] S. Akoudad, P. Frère, N. Mercier, and J. Roncali, *J. Org. Chem.*, **1999**, 64, 4267.
- [219] E. S. Pysh, and N. C. Yan, *J. Am. Chem. Soc.*, **1963**, 85, 2124.
- [220] J. B. Torrance, *Mol. Cryst. Liq. Cryst.*, **1985**, 126, 55.
- [221] *CrystalClear: Data Collection and Processing Software*, Rigaku Corporation, Tokyo, Japan, 2015.
- [222] A. Altomare, G. Cascarano, C. Giacovazzo, and A. Guagliardi, *J. Appl. Cryst.*, **1993**, 26, 343.
- [223] G. M. Sheldrick, *Acta Cryst. A*, **2014**, 70, C1437.

## List of Publications

### Supplemental Publications

[1] “Discovery of the  $K_4$  Structure Formed by a Triangular  $\pi$  Radical Anion”

A. Mizuno, Y. Shuku, R. Suizu, M. M. Matsushita, M. Tsuchiizu, D. Reta Mañeru, F. Illas, V. Robert, and K. Awaga,  
*J. Am. Chem. Soc.*, **2015**, 137, 7612-7615.

[2] “3D Spin-Liquid State in an Organic Hyperkagome Lattice of Mott dimers”

A. Mizuno, Y. Shuku, M. M. Matsushita, M. Tsuchiizu, Y. Hara, N. Wada, Y. Shimizu, and K. Awaga,  
*Phys. Rev. Lett.*, **2017**, 119, 057201 (6 pages).

### Publications not related to this thesis

[1] “The key role of vibrational entropy in the phase transitions of dithiazolyl-based bistable magnetic materials”

S. Vela, F. Mota, M. Deumal, R. Suizu, Y. Shuku, A. Mizuno, K. Awaga, M. Shiga, J. J Novoa, and J. Ribas-Arino,  
*Nature Commun.*, **2014**, 5, 4411 (9 pages).